

Copyright Warning & Restrictions

The copyright law of the United States (Title 17, United States Code) governs the making of photocopies or other reproductions of copyrighted material.

Under certain conditions specified in the law, libraries and archives are authorized to furnish a photocopy or other reproduction. One of these specified conditions is that the photocopy or reproduction is not to be “used for any purpose other than private study, scholarship, or research.” If a user makes a request for, or later uses, a photocopy or reproduction for purposes in excess of “fair use” that user may be liable for copyright infringement,

This institution reserves the right to refuse to accept a copying order if, in its judgment, fulfillment of the order would involve violation of copyright law.

Please Note: The author retains the copyright while the New Jersey Institute of Technology reserves the right to distribute this thesis or dissertation

Printing note: If you do not wish to print this page, then select “Pages from: first page # to: last page #” on the print dialog screen

The Van Houten library has removed some of the personal information and all signatures from the approval page and biographical sketches of theses and dissertations in order to protect the identity of NJIT graduates and faculty.

ABSTRACT

CLOSED-LOOP CONTROL OF VORTEX SHEDDING BY MEANS OF LORENTZ FORCE

**by
Xiaoyun Sun**

When an incompressible fluid flows past a circular cylinder, vortex shedding occurs as soon as the Reynolds number exceeds about 40. Vortex shedding is usually undesirable, as it generates a significant increase in drag, as well an oscillating lift force on the cylinder leading to cross-stream structural vibrations. Flow control to either delay the appearance of vortex shedding or fully suppress it has attracted much attention during the last decade. The focus of this dissertation is to control vortex shedding from a circular cylinder by applying an external electromagnetic field. As in previous works, the latter is generated by electrodes and magnets alternatively arranged on the cylinder surface. In a weakly conducting fluid such as seawater, this has the effect of creating a Lorentz force tangential to the surface of the cylinder and oriented in the flow direction. A novel analytical expression of the Lorentz force is derived by integrating the Maxwell equations and using series expansions. This expression is then used for the control of vortex shedding in numerical simulations. Specifically, a closed-loop control algorithm is derived utilizing a single point sensor on the cylinder surface and the bilinear searching method in order to determine the appropriate magnitude of the Lorentz force at every time. Numerical simulations based on a two-dimensional Navier-Stokes solver show that vortex shedding is indeed suppressed at the Reynolds number values $Re = 100$ and 200 .

**CLOSED-LOOP CONTROL OF VORTEX SHEDDING
BY MEANS OF LORENTZ FORCE**

by
Xiaoyun Sun

**A Dissertation
Submitted to the Faculty of
New Jersey Institute of Technology
in Partial Fulfillment of the Requirements for the Degree of
Doctor of Philosophy in Mathematical Sciences**

Department of Mathematical Sciences

January 2003

Copyright © 2003 by Xiaoyun Sun

ALL RIGHTS RESERVED

APPROVAL PAGE

**CLOSED-LOOP CONTROL OF VORTEX SHEDDING
BY MEANS OF LORENTZ FORCE**

Xiaoyun Sun

Dr. Nadine Aubry, Dissertation Advisor
Distinguished Professor, Department of Mechanical Engineering and
Department of Mathematical Sciences, NJIT Date

Dr. Denis Blackmore, Committee Member
Professor, Department of Mathematical Sciences, NJIT Date

Dr. Demetrius Papageorgiou, Committee Member
Professor, Department of Mathematical Sciences, NJIT Date

Dr. Pushendra Singh, Committee Member
Associate Professor, Department of Mechanical Engineering, NJIT Date

Dr. Lou Kondic, Committee Member
Associate Professor, Department of Mathematical Sciences, NJIT Date

BIOGRAPHICAL SKETCH

Author: Xiaoyun Sun
Degree: Doctor of Philosophy
Date: January 2003

Undergraduate and Graduate Education:

- Doctor of Philosophy in Mathematical Sciences, New Jersey Institute of Technology, Newark, NJ, 2003
- Master of Applied Mathematics, New Jersey Institute of technology, Newark, NJ, 2000
- Master of Engineering Thermophysics, Chinese Academy of Sciences, Beijing, China, 1986
- Bachelor of Thermophysics Engineering, Zhejiang University, Hangzhou, Zhejiang, China, 1983

Major: Mathematical Sciences

Presentations and Publications Related to Dissertation:

Sun, X. Y. and Aubry, N. "Closed-loop control of vortex shedding from a cylinder by a single sensor", 55th Conference of Division of Fluid Dynamics, American Physical Society, EG.002, Dallas, Texas, November 23-26, 2002.

Sun, X. Y. and Aubry, N., "Control of Vortex Shedding by Electro-Magnetic Field" (keynote), ASME- European Fluids Engineering Division Conference, FEDSM2002-31277, Montreal, Canada, July 14-18, 2002.

Sun, X. Y. and Aubry, N., "Control of Vortex Shedding from Cylinder by Electromagnetic Field", 14th U. S. National Congress on Theoretical and Applied Mechanics, Blacksburg, Virginia, June 23-28, 2002.

Sun, X. Y. and Aubry, N., "Electro-Magnetic Control of Vortex Shedding", 54th Conference of Division of Fluid Dynamics, American Physical Society, FN 6, San Diego, California, November 18-20, 2001.

Sun, X. Y. and Aubry, N., "Optimal Feedback Control of Cylinder Vortex Shedding with Lorentz Force", 53rd Conference of Division of Fluid Dynamics, American Physical Society, DH.004, Washington D.C., November 19-21, 2000.

To my beloved family

ACKNOWLEDGEMENT

I would like to express my deepest gratitude to my advisor, Dr. Nadine Aubry, without whom the completion of this dissertation would have been impossible, and for her continuous encouragement, support during the past several years. Her generous advice and constant faith have made my time with her a very rewarding experience.

Special thanks are given to Dr. Denis Blackmore, Dr. Demetrius Papageorgiou, Dr. Pushpedra Singh, and Dr. Lou Kondic for actively serving on my dissertation committee.

Thanks to Ms. Sharyn Serifin who gave me the assistance I needed in my research work in the Computational Fluid Dynamics Lab and routine operations of the research group.

Thanks also to all my colleagues, in the Computational Fluid Dynamics Laboratory, for many useful discussions and continued help, allowing me work in a friendly environment.

I am very indebted to my wife, Yunyu Joyce Zhao, and my daughter, Tian Sun, for giving me great support that helped me concentrate on my research.

TABLE OF CONTENTS

Chapter	Page
1 INTRODUCTION	1
1.1 Background.....	1
1.2 Flow Control with Electromagnetic Fields.....	5
1.3 Research Objectives.....	7
2 GOVERNING EQUATIONS AND MATHEMATICAL MANIPULATIONS....	8
2.1 Governing Equations	8
2.2 Pressure Coefficient.....	10
2.3 Force Coefficients.....	13
2.4 Discrete Form of the Equations and Numerical Algorithm	15
2.5 Initial and Boundary Conditions.....	20
2.6 Numerical Treatment of Vorticity on the Wall.....	24
3 DISCUSSION OF LORENTZ FORCE IN PLATE CASE.....	26
3.1 Background.....	26
3.2 Governing Equations	29
3.3 Analysis of Lorentz Force Applied in an Infinite Plate.....	30
3.4 Comparison of Numerical and Analytical Expression of Lorentz Force in Plate Case.....	37
4 ANALYSIS OF LORENTZ FORCE APPLIED IN THE CASE OF AN INFINITE CIRCULAR CYLINDER	42
4.1 Introduction.....	42
4.2 Numerical Method	45
4.3 Analytical Investigation.....	47
4.4 Approximate Solution.....	52

TABLE OF CONTENTS
(Continued)

Chapter	Page
4.5 Simplified Approximate Solution.....	56
5 CONTROL OF VORTEX SHEDDING FROM CYLINDER BY ELECTROMAGNETIC FIELDS.....	65
5.1 Introduction.....	65
5.2 Open Control.....	67
5.3 Closed-loop Control.....	72
5.4 Closed-loop Control with a Single Sensor.....	84
6 CONCLUSIONS.....	99
APPENDIX A SOLUTION OF TWO DIMENSIONAL LAPLACE EQUATION WITH DIRICHLET BOUNDARY CONDITION ON A CIRCLE.....	101
APPENDIX B SIMPLIFICATION OF INTEGRAL EXPRESSION IN THE ANALYTICAL EXPRESSION OF THE ELECTRIC POTENTIAL.....	106
APPENDIX C GENERATION OF A VORTEX FLOW BY MEANS OF AN ELECTROMAGNETIC CYLINDER.....	110
REFERENCES.....	115

LIST OF TABLES

Table		Page
2.1	Nondimensionalized Parameters.....	9
3.1	Numerical results for the average of the Lorentz force at the wall for different values $\frac{h}{2a}$ of mesh element sizes	38
4.1	Values of the coefficient functions $c_{00}(z)$ and $c_{01}(z)$ at various z values.....	57
5.1	Summary of the effect of the single sensor closed-loop control algorithm on the flow at the Reynolds number $Re = 100$, for various actuation areas.	97
5.2	Summary of the effect of the single sensor closed-loop control algorithm on the flow at the Reynolds number $Re = 200$, for various actuation areas.	97

LIST OF FIGURES

Figure	Page
1.1 Flow past a circular cylinder at Reynolds number $Re=1.54$	2
1.2 Flow past a circular cylinder at Reynolds number $Re=9.6$	2
1.3 Flow past a circular cylinder at Reynolds number $Re=13.1$	3
1.4 Flow past a circular cylinder at Reynolds number $Re=26$	3
2.1 Computational domain for the simulation of the flow past a circular cylinder. ...	17
3.1 Scheme for the alternating arrangement of electromagnetic fields.	28
3.2 Computational domain for the electric field and magnetic fields.....	31
3.3 Distribution of the Lorentz force in plate case with various terms in the summation.....	35
3.4 Distribution of the Lorentz force in plane case with various terms in the summation (Continued).	36
3.5 Numerical result for the electric and magnetic potential distributions and the corresponding Lorentz force.	40
3.6 Comparison of the average Lorentz force in the case of a flat plate showing good agreement between the analytical and numerical results derived in this dissertation.	41
4.1 Arrangement of the electrodes and magnets generating a Lorentz force in the flow past a cylinder.	44
4.2 Comparison of the Lorentz force computed from the DM model, the MIX model and the numerical simulations for the aspect ratio $a/b = 0.1$	60
4.3 Comparison of the Lorentz force computed from the DM model, the MIX model and the numerical simulations for the aspect ratio $a/b = 0.2$	61
4.4 Comparison of the Lorentz force computed from the DM model, the MIX model and the numerical simulations for the aspect ratio $a/b = 0.3$	62
4.5 Comparison of the Lorentz force computed from the DM model, the MIX model and the numerical simulations for the aspect ratio $a/b = 0.4$	63

LIST OF FIGURES
(Continued)

Figure	Page
4.6 Comparison of the Lorentz force computed from the DM model, the MIX model and the numerical simulations for the aspect ratio $a/b = 0.5$	64
5.1 Schematics of open loop control.....	67
5.2 Visualization of the flow by vorticity contours for the flow without control at the Reynolds number $Re = 100$, showing vortex shedding.	68
5.3 Visualization of the flow by streamlines for the flow without control at the Reynolds number $Re = 100$, showing vortex shedding	69
5.4 Visualization of the flow by vorticity contours for the flow after open loop control at the Reynolds number $Re = 100$. The interaction parameter value is $N = 2$. This clearly shows vortex shedding is fully suppressed by the control....	70
5.5 Visualization of the flow by streamlines for the flow with open loop control at the Reynolds number $Re = 100$. The interaction parameter is $N = 2$. The control scheme suppresses vortex shedding, the streamline originating at the rear stagnation point becoming eventually straight and horizontal	71
5.6 Schematics of closed-loop control.	73
5.7 Schematics of actuation and sensing arrangement on the cylindrical surface	74
5.8 Visualization of the flow by vorticity contours after closed loop control (using the algorithm given by Equation (5.8) in the text) at the Reynolds number $Re = 100$. This clearly shows that vortex shedding is fully suppressed by closed loop control.	77
5.9 Time history of the drag coefficient for the closed-loop controlled flow of Figure 5.8.....	78
5.10 Time history of the lift coefficient for the closed-loop controlled flow of Figure 5.8.	78
5.11 Time history of the interaction parameter N for the closed-loop control flow of Figure 5.8.....	79
5.12 Time history of the vorticity at the rear stagnation point for the closed loop controlled flow of Figure 5.8.	79

LIST OF FIGURES
(Continued)

Figure	Page
5.13 Visualization of the flow by vorticity contours after closed loop control (using the algorithm given by Equation (5.8) in the text) at the Reynolds number $Re = 200$. This clearly shows that vortex shedding is fully suppressed by closed loop control	81
5.14 Time history of the drag coefficient for the closed-loop controlled flow of Figure 5.13.....	82
5.15 Time history of the lift coefficient for the closed-loop controlled flow of Figure 5.13.	82
5.16 Time history of the interaction parameter for the closed-loop controlled flow of Figure 5.13.....	83
5.17 Time history of the vorticity at rear stagnation point for the closed-loop controlled flow of Figure 5.13.	83
5.18 Detecting position of the single sensor closed-loop control algorithm.....	84
5.19 Drag and lift coefficients C_d and C_L for the closed-loop controlled flow with a single sensor at the Reynolds number $Re = 100$, in Case I described in the text.....	86
5.20 Interaction parameter N and vorticity ω_{rear} at the rear stagnation point for the closed-loop controlled flow with a single sensor at the Reynolds number $Re = 100$, in Case I described in the text.....	86
5.21 Drag and lift coefficients C_d and C_L for the closed-loop controlled flow with a single sensor at the Reynolds number $Re = 100$, in Case II described in the text.....	87
5.22 Interaction parameter N and vorticity ω_{rear} at the rear stagnation point for the closed-loop controlled flow with a single sensor at the Reynolds number $Re = 100$, in Case II described in the text.	87
5.23 Drag and lift coefficients C_d and C_L for the closed-loop controlled flow with a single sensor at the Reynolds number $Re = 100$, in Case III described in the text.....	88
5.24 Interaction parameter N and vorticity ω_{rear} at the rear stagnation point for the closed-loop controlled flow with a single sensor at the Reynolds number $Re = 100$, in Case III described in the text.	88

**LIST OF FIGURES
(Continued)**

Figure	Page
5.25 Drag and lift coefficients C_d and C_L for the closed-loop controlled flow with a single sensor at the Reynolds number $Re = 100$, in Case IV described in the text.....	89
5.26 Interaction parameter N and vorticity ω_{rear} at the rear stagnation point for the closed-loop controlled flow with a single sensor at the Reynolds number $Re = 100$, in Case IV described in the text.....	89
5.27 Drag and lift coefficients C_d and C_L for the closed-loop controlled flow with a single sensor at the Reynolds number $Re = 100$, in Case V described in the text.....	90
5.28 Interaction parameter N and vorticity ω_{rear} at the rear stagnation point for the closed-loop controlled flow with a single sensor at the Reynolds number $Re = 100$, in Case V described in the text.	90
5.29 Drag and lift coefficients C_d and C_L for the closed-loop controlled flow with a single sensor at the Reynolds number $Re = 200$, in Case I described in the text.....	91
5.30 Interaction parameter N and vorticity ω_{rear} at the rear stagnation point for the closed-loop controlled flow with a single sensor at the Reynolds number $Re = 200$, in Case I described in the text.....	91
5.31 Drag and lift coefficients C_d and C_L for the closed-loop controlled flow with a single sensor at the Reynolds number $Re = 200$, in Case II described in the text.....	92
5.32 Interaction parameter N and vorticity ω_{rear} at the rear stagnation point for the closed-loop controlled flow with a single sensor at the Reynolds number $Re = 200$, in Case II described in the text.	92
5.33 Drag and lift coefficients C_d and C_L for the closed-loop controlled flow with a single sensor at the Reynolds number $Re = 200$, in Case III described in the text.....	93
5.34 Interaction parameter N and vorticity ω_{rear} at the rear stagnation point for the closed-loop controlled flow with a single sensor at the Reynolds number $Re = 200$, in Case III described in the text.	93

LIST OF FIGURES
(Continued)

Figure	Page
5.35 Drag and lift coefficients C_d and C_L for the closed-loop controlled flow with a single sensor at the Reynolds number $Re = 200$, in Case IV described in the text.....	94
5.36 Interaction parameter N and vorticity ω_{rear} at the rear stagnation point for the closed-loop controlled flow with a single sensor at the Reynolds number $Re = 200$, in Case IV described in the text.....	94
5.37 Drag and lift coefficients C_d and C_L for the closed-loop controlled flow with a single sensor at the Reynolds number $Re = 200$, in Case V described in the text.....	95
5.38 Interaction parameter N and vorticity ω_{rear} at the rear stagnation point for the closed-loop controlled flow with a single sensor at the Reynolds number $Re = 200$, in Case V described in the text.....	95
A.1 Conformal mapping the computational domain outside cylinder to a circle.....	101
C.1 Scheme of the generation of a vortex by the displayed alternating arrangement of electrodes and	110

CHAPTER 1

INTRODUCTION

1.1 Background

A viscous fluid flowing around a circular cylinder has attracted much attention in the scientific community over the years. More recently, the focus has been on controlling the flow as Reynolds number increases. Here, the Reynolds number is defined as $Re_d = u_\infty d / \nu$, d being the diameter of the cylinder, ν the kinematics viscosity of the fluid and u_∞ the incoming flow velocity. At small values of the Reynolds number ($Re = 1 \sim 6$), the flow remains attached to the solid body and its streamlines are symmetric with respect to the centerline. When the Reynolds number reaches $Re \sim 10$, the flow detaches itself from the body at a separation point located near the rear stagnation point and a small bubble of two counter-rotating, symmetric vortices appears in the rear part of the cylinder (Figures 1.1 and 1.2). As the Reynolds number increases further, the separation point on the cylinder surface moves toward the front stagnation point gradually, making the bubble become larger and larger (Figure 1.3 and 1.4, Van Dyke, M., 1982). When the Reynolds number reaches about $Re = 48$, the bubble sheds its vortices away from the cylinder surface in an alternative and periodic fashion. At higher Reynolds number values, the flow remains organized in a structured pattern, or Von Karman vortex street, in which upper and lower vortices shed alternatively. As the Reynolds becomes larger, the vortices grow in size and are further away from one another. At the Reynolds number $Re \sim 160$, a three dimensional instability develops, as a step toward the route to turbulence. This dissertation focuses on the control of vortex shedding before the three-dimensionality sets in.

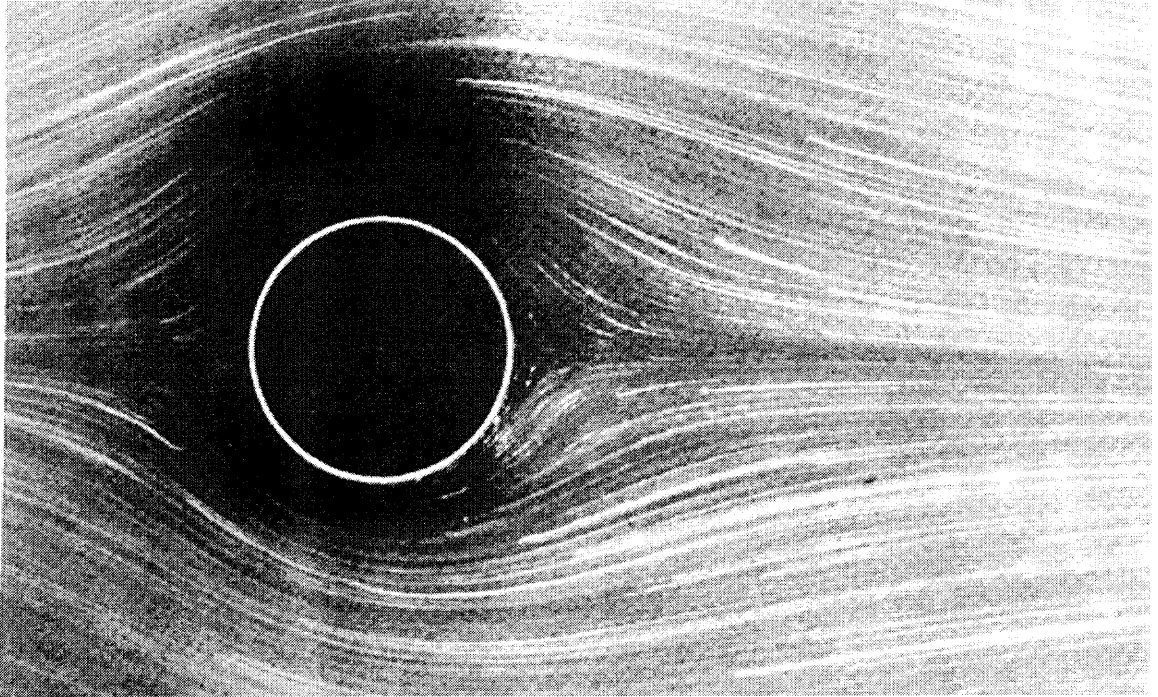


Figure 1.1 Flow past a circular cylinder at Reynolds number $Re = 1.54$ (from Van Dyke, 1982).

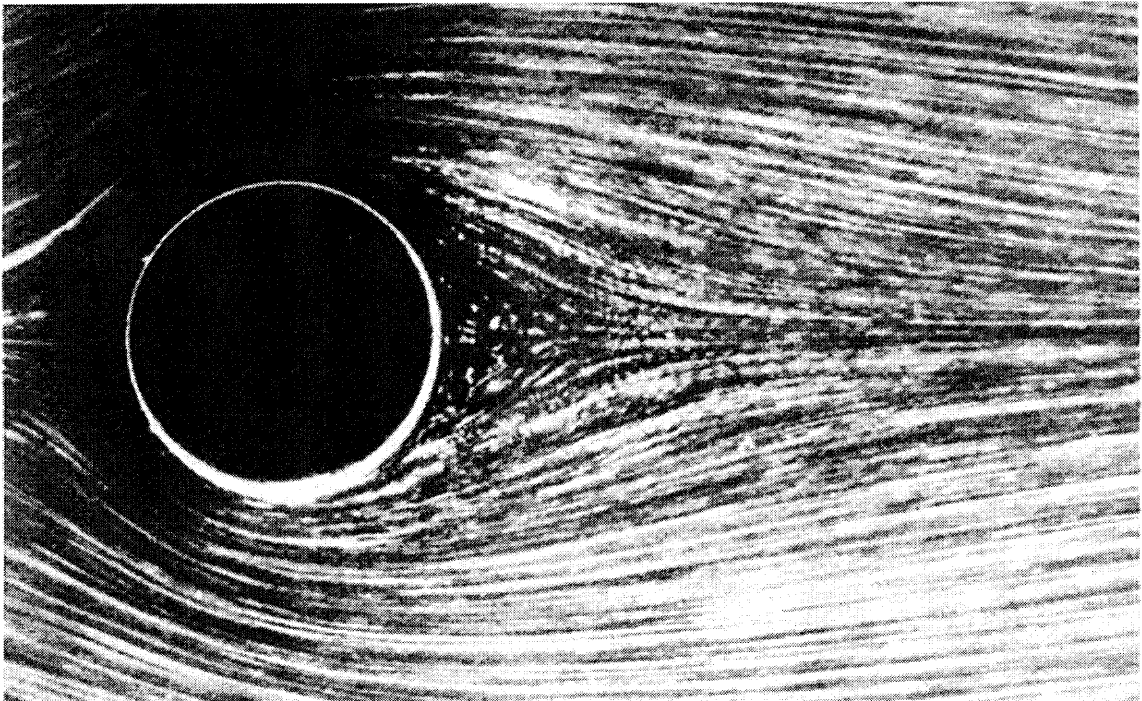


Figure 1.2 Flow passing a circular cylinder at the Reynolds number $Re = 9.6$ (from Van Dyke, 1982).

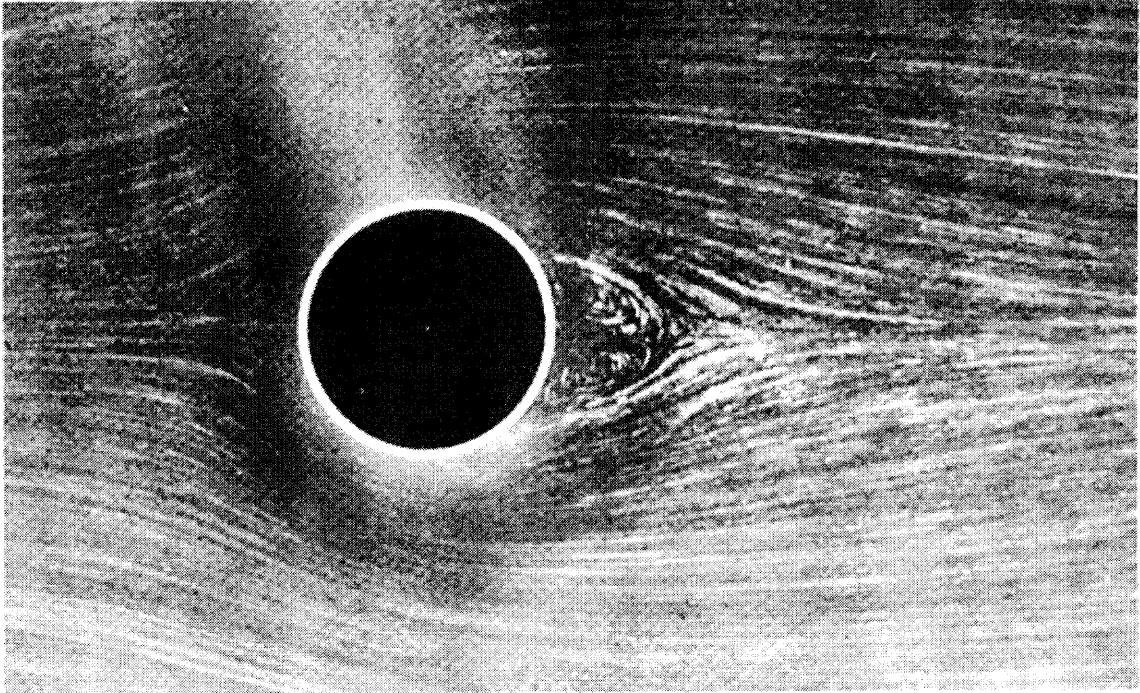


Figure 1.3 Flow passing a circular cylinder at the Reynolds number $Re = 13.1$ (from Van Dyke, 1982).

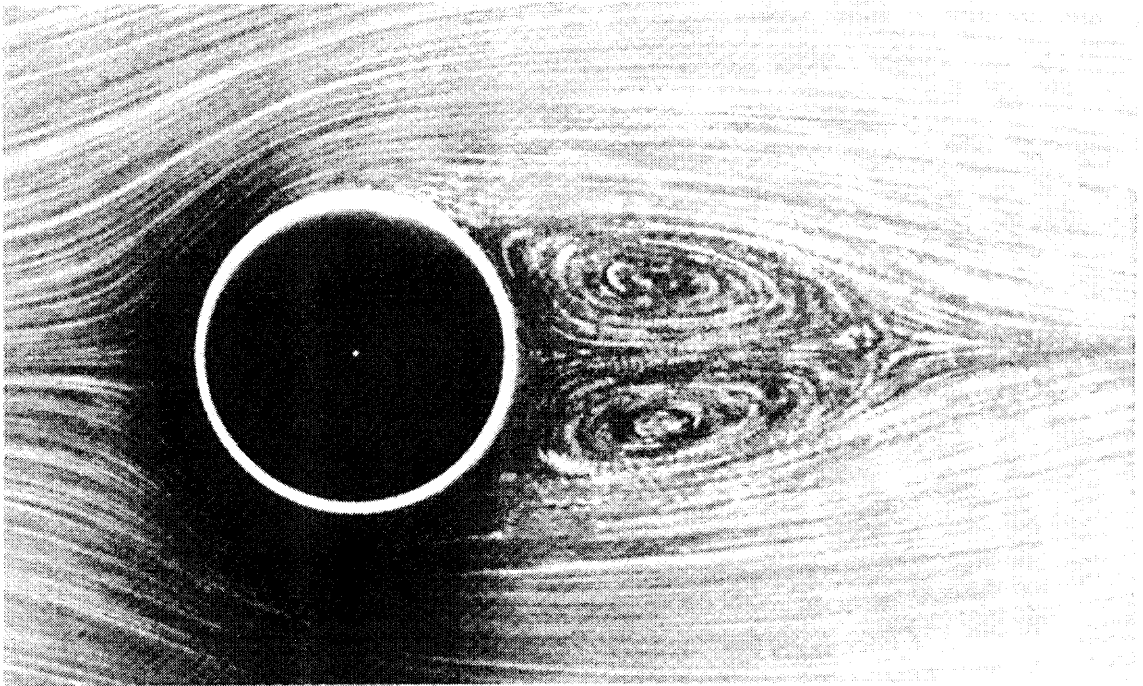


Figure 1.4 Flow passing a circular cylinder at the Reynolds number $Re = 26$ (from Van Dyke, 1982).

Flow control can be divided in two categories, passive and active control. Passive control uses a mere, advantageous alteration of the boundary conditions, while active control requires the input of a force and/or energy into the flow. Active control can be further subdivided into two categories, open or closed-loop control. Open loop control requires one or more actuators, but no information on the flow (Gad-el-Hak, M., 1996), while closed-loop feedback control requires both actuators and sensors. Examples of passive control of vortex shedding consist of the insertion of end plates (Stansby, P., 1974) or splitter plates (Apelt and West, 1975), and the placing of a small secondary cylinder in the flow (Strykowski and Hannemann, 1991). Examples of active control for vortex shedding can be found in the literature only more recently. For instance, Roussopoulos (1993) conducted feedback control using a speaker based on the velocity phase information measured at a point in the wake. Park *et al.* (1994) used a pair of blowing/suction slots on the cylinder and a single feedback sensor located in the wake. They showed a complete suppression of vortex shedding at the Reynolds number $Re = 60$.

It is well known that the drag on the cylinder has two terms, one due to friction and the other one originating in the net force due to pressure. In many studies of flow control at low Reynolds numbers, control algorithms seek the decrease of pressure drag by suppressing vortex shedding from the cylinder. For example, Monkewitz *et al.* (1989) studied the possibility of feedback control by means of global oscillations. In another study, Park *et al.* (1993) used a single sensor and a pair of blowing/suction actuators. Finally, Min and Choi (1998) derived a sub-optimal feedback control procedure and investigated the performance of three generated cost functions, all related one way or the other to the pressure distribution on the cylinder surface.

1.2 Flow Control with Electromagnetic Fields

It is well-known that a body force, or Lorentz force, is generated in a conducting fluid subjected to an electric field and a magnetic field non-parallel to one another. Several decades ago, much attention was given to the generation of electric current, and thus electric power, by the motion of a fluid conductor in the presence of magnetic and electric fields. This idea is now being explored in the context of flow control. One advantage over other control methods is the absence of moving parts and therefore the potential of miniaturization.

Gailitis and Leilausis (1961) first proposed to use an alternating arrangement of electrodes and magnets on a plate to generate a Lorentz force that is parallel to the plate. Depending on the flow direction, the Lorentz force can be either parallel or perpendicular to the flow direction. Henoah and Stace (1995) conducted an experimental investigation of a turbulent boundary layer flow subjected to a magnetohydrodynamic (MHD) body force in the streamwise direction. The MHD force was found to decrease the turbulence intensity up to 30%. In a parallel study, Crawford and Karniadakis (1997) studied the effect of an electromagnetic force on a flow past a flat plate via direct numerical simulations. Their results show that the Lorentz force generated from an alternating arrangement of electromagnetic field is quasi-periodic in the spanwise direction and decay exponentially fast in the normal direction. Berger *et al.* (2000) also found an exponentially decaying function for the Lorentz force in the direction normal to the plate, assuming that the electromagnetic field on the solid wall boundary follows a cosine distribution.

The control of vortex shedding from a cylinder in a conducting fluid by means of electromagnetic fields is an interesting research topic with potentially promising applications for future designs of ships and sea vessels, or for bio-technological applications. It is thus common to consider seawater as the fluid. Due to the low conductivity of saltwater, the Lorentz force exists only in the vicinity of the electrodes and magnets and its magnitude decreases dramatically with the distance from the wall.

While Mutschke *et al.* (1997, 1998) conducted cylinder wake control by means of a uniform magnetic field in liquid metal flows, Weier *et al.* (1998) first proposed the possibility of controlling vortex shedding with the alternating arrangement of electrodes and magnets studied in this dissertation and demonstrated the suppression of vortex shedding experimentally by means of open control. Aubry *et al.* (2000) explored the possibility of closed-loop control by means of the same Lorentz force.

It is interesting to recall that Posdziech and Grundmann (2001) pointed out that in studying the control of vortex shedding by alternating electrodes and magnets, the magnitude of the Lorentz force was not the only parameter of importance. The relative width of electrodes and magnets compared with the cylinder radius played a crucial role as well. Their numerical simulations showed that the magnitude of the Lorentz force needed to control the flow varied dramatically for different ratios.

Kim and Lee's (2000, 2001) experiments demonstrated that the Lorentz force was also capable of suppressing vortex shedding at high Reynolds number values such as $Re = 2500$ and 5000 .

1.3 Research Objectives

The research objective of this dissertation is to develop a realistic closed-loop control algorithm to suppress vortex shedding from a circular cylinder by means of a Lorentz force. In order to address this problem, the electro-magnetism problem is first studied in detail. Then, the fluid mechanics equations are solved numerically first in an open control manner, and second with the aid of two closed-loop control algorithms. While all techniques are successful at controlling the flow, they are not equivalent for practical purposes. One technique uses many sensors on the cylinder surface, while the other one requires the use of one sensor only. Finally, the results are analyzed from a power consumption viewpoint.

CHAPTER 2

GOVERNING EQUATIONS AND MATHEMATICAL MANIPULATIONS

2.1 Governing Equations

The continuity and momentum equations for a two-dimensional incompressible viscous flow are

$$\nabla \cdot \vec{u} = 0 \quad (2.1)$$

$$\frac{\partial \vec{u}}{\partial t} + (\vec{u} \cdot \nabla) \vec{u} = \frac{1}{\rho} \nabla p + \nu \nabla^2 \vec{u} + \frac{\vec{f}}{\rho} \quad (2.2)$$

where \vec{u} is the fluid velocity, p is the fluid pressure, ρ is the fluid density, ν is the viscosity, \vec{f} is the body force exerted on the fluid, and t is time. The fluid is also assumed to have constant electrical conductivity σ .

For a two-dimensional flow, the vorticity ω and streamfunction ψ are introduced as follows.

$$\vec{\omega} = \nabla \times \vec{u} \quad (2.3a)$$

$$\vec{u}_x = \frac{\partial \psi}{\partial y} \quad (2.3b)$$

$$\vec{u}_y = -\frac{\partial \psi}{\partial x} \quad (2.3c)$$

The continuity and momentum equations can be translated in terms of vorticity and streamfunction equations.

$$\frac{\partial \vec{\omega}}{\partial t} + (\vec{u} \cdot \nabla) \vec{\omega} = \frac{1}{\rho} \nabla^2 \vec{\omega} + \frac{1}{\rho} \nabla \times \vec{f} \quad (2.4)$$

$$\nabla^2 \psi = -\omega \quad (2.5)$$

The cylindrical coordinates are introduced in a natural manner to match the geometry of the circular cylinder. Equations (2.4) and (2.5) then become

$$\frac{\partial \omega}{\partial t} + u_r \frac{\partial \omega}{\partial r} + \frac{u_\theta}{r} \frac{\partial \omega}{\partial \theta} = \nu \left[\frac{1}{r} \frac{\partial}{\partial r} \left(r \frac{\partial \omega}{\partial r} \right) + \frac{1}{r^2} \frac{\partial^2 \omega}{\partial \theta^2} \right] + \frac{1}{\rho} \left[\frac{1}{r} \frac{\partial (r f_\theta)}{\partial r} - \frac{1}{r} \frac{\partial f_r}{\partial \theta} \right] \quad (2.6)$$

$$\frac{1}{r} \left(\frac{\partial}{\partial r} \left(r \frac{\psi}{\partial r} \right) \right) + \frac{1}{r^2} \frac{\partial^2 \psi}{\partial \theta^2} = -\omega \quad (2.7)$$

The corresponding dimensionless form of Equations (2.6) and (2.7) are then derived using the nondimensional variables shown in Table 2.1, where the uppercase letters are used for the original dimensional variables, and lowercase letters denote the dimensionless variables. Here, b denotes the cylinder radius and u_∞ refers to the velocity of the incoming flow at infinity.

Table 2.1 Nondimensionalized Parameters

$\Omega = \omega / (u_\infty / b)$	$\Psi = \psi / (b u_\infty)$
$U_r = u_r / u_\infty$	$U_\theta = u_\theta / u_\infty$
$r = r / b$	$\theta = \theta$
$T = t / (b / u_\infty)$	$N = \frac{f}{\rho u_\infty^2 / (2b)}$
$F_r = \frac{f_r}{ f }$	$F_\theta = \frac{f_\theta}{ f }$

The dimensionless vorticity and streamfunction equations can then be written as follows.

$$\frac{\partial \Omega}{\partial T} + U_r \frac{\partial \Omega}{\partial r} + \frac{U_\theta}{r} \frac{\partial \Omega}{\partial \theta} = \frac{2}{\text{Re}} \left[\frac{1}{r} \frac{\partial}{\partial r} \left(r \frac{\partial \Omega}{\partial r} \right) + \frac{1}{r^2} \frac{\partial^2 \Omega}{\partial \theta^2} \right] + \frac{1}{2} N \left[\frac{1}{r} \frac{\partial (r F_\theta)}{\partial r} - \frac{1}{r} \frac{\partial F_r}{\partial \theta} \right] \quad (2.8)$$

$$\frac{1}{r} \left(\frac{\partial}{\partial r} \left(r \frac{\partial \Psi}{\partial r} \right) \right) + \frac{1}{r^2} \frac{\partial^2 \Psi}{\partial \theta^2} = -\Omega \quad (2.9)$$

where $\text{Re} = \frac{2bu_\infty}{\nu}$ is the Reynolds number and $N = \frac{f}{\rho u_\infty^2 / (2b)}$ is the interaction

parameter representing the ratio of the body and inertia forces.

Another transformation of coordinates is now performed, using the exponential-polar coordinate system (ξ, η) , $r = e^{2\pi\xi}$ and $\theta = 2\pi\eta$. In the new system of coordinates, Equations (2.8) and (2.9) can be rewritten as

$$E \frac{\partial \Omega}{\partial T} + \frac{\partial(U_\xi \Omega)}{\partial \xi} + \frac{\partial(U_\eta \Omega)}{\partial \eta} = \frac{2}{\text{Re}} \left(\frac{\partial \Omega}{\partial \xi^2} + \frac{\partial^2 \Omega}{\partial \eta^2} \right) + \frac{1}{2} N E^{\frac{1}{2}} \left(\frac{\partial F_\eta}{\partial \xi} + 2\pi F_\eta - \frac{\partial F_\xi}{\partial \eta} \right) \quad (2.10)$$

$$\frac{\partial^2 \Psi}{\partial \xi^2} + \frac{\partial^2 \Psi}{\partial \eta^2} = -E \Omega \quad (2.11)$$

where U_ξ , U_η and E are defined as

$$U_\xi = \frac{\partial \Psi}{\partial \eta} = E^{\frac{1}{2}} U_r \quad (2.12a)$$

$$U_\eta = -\frac{\partial \Psi}{\partial \xi} = E^{\frac{1}{2}} U_\theta \quad (2.12b)$$

$$E = 4\pi^2 e^{4\pi\xi} \quad (2.12c)$$

2.2 Pressure Coefficient

The pressure coefficient takes the well-known expression at the location on the cylindrical surface defined by the angle θ that is measured from the front stagnation point of the circular cylinder.

$$C_p^\theta = \frac{p_\theta - p_\infty}{\frac{1}{2}\rho u_\infty^2} \quad (2.13)$$

where p_∞ is the pressure of the incoming flow at infinity; p_θ is the pressure on the cylindrical surface at the angle θ .

Introducing the subscript zero to denote the position of the front stagnation point of the circular cylinder, the above equation can be written as

$$C_p^\theta = \frac{1}{\frac{1}{2}\rho u_\infty^2}(p_\theta - p_0) - \frac{1}{\frac{1}{2}\rho u_\infty^2}(p_\infty - p_0) \quad (2.14)$$

Therefore, the pressure coefficient at an arbitrary angle θ on the cylinder surface is determined by the pressure difference between the front stagnation point and its local position on cylinder surface and the pressure difference between the incoming flow and the pressure at the stagnation point.

The first term on the right side of Equation (2.14) is obtained from the integral of the pressure along the streamline coinciding with the cylinder surface. Using the identity $\nabla^2 \vec{u} = \nabla(\nabla \cdot \vec{u}) - \nabla \times (\nabla \times \vec{u})$, the no-slip boundary condition on the cylinder surface, and the continuity equation $\nabla \cdot \vec{u} = 0$, on the cylinder surface the momentum equation reduces to

$$\frac{1}{\rho} \nabla p = \nu \nabla^2 \vec{u} + \frac{\vec{f}}{\rho} = -\nu \nabla \times \vec{\omega} + \frac{\vec{f}}{\rho} \quad (2.15)$$

In two-dimensional cylindrical coordinates, the curl expression is given by

$$\nabla \times \vec{\omega} = \frac{1}{r} \frac{\partial \omega}{\partial \theta} \vec{e}_r - \frac{\partial \omega}{\partial r} \vec{e}_\theta$$

and the component equations of Equation (2.15) can be explicitly written as

$$\frac{1}{\rho} \frac{\partial p}{\partial r} \Big|_{r=b} = \left[-\frac{v}{r} \frac{\partial \omega}{\partial \theta} + \frac{f_r}{\rho} \right]_{r=b} \quad (2.16a)$$

$$\frac{1}{\rho r} \frac{\partial p}{\partial \theta} \Big|_{r=b} = \left[v \frac{\partial \omega}{\partial r} + \frac{f_\theta}{\rho} \right]_{r=b} \quad (2.16b)$$

Introducing the dimensionless pressure P as

$$P = \frac{p}{\frac{1}{2} \rho u_\infty^2}, \quad (2.17)$$

Equation (2.16) becomes

$$\frac{1}{\rho} \frac{\partial P}{\partial r} \Big|_{r=1} = \left[-\frac{4}{\text{Re}} \frac{\partial \Omega}{\partial \theta} + N F_r \right]_{r=1} \quad (2.18a)$$

$$\frac{\partial P}{\partial r} \Big|_{r=1} = \left[\frac{4}{\text{Re}} \frac{\partial \Omega}{\partial r} + N F_\theta \right]_{r=1} \quad (2.18b)$$

Integrating Equation (2.18) in the θ -direction in the interval $[0, \theta]$, the first term in Equation (2.14) can be rewritten in terms of the dimensionless vorticity and body force.

$$\begin{aligned} \frac{P_\theta - P_0}{\frac{1}{2} \rho u_\infty^2} &= P_\theta - P_0 \\ &= \left[\frac{4}{\text{Re}} \int_0^\theta r \frac{\partial \Omega}{\partial r} d\theta + N \int_0^\theta r F_\theta d\theta \right]_{r=1} \\ &= \frac{4}{\text{Re}} \int_0^\theta \frac{\partial \Omega}{\partial \xi} d\eta + 4\pi N \int_0^\theta F_\theta d\eta \end{aligned} \quad (2.19)$$

The second term on the right side of Equation (2.14) can be manipulated in a similar fashion, from the integral of pressure along the horizontal streamline that reaches the front stagnation point of the circular cylinder. In the r -direction, the momentum equation is

$$\frac{\partial u_r}{\partial t} = -\frac{1}{\rho} \frac{\partial p}{\partial r} - u_r \frac{\partial u_r}{\partial r} - \frac{u_\theta}{r} \frac{\partial u_\theta}{\partial \theta} + \frac{u_\theta^2}{r} - \frac{v}{r} \frac{\partial \omega}{\partial \theta} + \frac{f_r}{\rho} \quad (2.20)$$

After integration in the r - direction from b to ∞ , the difference of pressure between infinity and the front stagnation point takes the expression

$$\frac{1}{\rho} (p_\infty - p_0) = - \int_b^\infty \left[\frac{\partial u_r}{\partial t} - u_r \frac{\partial u_r}{\partial r} - \frac{u_\theta}{r} \frac{\partial u_\theta}{\partial \theta} + \frac{u_\theta^2}{r} - \frac{v}{r} \frac{\partial \omega}{\partial \theta} + \frac{f_r}{\rho} \right] dr \quad (2.21)$$

The above equation can be written in the (ξ, η) coordinates as follows.

$$\frac{p_\infty - p_0}{\frac{1}{2} \rho u_\infty^2} = -1 - 4\pi \int_b^\infty \frac{\partial U_r}{\partial t} e^{2\pi\xi} d\xi - 2 \int_b^\infty U_\theta \frac{\partial U_r}{\partial \eta} d\xi + 4\pi \int_b^\infty U_\theta^2 d\xi - \frac{4}{\text{Re}} \int_b^\infty \frac{\partial \Omega}{\partial \eta} d\xi \quad (2.22)$$

Substitution of Equations (2.19) and (2.22) into Equation (2.14) leads to the expression of the pressure coefficient in terms of the dimensionless variables in the new system of coordinates.

$$\begin{aligned} C_p^\theta = 1 + \frac{4}{\text{Re}} \int_b^\eta \frac{\partial \Omega}{\partial \eta} d\eta + 4\pi N \int_b^\eta F_\theta d\eta + 4\pi \int_b^\infty \frac{\partial U_r}{\partial t} e^{2\pi\xi} d\xi \\ + 2 \int_b^\infty U_\theta \frac{\partial U_r}{\partial \eta} d\xi - 4\pi \int_b^\infty U_\theta^2 d\xi + \frac{4}{\text{Re}} \int_b^\infty \frac{\partial \Omega}{\partial \eta} d\xi \end{aligned} \quad (2.23)$$

2.3 Force Coefficients

When the circular cylinder is immersed in the fluid, the cylinder experiences a net force due to the action of the fluid motion. The total force acting on the body, \vec{F}_t , is opposite and equal to the sum of the pressure and friction acting on the fluid. The expression of such force is obtained by integrating the shear stress and pressure along the cylinder surface.

$$\vec{F}_t = \vec{F}_p + \vec{F}_\tau = \iint_A \vec{p} dA + \iint_A \vec{\tau}_\omega dA \quad (2.24)$$

For the study of the two-dimensional flow, the cylinder can be considered of unit length in the axial z -direction. The component of \vec{F}_l parallel to the incoming flow is termed drag force and the component of \vec{F}_l orthogonal to the incoming flow is termed lift force. As recalled earlier, the total drag consists of skin friction and pressure drag. The friction drag can be obtained from the projection of the integral of the wall shear stress along the cylinder surface in the direction of the incoming flow. The pressure drag can be obtained from the projection of the integral of the pressure along the cylinder surface in the direction of the incoming flow. Therefore, the total drag is

$$F_x^D = F_{px} + F_{\tau x} = \int_0^{2\pi} rp \cos \theta d\theta + \int_0^{2\pi} r \tau_{r\theta} \sin \theta d\theta \quad (2.25)$$

Similarly, the total lift is

$$F_y^l = F_{py} + F_{\tau y} = - \int_0^{2\pi} rp \sin \theta d\theta + \int_0^{2\pi} r \tau_{r\theta} \cos \theta d\theta \quad (2.26)$$

Using Equation (2.16b), the first term in the right hand-side of Equation (2.25) can be written as follows

$$\begin{aligned} \frac{F_{px}}{\frac{1}{2} \rho u_\infty^2 d} &= \int_0^{2\pi} P \cos \theta d\theta \\ &= -\frac{2}{\text{Re}} \int_0^{2\pi} \frac{\partial \Omega}{\partial r} \sin \theta d\theta - 2N \int_0^{2\pi} F_\theta \sin \theta d\theta \end{aligned} \quad (2.27)$$

where $d = 2b$ is the cylinder diameter.

From the no-slip boundary condition $u_\theta = u_r = 0$ on the cylinder surface, it can be seen that $\frac{\partial u_r}{\partial \theta} = \frac{\partial u_\theta}{\partial \theta} = 0$ and that the vorticity reduces to $\omega = \nabla \times \vec{u} = \frac{\partial u_\theta}{\partial r}$. This leads to

the expression of the shear stress on the surface of the cylinder

$$\tau_{r\theta} = \mu \left[r \frac{\partial}{\partial r} \left(\frac{u_\theta}{r} \right) + \frac{1}{r} \frac{\partial u_r}{\partial \theta} \right] = \frac{1}{2} \rho u_\infty^2 \frac{4}{\text{Re}} \Omega_{surf} \quad (2.28)$$

Substitution of the above equation into Equation (2.25) gives

$$\frac{F_x}{\frac{1}{2} \rho u_\infty^2 d} = \frac{2}{\text{Re}} \int_0^{2\pi} \Omega_{surf} \sin \theta d\theta \quad (2.29)$$

Using the well-known generic expressions of the drag and lift coefficients

$$C_d = \frac{F_x^D}{\frac{1}{2} \rho u_\infty^2 d}, \quad (2.30a)$$

$$C_l = \frac{F_y}{\frac{1}{2} \rho u_\infty^2 d}, \quad (2.30b)$$

the drag and lift coefficients in the context of our problem become

$$\begin{aligned} C_d &= \frac{F_{px} + F_x}{\frac{1}{2} \rho u_\infty^2 d} \\ &= \frac{2}{\text{Re}} \int_0^1 \left(2\pi \Omega_{surf} - \frac{\partial \Omega_{surf}}{\partial \xi} \right) \sin(2\pi\eta) d\eta - 2\pi N \int_0^1 F_\theta \sin(2\pi\eta) d\eta \end{aligned} \quad (2.31)$$

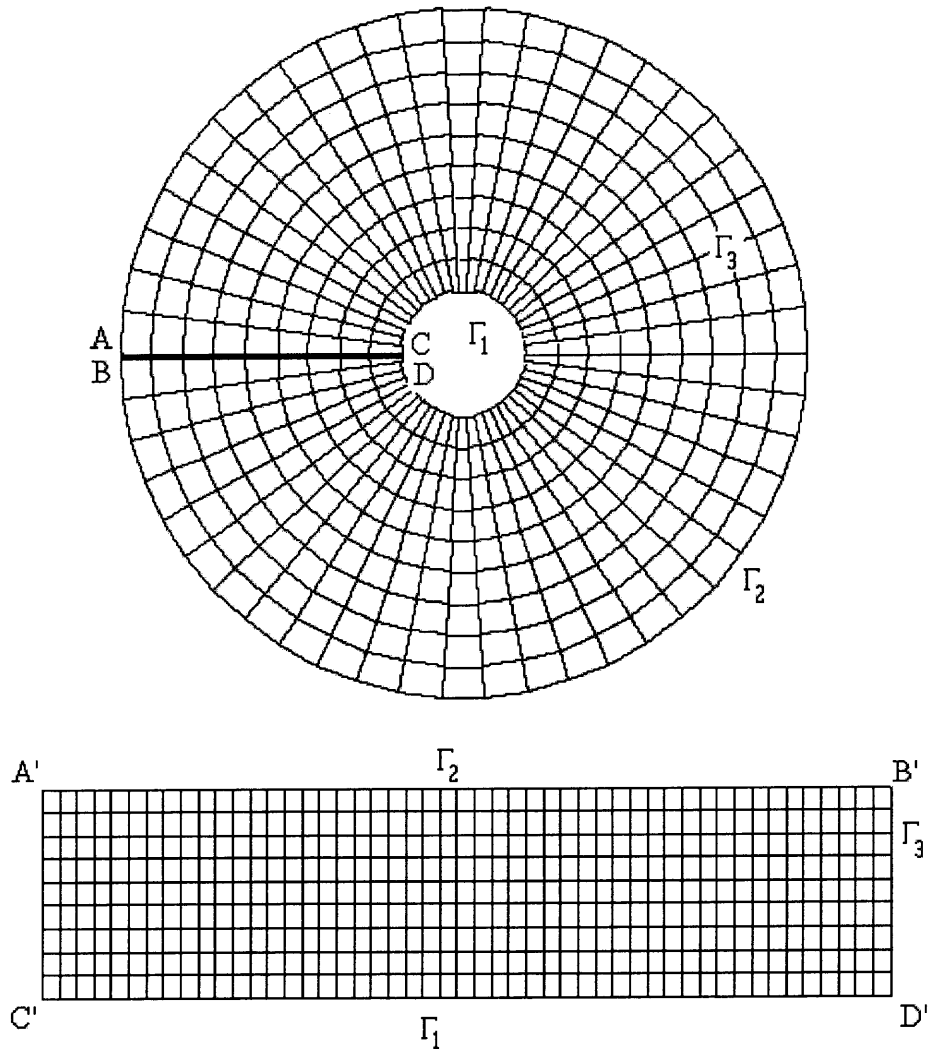
$$\begin{aligned} C_l &= \frac{F_{py} + F_y}{\frac{1}{2} \rho u_\infty^2 d} \\ &= \frac{2}{\text{Re}} \int_0^1 \left(2\pi \Omega_{surf} - \frac{\partial \Omega_{surf}}{\partial \xi} \right) \cos(2\pi\eta) d\eta - 2\pi N \int_0^1 F_\theta \cos(2\pi\eta) d\eta \end{aligned} \quad (2.32)$$

2.4 Discrete Form of the Equations and Numerical Algorithm

The nonlinear partial differential equations of motion in terms of the vorticity and streamfunction are too complicated to be solved analytically, in particular in the case of the circular cylinder geometry. The only option is to use numerical methods to solve such

equations. The two most obvious computational methods are the finite difference and finite element schemes. While both schemes require the domain to be discretized into a grid, the main difference lies in the manner in which the equations are discretized. Finite difference schemes use differentiation formula to replace each term in the partial differential equation while finite element algorithms use the variational method as a discretization technique. In general, the finite difference technique offers greater flexibility for complex differential operators and the finite element procedure adapts better to complex geometries. Navier-Stokes solvers have used both techniques due to the complexity of the differential operators involved, and the complex flow geometry of interest. In this dissertation, we restrict ourselves to the flow past a cylinder, which remains of rather simple geometry, and have selected the finite difference option.

In the numerical calculations presented in this dissertation, the physical circular domain ABCD in polar coordinates is transformed into the rectangular (ξ, η) domain A'B'C'D' (See Figure 2.1) through the $(r, \theta) \rightarrow (\xi, \eta)$ coordinate transformation. In this computational domain, the differential equations are transformed into discrete algebra equations defined on a preset mesh. The problem is then turned into a set of linear or quasi-linear equations that need to be solved at all mesh points. The computations presented in this dissertation are run on a mesh consisting of $N_1 \times N_2 = 1024 \times 512$ grid points in the r and θ directions, respectively. The subscripts i and j refer to the radial location (ξ) and azimuthal location (η) in the discrete computational domain with $1 \leq i \leq N_1$ and $1 \leq j \leq N_2+1$.



Domain transformation relation $\xi = \ln r / 2\pi, \eta = \theta / 2\pi$

Γ_1 , the cylinder surface

Γ_2 , the outer boundary of calculation domain

Γ_3 , movable boundary separating the viscous from the nonviscous flow

at Γ_1 , $\Psi = 0$, Ω determined from calculation

at Γ_2 , $\Omega = 0$, $\Psi = -2sh(2\pi\xi) \sin(2\pi\eta)$

at Γ_3 , $\Omega = 0$, Ψ determined from calculation

Figure 2.1 Computational domain for the simulation of the flow past a circular cylinder.

The streamfunction equation (2.11) is discretized in the following manner:

$$\frac{1}{\Delta\xi^2}(\Psi_{i-1,j} - 2\Psi_{i,j} + \Psi_{i+1,j}) + \frac{1}{\Delta\eta^2}(\Psi_{i,j+1} - 2\Psi_{i,j} + \Psi_{i,j+1}) = -\Omega_{i,j} \quad (2.33)$$

Solving the above equation is performed by using the method of Fast Fourier Transformation (Hockney, R.W. 1970). The basic idea is as follows. Let the number of mesh points be 2^n or $2^n \pm 1$ for a one-dimensional problem and take the periodic boundary condition as an example. Consider the three neighboring equations for variable ψ with q known at every point and t even

$$\psi_{t-2} + A\psi_{t-1} + \psi_t = q_{t-1} \quad (2.34a)$$

$$\psi_{t-1} + A\psi_t + \psi_{t+1} = q_t \quad (2.34b)$$

$$\psi_t + A\psi_{t+1} + \psi_{t+2} = q_{t+1} \quad (2.34c)$$

After manipulations leading to the elimination of ψ_{t-1} and ψ_{t+1} , one obtains

$$\psi_{t-2} + A^{(1)}\psi_t + \psi_{t+2} = q_t^{(1)} \quad (2.35a)$$

where

$$A^{(1)} = 2I - A^2 \quad (2.35b)$$

$$q_t^{(1)} = q_{t-1} - Aq_t + q_{t+1} \quad (2.35c)$$

The procedure can be reiterated for the following equations (with t even)

$$\psi_{t-4} + A^{(1)}\psi_{t-2} + \psi_t = q_{t-1}^{(1)} \quad (2.36a)$$

$$\psi_{t-2} + A^{(1)}\psi_t + \psi_{t+2} = q_t^{(1)} \quad (2.36b)$$

$$\psi_t + A^{(1)}\psi_{t+2} + \psi_{t+2} = q_{t+1}^{(1)} \quad (2.36c)$$

After n steps, the following relation is derived

$$\psi_{-N} + A^{(n)}\psi_0 + \psi_N = q_0^{(n)} \quad (2.37)$$

Since the computational domain is subjected to periodic conditions,

$\psi_{-N} = \psi_0 = \psi_N$, it follows that

$$\psi_0 = \frac{q_0^{(n)}}{A^{(n)} + 2} \quad (2.38)$$

From ψ_0 and ψ_N it is easy to find $\psi_{N/2}$ and so on. Thus, ψ is determined at every inner mesh point. The treatment of other boundary conditions and/or a two-dimensional (rather than one-dimensional) problem can be performed in a similar manner. The calculation accuracy is of the order of $\max(\Delta\xi^2, \Delta\eta^2)$.

Unlike the streamfunction equation that includes time implicitly, the vorticity equation includes a time derivative and, therefore, involves time explicitly. The Alternative Direction Implicit method (ADI) was used to solve this equation. The differentiation form of the vorticity equation is described as follows, where the subscripts i and j refer to the ξ and η direction, respectively.

j direction:

$$\begin{aligned} & E_i \frac{\Omega_{i,j}^{n+\frac{1}{2}} - \Omega_{i,j}^n}{\frac{1}{2}\Delta t} + \frac{(U_\eta \Omega^{n+\frac{1}{2}})_{i,j+1} - (U_\eta \Omega^{n+\frac{1}{2}})_{i,j-1}}{2\Delta\eta} - \frac{2}{\text{Re}} \frac{\Omega_{i,j+1}^{n+\frac{1}{2}} - 2\Omega_{i,j}^{n+\frac{1}{2}} + \Omega_{i,j-1}^{n+\frac{1}{2}}}{\Delta\eta^2} \\ & = - \frac{(U_\xi \Omega^n)_{i+1,j} - (U_\xi \Omega^n)_{i-1,j}}{2\Delta\xi} + \frac{2}{\text{Re}} \frac{\Omega_{i+1,j}^n - 2\Omega_{i,j}^n + \Omega_{i-1,j}^n}{\Delta\xi^2} \\ & + \frac{1}{2} N E_i^{\frac{1}{2}} \left(\frac{F_{\alpha+1,j} - F_{\alpha-1,j}}{2\Delta\xi} + 2\pi F_{\alpha,j} \right) \end{aligned} \quad (2.39a)$$

i direction:

$$\begin{aligned}
& E_i \frac{\Omega_{i,j}^{n+1} - \Omega_{i,j}^{n+\frac{1}{2}}}{\frac{1}{2}\Delta t} + \frac{(U_\xi \Omega^{n+1})_{i+1,j} - (U_\xi \Omega^{n+1})_{i-1,j}}{2\Delta\xi} - \frac{2}{\text{Re}} \frac{\Omega_{i+1,j}^{n+1} - 2\Omega_{i,j}^{n+1} + \Omega_{i-1,j}^{n+1}}{\Delta\xi^2} \\
&= - \frac{(U_\eta \Omega^{n+\frac{1}{2}})_{i,j+1} - (U_\eta \Omega^{n+\frac{1}{2}})_{i,j-1}}{2\Delta\eta} + \frac{2}{\text{Re}} \frac{\Omega_{i,j+1}^{n+\frac{1}{2}} - 2\Omega_{i,j}^{n+\frac{1}{2}} + \Omega_{i,j-1}^{n+\frac{1}{2}}}{\Delta\eta^2} \\
&+ \frac{1}{2} N E_i^{\frac{1}{2}} \left(\frac{F_{\alpha+1,j} - F_{\alpha-1,j}}{2\Delta\xi} + 2\pi F_{\alpha,j} \right)
\end{aligned} \tag{2.39b}$$

The main feature of ADI is a square matrix with nonzero entries on its three diagonal lines of the matrix. ADI has a truncated error of second order in time step Δt and spatial mesh size $\Delta\xi$ or $\Delta\eta$. Its accuracy is of the order of $\max(\Delta t^2, \Delta\xi^2, \Delta\eta^2)$.

2.5 Initial and Boundary Conditions

The fluid is considered at rest at $t = 0$ and impulsively started at $t = 0^+$. At that time, a uniform velocity u_∞ is imposed and maintained at later times. As time increases, the fluid flow develops from its rest position. Therefore, there is a need to describe the boundary conditions at $t = 0$ and $t > 0$ separately.

$t = 0$:

At $t = 0$, the fluid is in its static state in the entire domain, so that the streamfunction Ψ and vorticity Ω are zero everywhere, i.e. at $t = 0$, $\Psi = 0$ and $\Omega = 0$. At $t = 0^+$, a dimensionless uniform velocity $U_\infty = 1$ is instantaneously imposed. The initial condition for vorticity is still obviously zero everywhere, i.e. $\Omega = 0$. The streamfunction satisfies Laplace's equation at the initial time (see Equation (2.11)), that is

$$\frac{\partial^2 \Psi}{\partial \xi^2} + \frac{\partial^2 \Psi}{\partial \eta^2} = 0 \tag{2.40a}$$

When $x \rightarrow \infty$, the boundary condition is

$$\left. \frac{\partial \Psi}{\partial \xi} \right|_{\xi \rightarrow \infty} = -E^{\frac{1}{2}} \cos 2\pi\eta = -2\pi e^{2\pi\xi} \cos 2\pi\eta, \quad t = 0^+ \quad (2.40b)$$

Since it takes time for the velocity at infinity to reach the cylinder surface in a viscous fluid, the streamfunction on the cylinder surface at $t = 0^+$ is the same as what it was

at $t = 0$. Therefore, the streamfunction boundary condition on the surface of

the cylinder is

$$\Psi|_{\xi=0} = 0, \quad t = 0^+ \quad (2.41)$$

By using the method of separation of variables, it is assumed that $\Psi(\xi, \eta) = X(\xi)Y(\eta)$. Substitution into Equation (2.40) leads to

$$\frac{X''}{X} = -\frac{Y''}{Y} = \lambda^2 \quad (2.42)$$

Therefore, the solution for $X(\xi)$ and $Y(\eta)$ is given by

$$Y(\eta) = c_1 \cos(\lambda\eta) + c_2 \sin(\lambda\eta) \quad (2.43a)$$

$$X(\xi) = c_3 e^{-\lambda\xi} + c_4 e^{\lambda\xi} \quad (2.43b)$$

In the η -direction, the streamfunction is periodic, i.e. for any ξ and η , it satisfies

$$\Psi(\xi, \beta) = \Psi(\xi, \beta + 2\pi) \quad (2.44)$$

Combining the latter with Equation (2.43a), it is found that $\lambda = 2\pi$. Therefore, the streamfunction takes the expression

$$\Psi = -2sh(2\pi\xi) \sin(2\pi\eta) \quad (2.45)$$

In conclusion, the flow initial condition at $t = 0^+$ is given by zero vorticity ($\Omega = 0$) and by the streamfunction drawn from Equation (2.45).

$t > 0$:

Far away from the cylinder, the flow is assumed to be potential, and therefore the boundary condition is

$$t > 0: \text{ for } \xi \rightarrow \xi_\infty, \Psi = -2sh(2\pi\xi)\sin(2\pi\eta) \text{ and } \Omega = 0 \quad (2.46)$$

On the surface of the cylinder, the streamfunction Ψ is identically zero since there exists no suction or ejection. Because the investigated flow is incompressible viscous flow, the velocity on the cylinder surface is zero in order to satisfy the no-slip boundary condition.

Therefore $\frac{\partial^2 \Psi}{\partial \eta^2}$ vanishes on the cylinder surface. According to Equation (2.11), the

boundary condition on the cylinder surface at $t > 0$ is described as follows:

$$\Psi = 0 \text{ and } \Omega = -\frac{1}{E} \frac{\partial^2 \Psi}{\partial \xi^2} \text{ at } \xi = 0 \quad (2.47)$$

In order to save computing time, a moving boundary technique is used in the computation. In the domain between Γ_1 and Γ_2 , a circle Γ_3 is defined as the zero vorticity line if at all points on the circle vorticity is zero (or below a certain threshold for computation purposes). As the vorticity diffuses away from the solid boundary, Γ_3 is moved outward. The adaptive scheme is thus as follows. At every time step, the vorticity on Γ_3 is checked with a certain tolerance (for example, 10^{-15}). If the vorticity at every point located on Γ_3 is lower than the tolerance, Γ_3 is maintained at its present radial position. Otherwise, Γ_3 is moved outward with ΔN grid points in the azimuthal direction. The flow is free of vorticity outside Γ_3 . This method leads to the saving of a substantial amount of computing time.

In the numerical scheme, there is one additional boundary condition due to the fact that the sides A'C' and B'D' of the computational domain correspond to the same line in the original domain. This leads to the following additional periodic boundary condition in the azimuthal direction.

$$\Psi_{i,1} = \Psi_{i,N_2+1}, \quad 1 \leq i \leq N_1 \quad (2.48a)$$

and

$$\Omega_{i,1} = \Omega_{i,N_2+1}, \quad 1 \leq i \leq N_1 \quad (2.48b)$$

The side A'B' correspond to the outer boundary of the original physical domain. This side is defined by all points whose subscript is $i = N_1$. The intermediate boundary, or zero-vorticity circle, corresponds to $i = N_t$ such that $\Omega_{N_t,j} = 0$. It moves at every time step during the transient regime of the flow as the vorticity diffuses away from the cylinder so that N_t is not preset. Outside this circle, the streamfunction and vorticity satisfy the potential flow condition:

$$\Psi_{N_t,j} = -2sh(2\pi\xi_{N_t})\sin(2\pi\eta_j), \quad N_t \leq Nt \leq N_1 \quad 1 \leq j \leq N_2 \quad (2.49a)$$

$$\Omega_{N_t,j} = 0, \quad N_t \leq Nt \leq N_1 \quad 1 \leq j \leq N_2 \quad (2.49b)$$

On the cylinder surface, the streamfunction Ψ is set to be zero, that is

$$\Psi_{1,j} = 0, \quad 1 \leq j \leq N_2 \quad (2.50)$$

For all mesh points whose subscript $i = 1$ (cylinder surface), Equation (2.47) is used to get the vorticity on the cylinder surface. For all mesh points whose subscript $i = N_1$ (outer boundary) the vorticity is zero on the outer boundary.

2.6 Numerical Treatment of Vorticity on the Wall

The boundary condition for vorticity along the cylinder surface requires some special care. Analytically, the condition has the expression

$$\Omega_{1,j} = -\frac{1}{E} \frac{\partial^2 \Psi}{\partial \xi^2} \Big|_{1,j} \quad 1 \leq j \leq N_2 \text{ in which the second derivative of the streamfunction } \Psi$$

needs to be discretized. If such derivative is simply discretized as

$$\Omega_{1,j} = -\frac{1}{E(\xi_1)} \frac{\Psi_{1,j} - 2\Psi_{2,j} + \Psi_{3,j}}{(\Delta\xi)^2} \text{ (central scheme of second order accuracy), it implies}$$

$\Omega_{1,j} = \Omega_{2,j} \quad 1 \leq j \leq N_2$, which neglects the diffusion of vorticity close to the wall. An

alternative scheme is to rewrite $\Omega_{1,j} = -\frac{1}{E} \frac{\partial^2 \Psi}{\partial \xi^2} \Big|_{1,j}$ in terms of the velocity, that is

$$\Omega_{1,j} = -\frac{1}{E} \frac{\partial U_\eta}{\partial \xi} \Big|_{1,j} = -\frac{1}{E(\xi_1)} \frac{U_{2,j} - U_{1,j}}{\Delta\xi} \quad (5.51)$$

On the surface of the cylinder, the no-slip boundary condition implies that

$V_{1,j} = 0$ and $U_{1,j} = 0$ for $1 \leq j \leq N_2$, which means that $\frac{\partial \Psi}{\partial \xi} \Big|_{1,j} = 0$. Since the

streamfunction is also zero, $\Psi_{1,j} = 0$ for $1 \leq j \leq N_2$, one can write

$$U_{2,j} = \frac{\Psi_{3,j} - \Psi_{1,j}}{2\Delta\xi} = \frac{\Psi_{3,j}}{2\Delta\xi}, \text{ and therefore}$$

$$\Omega_{1,j} = -\frac{1}{E(\xi_1)} \frac{\Psi_{3,j}}{2(\Delta\xi)^2} \quad (2.52)$$

Then, by Taylor's expansion,

$$\Psi_{2,j} = \Psi_{1,j} + \left(\frac{\partial \Psi}{\partial \xi}\right)_{1,j} \Delta\xi + \frac{1}{2} \left(\frac{\partial^2 \Psi}{\partial \xi^2}\right)_{1,j} (\Delta\xi)^2 + \frac{1}{2!} \left(\frac{\partial^3 \Psi}{\partial \xi^3}\right)_{1,j} (\Delta\xi)^3 \quad (2.53)$$

$$\Psi_{3,j} = \Psi_{1,j} + \left(\frac{\partial\Psi}{\partial\xi}\right)_{1,j}(2\Delta\xi) + \frac{1}{2}\left(\frac{\partial^2\Psi}{\partial\xi^2}\right)_{1,j}(2\Delta\xi)^2 + \frac{1}{3!}\left(\frac{\partial^3\Psi}{\partial\xi^3}\right)_{1,j}(\Delta\xi)^3 \quad (2.54)$$

Since $\Psi_{1,j} = 0$, it follows that $\Psi_{2,j} = \frac{1}{4}\Psi_{3,j} + O((\Delta\xi)^3)$. From Equation (2.52), the vorticity on the cylinder surface is

$$\Omega_{1,j} = -\frac{1}{E(\xi_1)} \frac{2\Psi_{2,j}}{(\Delta\xi)^2} \quad (2.55)$$

Equation (2.33) with its boundary conditions (2.48a), (2.49a) and (2.50) is solved first. Then Equations (2.39a), (2.39b) and their boundary conditions (2.48b), (2.49b) and (2.55) are numerically integrating based on the knowledge of the vorticity Ω and the streamfunction Ψ .

CHAPTER 3

DISCUSSION OF LORENTZ FORCE IN PLATE CASE

3.1 Background

For fluids of non-zero electrical conductivity, an external body force, or Lorentz force, can be generated by the action of an electric and magnetic field. The expression of the Lorentz force is as follows.

$$\vec{F} = \vec{J} \times \vec{B} \quad (3.1)$$

where J refers to ... and B represents the

In the case of a fluid flow over a flat plate or a cylinder, electrodes and magnets can be placed in the wall of the plate or the cylinder in order to generate an electromagnetic field which, in turn, creates an electromagnetic force applied to the fluid. One configuration consists of electrodes and magnets that are arranged alternatively on the plate or the cylinder and generate a Lorentz force aligned in the flow direction, as shown in Figure 3.1 (Gailitis, A., 1961). Flow control using such a “stripes” arrangement has been studied mostly in the context of turbulent boundary layers (Hennoch and Stace, 1995; Crawford and Karniadakis, 1997). Another geometry, referred to as chessboard-like arranged electrodes/magnets or “tiles”, induces a wall-normal Lorentz force and has been explored for flat plate boundary layer flows as well (Nosenchuck and Brown, 1993; Fan and Brown, 1997; O’Sullivan and Biringen, 1998). Significant drag reductions were reported using this technique. A spanwise oscillating Lorentz force was also successfully used to reduce skin friction in a turbulent boundary layer (Berger *et al.*, 2000).

Grienberg (1961) calculated the Lorentz force generated by a stripes arrangement using a series expansion to determine the electromagnetic field distribution, assuming a periodical dependence in the x-direction. He found an exponentially decaying relation as

$$F = 2.87J_0B_0e^{-\frac{\pi y}{2a}} \quad (3.2)$$

where J_0 , B_0 , y and a denote the ..., respectively.

Under the assumption that the boundary condition for the electric and magnetic fields are of the form $J = J_0 \cos \frac{\pi x}{a}$, $-a \leq x \leq a$, $B = B_0 \cos \frac{\pi(x-a)}{a}$, $0 \leq x \leq 2a$, a similar analytical relation was found by Berger (2000):

$$F = J_0B_0e^{-\frac{\pi y}{a}} \quad (3.3)$$

although the factor 1/2 was missing in the exponential compared with Grienberg's expression (3.2).

In practice, the periodic cosine function is hard to impose. A more realistic boundary condition seems to be a Dirichlet boundary condition for the electric and magnetic potentials on the surface of the electrodes and magnets, provided that the junction points between the electrodes and magnets are well insulated and infinitely small. A novel analytical expression will be developed in the following section under such assumption.

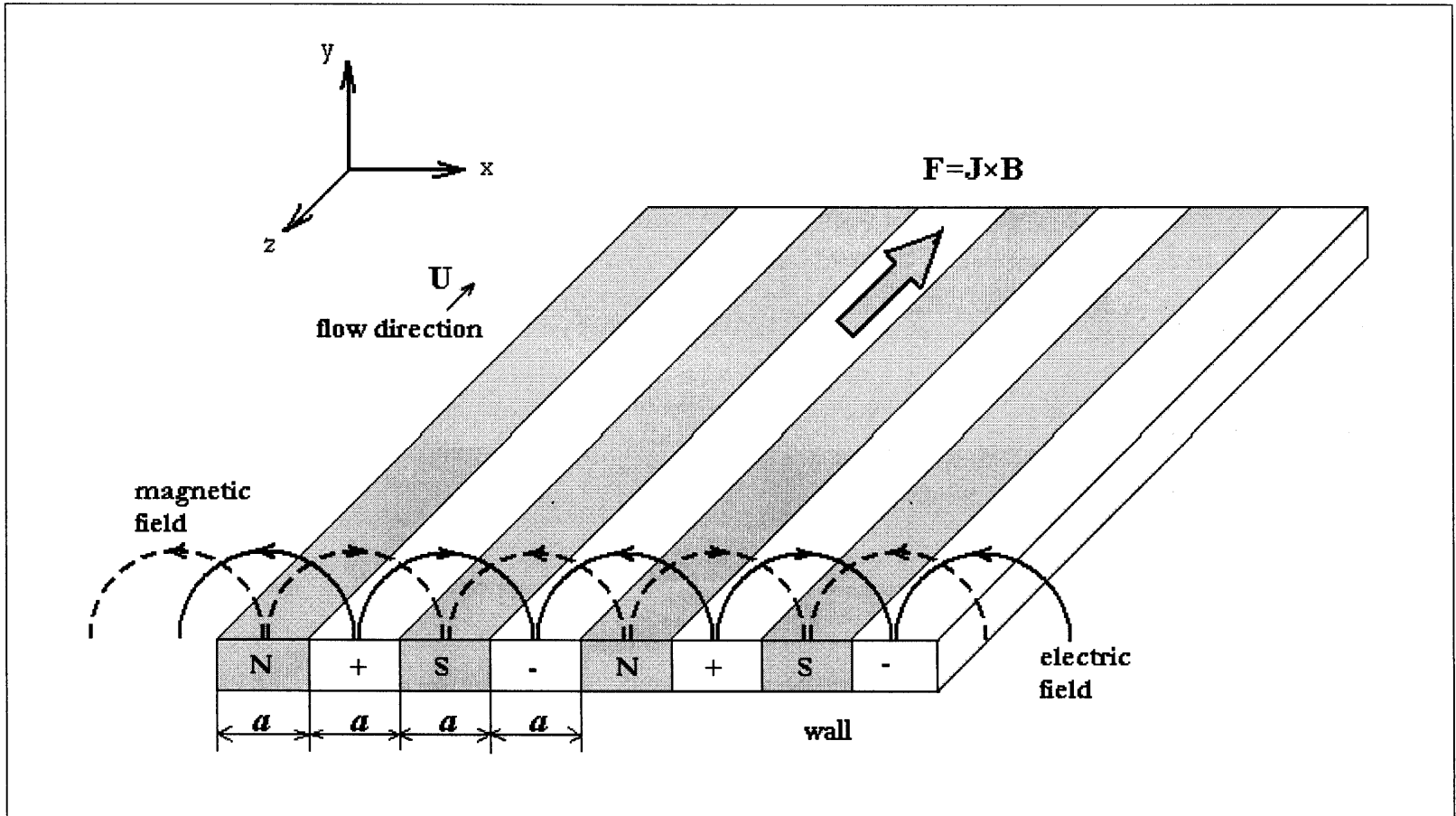


Figure 3.1 Scheme for the alternating arrangement of electromagnetic fields.

3.2 Governing Equations

From Maxwell's equations, it can be written that

$$\nabla \times E = -\sigma \frac{\partial B}{\partial t} \quad (3.4)$$

$$\nabla \times B = \mu_0 J_s \quad (3.5)$$

where μ_0 is the magnetic permeability.

Since seawater is a low conductivity ($\sigma \sim 10^{-3} \text{ ohm}^{-1}\text{mm}^{-1}$), low magnetic permeability ($\mu_0 \sim O(10^{-7})$) (Berger *et al.*, 2000), and quasi-neutral (charge density $\rho_e \approx 0$) (Crawford, 1997) medium, it is assumed that both the applied electric field and the magnetic field are independent of time and divergence free. Therefore,

$$\nabla \cdot B = 0 \quad (3.6)$$

$$\nabla \cdot E = \varepsilon_0 \rho_e \approx 0 \quad (3.7)$$

$$\nabla \times E = 0 \quad (3.8)$$

$$\nabla \times B = 0 \quad (3.9)$$

where ε_0 is the electric permeability.

Equations (3.8) and (3.9) imply that the electric and magnetic fields can be represented by the potential functions U and Φ respectively (Crawford and Karniadakis, 1997; Berger *et al.*, 2000) such that $E = -\nabla U$ and $B = \nabla \Phi$. Equations (3.6) to (3.9) then reduce to two Laplace equations

$$\nabla^2 U = 0 \quad (3.10)$$

$$\nabla^2 \Phi = 0 \quad (3.11)$$

With well-defined boundary conditions in the computational domain, Equations (3.10) and (3.11) are solved to determine the electric field intensity E and the magnetic

field intensity B . The Lorentz force is then deduced in the computational domain by using Equation (3.1).

3.3 Analysis of Lorentz Force in the Case of an Infinite Plate

For the case of a flow over an infinite plate, the Lorentz force is created by an alternating array of electrodes and magnetic rods (Figure 3.1). The respective spans of the electrodes and magnetic rods are identical and the generated Lorentz force is strictly streamwise, that is aligned with the flow. The electric and magnetic fields are periodic in the direction normal to the flow. The magnetic potential Φ at the center of each electrode is assumed to be zero by symmetry due to the alternative arrangement of the electrodes. Likewise, the electric potential U is zero at the center of each magnet. The two Laplace equations for the electric and magnetic potentials U and Φ are solved independently.

For the Laplace equation corresponding to the electric potential U , i.e. $\nabla^2 U = 0$, the computational domain is taken as a semi-infinite strip with width $2a$. Without loss of generality, the center of the positive electrode is selected as the origin (a similar analysis can be carried out if the center of the negative electrode is selected instead). The boundary condition for that domain is as follows (see Figure 3.2). The electric potential is assumed to be constant, say U_0 , on the surface of the electrodes and to satisfy the Dirichlet boundary condition $U = 0$ on the surface of the magnets. In the domain above the infinite plate, the electric potential function $U(x, y)$ satisfies Laplace's equation. Therefore, the electric potential problem can be described as

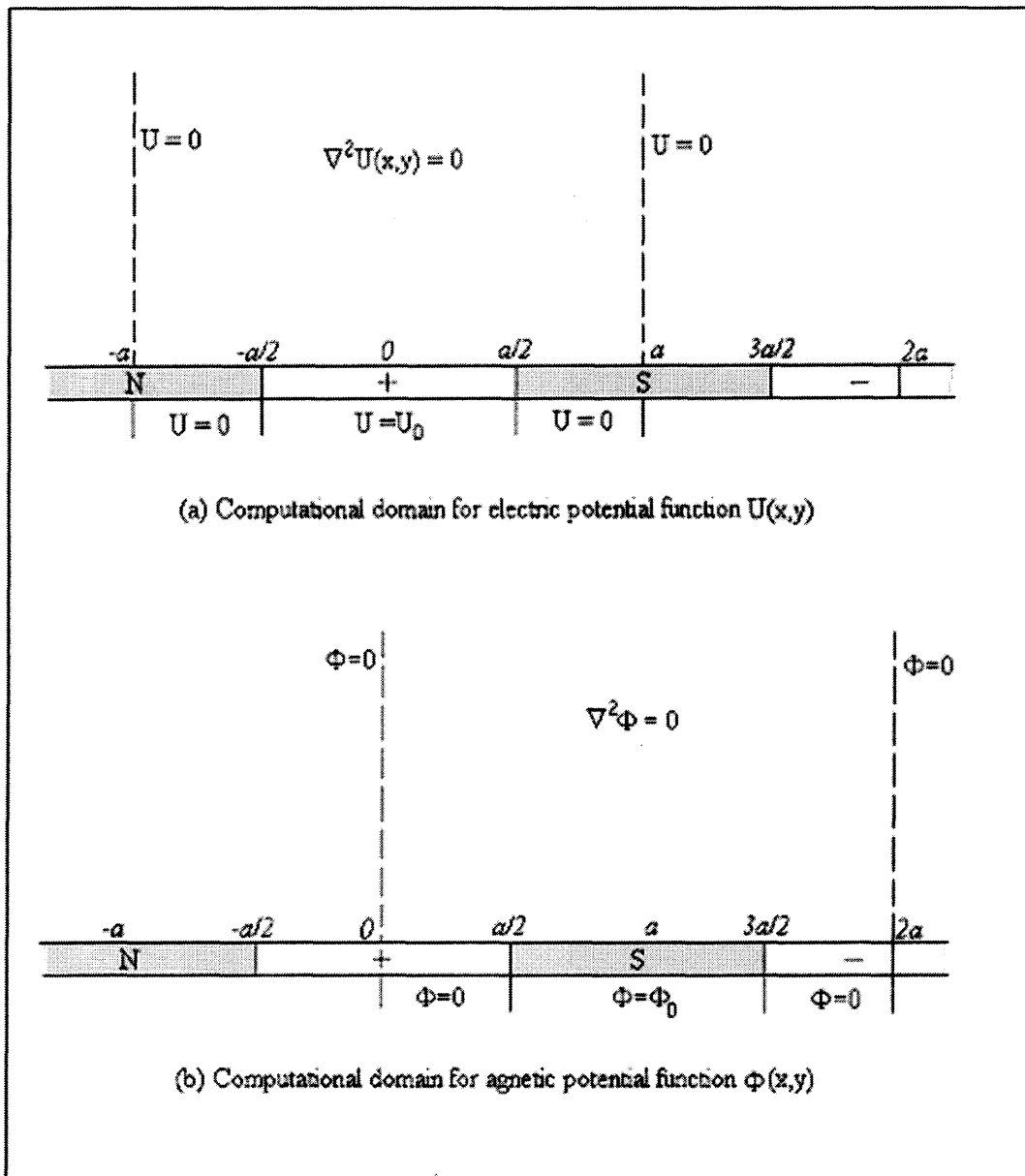


Fig 3.2 Computational domain for the electric and magnetic fields.

$$\frac{\partial^2 U}{\partial x^2} + \frac{\partial^2 U}{\partial y^2} = 0 \quad (3.12a)$$

$$\text{with } U(a, y) = 0 \text{ for } y \geq 0, \quad (3.12b)$$

$$U(-a, y) = 0 \text{ for } y \geq 0, \quad (3.12c)$$

$$U(x, 0) = \begin{cases} U_0, & -\frac{a}{2} < x < \frac{a}{2} \\ 0, & -a \leq x \leq -\frac{a}{2} \text{ or } \frac{a}{2} \leq x \leq a \end{cases} \quad (3.12d)$$

By the method of separation of variables, the solution of Equation (3.12) is found as

$$U(x, y) = \sum_{n=0}^{\infty} \frac{2U_0}{(n + \frac{1}{2})\pi} e^{-(n + \frac{1}{2})\frac{\pi y}{a}} \sin[(n + \frac{1}{2})\frac{\pi}{2}] \cos[(n + \frac{1}{2})\frac{\pi x}{a}] \quad (3.13)$$

The intensity of the electric field is then given by

$$\begin{aligned} \vec{J}(x, y) &= \sigma \nabla U \\ &= -\frac{2\sigma U}{a} \sum_{n=0}^{\infty} e^{-(n + \frac{1}{2})\frac{\pi y}{a}} \sin[(n + \frac{1}{2})\frac{\pi}{2}] \\ &\quad \cdot \left[\sin[(n + \frac{1}{2})\frac{\pi x}{a}] \vec{e}_x + \cos[(n + \frac{1}{2})\frac{\pi x}{a}] \vec{e}_y \right] \end{aligned} \quad (3.14)$$

Similarly, the equations satisfied by the magnetic potential function $\Phi(x, y)$ above the infinite plate can be written as

$$\frac{\partial^2 \Phi}{\partial X^2} + \frac{\partial^2 \Phi}{\partial y^2} = 0 \quad (3.15a)$$

$$\text{with } \Phi(a, y) = 0 \text{ for } y \geq 0 \quad (3.15b)$$

$$\Phi(-a, y) = 0 \text{ for } y \geq 0 \quad (3.15c)$$

$$\Phi(x, 0) = \begin{cases} \Phi_0, & \frac{a}{2} < x < \frac{3a}{2} \\ 0, & 0 \leq x \leq \frac{a}{2} \text{ or } \frac{3a}{2} \leq x \leq 2a \end{cases} \quad (3.15d)$$

The magnetic potential function $\Phi(x,y)$ and corresponding gradient $\vec{B}(x,y)$ are found as

$$\Phi(x,y) = \sum_{n=0}^{\infty} \frac{2\Phi_0}{(n+\frac{1}{2})\pi} e^{-\frac{(n+\frac{1}{2})\pi y}{a}} \sin[(n+\frac{1}{2})\frac{\pi}{2}] \cos[(n+\frac{1}{2})\frac{\pi(x-a)}{a}] \quad (3.16)$$

$$\begin{aligned} B &= \nabla\Phi \\ &= -\frac{2\Phi_0}{a} \sum_{n=0}^{\infty} e^{-\frac{(n+\frac{1}{2})\pi y}{a}} \sin[(n+\frac{1}{2})\frac{\pi}{2}] \\ &\quad \cdot \left[\sin[(n+\frac{1}{2})\frac{\pi(x-a)}{a}] \vec{e}_x + \cos[(n+\frac{1}{2})\frac{\pi(x-a)}{a}] \vec{e}_y \right] \end{aligned} \quad (3.17)$$

The Lorentz force can be found as the cross product of J and B , which can be written, after algebraic manipulations, as a double infinite series.

$$F(x,y) = \sum_{m=0}^{\infty} \sum_{n=0}^{\infty} F_{m,n}(x,y) \quad (3.18a)$$

$$\begin{aligned} F_{m,n}(x,y) &= (-1)^n \frac{4\sigma U_0 \Phi_0}{a^2} e^{-\frac{(m+n+1)\pi y}{a}} \\ &\quad \cdot \sin[(m+\frac{1}{2})\frac{\pi}{2}] \sin[(n+\frac{1}{2})\frac{\pi}{2}] \cos[(m-n)\frac{\pi x}{a}] \end{aligned} \quad (3.18b)$$

where the subscripts m and n refer to the frequencies due to the electric field and magnetic field, respectively.

Figures 3.3 and 3.4 show the distribution of the Lorentz force computed from Expression (3.18) retaining 50 terms in each series. This distribution in the z direction is approximately periodic, similarly to Grienberg's (1961) result.

The zeroth order term in the double series ($m = n = 0$), $F_{0,0} = \frac{2\sigma U_0 \Phi_0}{a^2} e^{-\frac{\pi y}{a}}$, is the

leading term away from the wall, i.e. $y \neq 0$.

When $m \neq n$, terms cancel each other since $F_{2k,2k+1} = -F_{2k+1,2k}$, $k = 0, 1, 2, 3$, etc.

When $m = n \neq 0$, $F_{n,n} = (-1)^n \frac{2\sigma U_0 \Phi_0}{a^2} e^{-\frac{(2n+1)\pi y}{a}}$. If $J_0 = \sigma \frac{U_0}{a}$ and $B_0 = \frac{\Phi_0}{a}$, the average

of the Lorentz force in the x -direction reduces to

$$F(y) = \frac{1}{2a} \int_{-a}^a F(x, y) dx = \sum_{n=0}^{\infty} F_{n,n} = J_0 B_0 \frac{2e^{-\frac{\pi y}{a}}}{1 + e^{-\frac{2\pi y}{a}}} \quad (3.19)$$

Equation (3.19) shows that the average of the Lorentz force is dependent on the distance to the wall as well as on the width of electrodes and magnets.

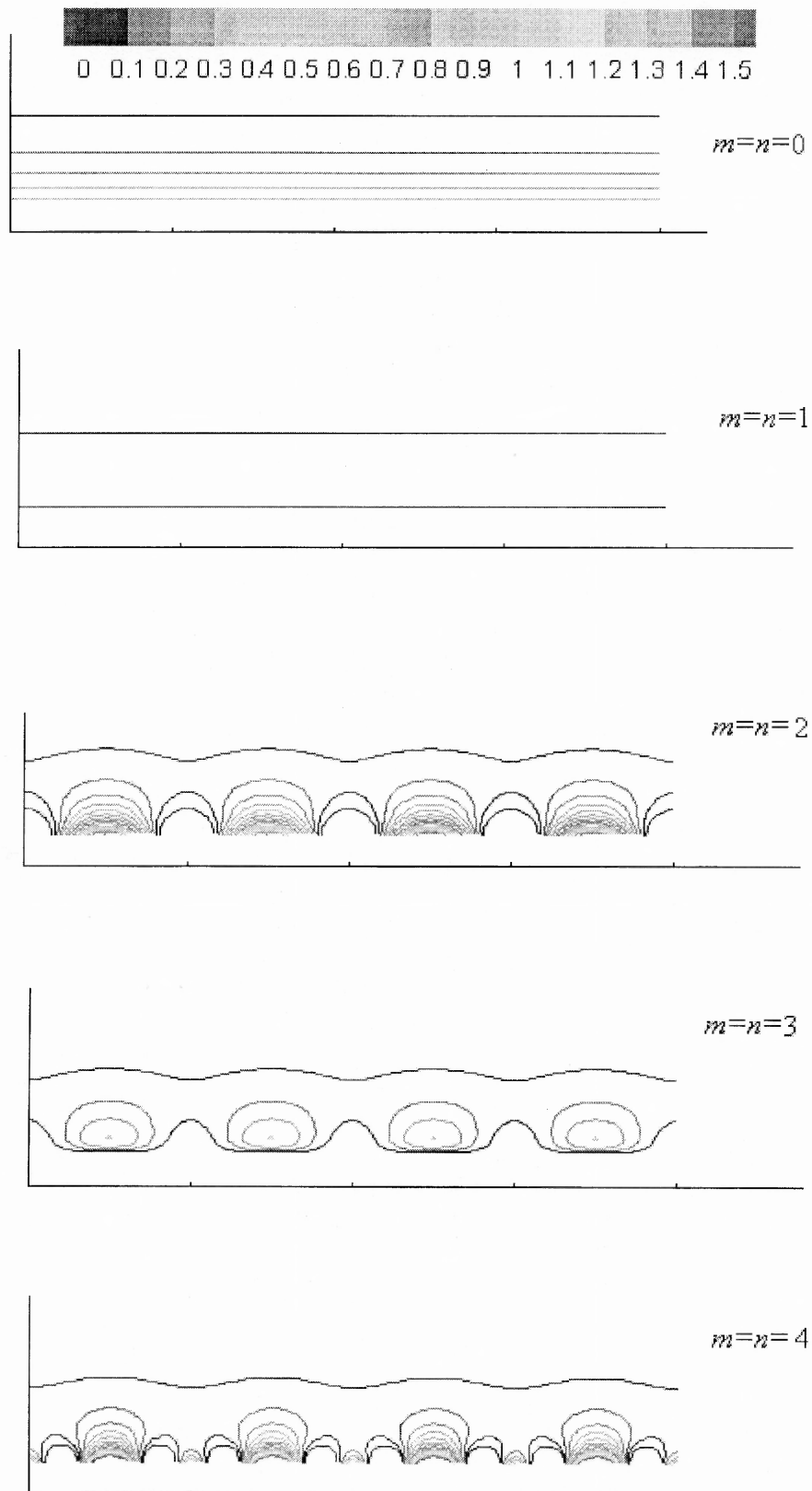


Figure 3.3 Distribution of the Lorentz force in the plate case with various terms in the summation.

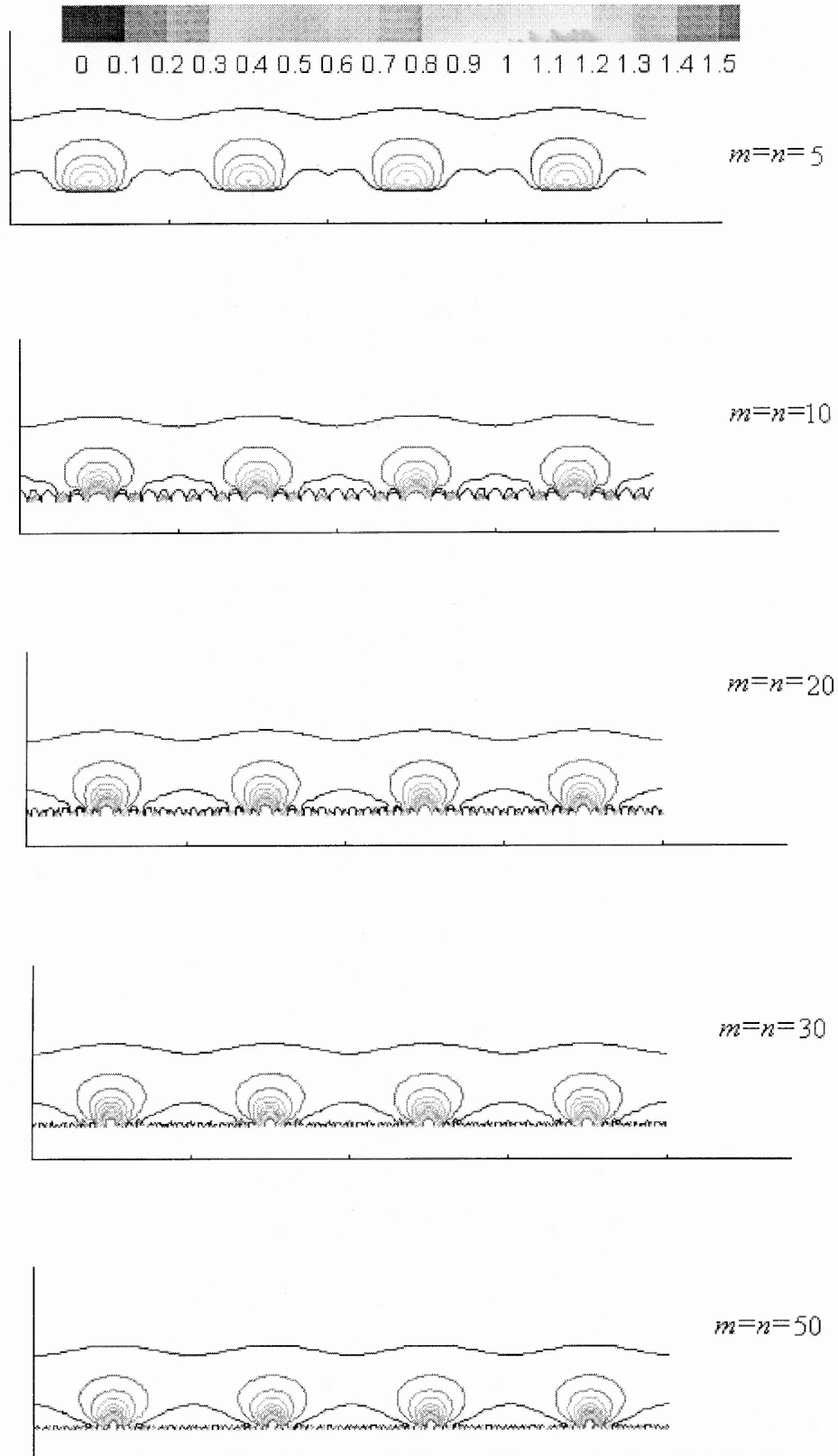


Figure 3.4 Distribution of the Lorentz force in the plate case with various terms in the summation (Continued).

3.4 Comparison of Numerical and Analytical Expression of Lorentz Force in Plate Case

Equations (3.12a) and (3.15a) are discretized by the second order central finite difference scheme with the subscripts i ($1 \leq i \leq M_x$) and j ($1 \leq j \leq M_y$) referring to the corresponding position in the x - and y -directions

$$\frac{U_{i-1,j} - 2U_{i,j} + U_{i+1,j}}{(\Delta x)^2} + \frac{U_{i,j-1} - 2U_{i,j} + U_{i,j+1}}{(\Delta y)^2} = 0 \quad (3.20)$$

$$\frac{\Phi_{i-1,j} - 2\Phi_{i,j} + \Phi_{i+1,j}}{(\Delta x)^2} + \frac{\Phi_{i,j-1} - 2\Phi_{i,j} + \Phi_{i,j+1}}{(\Delta y)^2} = 0 \quad (3.21)$$

In the numerical computations, the grid elements are given the same size in the x - and y -directions, that is $\Delta x = \Delta y = h$, and the computational domain is equal to $2a \times 40a$ where a is the width of the electrodes and magnets. The numerical tolerance for convergence is

such that $\frac{\max |U_{i,j}^{n+1} - U_{i,j}^n|}{U_0} \leq 1 \times 10^{-5}$ and $\frac{\max |\Phi_{i,j}^{n+1} - \Phi_{i,j}^n|}{\Phi_0} \leq 1 \times 10^{-5}$. The lateral and

wall boundary conditions are given by Equations (3.12b) to (3.12d) for the electric field and by Equations (3.15b) to (3.15d) for the magnetic field. The boundary value at the outer domain far away from the wall is simply set to zero for both electric and magnetic fields as it makes sense physically.

In order to save computing time, the over-relaxation method is used in order to accelerate the convergence of iteration calculations for both U and Φ :

$$W_{i,j}^{n+1} = W_{i,j}^n + \omega(W_{i,j}^* - W_{i,j}^n) \quad (3.22)$$

where $W_{i,j}$ is either $U_{i,j}$ or $\Phi_{i,j}$ depending on the calculation considered. The relaxation factor ω is constrained to be in the interval $1 < \omega < 2$. In the calculations, the value $\omega = 1.7$ is selected.

Figure 3.5 displays the electric and magnetic potentials, as well as the Lorentz force. Electric and magnetic potential functions vary continuously, except at the junction points of the electrodes and magnets. It follows that the Lorentz force changes dramatically in the x -direction (plate direction) in the vicinity of the plate surface. At distances from the plate roughly larger than half of the width a of the electrodes and magnets, the iso-contours of the Lorentz force are horizontal lines parallel to the flat plate, due to a quasi-uniform distribution of the Lorentz force in the direction of the plate.

Table 3.1 Numerical results for the average of the Lorentz force at the wall for different values $\frac{h}{2a}$ of mesh element sizes.

$\frac{h}{2a}$	$\frac{1}{10}$	$\frac{1}{20}$	$\frac{1}{30}$	$\frac{1}{40}$	$\frac{1}{50}$	$\frac{1}{60}$	$\frac{1}{70}$	$\frac{1}{80}$	$\frac{1}{90}$
$\frac{F_{wall}}{J_0 B_0}$	1.279	1.017	1.025	1.005	1.010	1.002	1.005	1.002	1.004
$\frac{h}{2a}$	$\frac{1}{100}$	$\frac{1}{110}$	$\frac{1}{120}$	$\frac{1}{130}$	$\frac{1}{140}$	$\frac{1}{150}$	$\frac{1}{160}$	$\frac{1}{170}$	$\frac{1}{180}$
$\frac{F_{wall}}{J_0 B_0}$	1.002	1.003	1.002	1.003	1.002	1.003	1.003	1.003	1.003

Table 3.1 shows the convergence of the numerical computations by displaying the averaged Lorentz force for different mesh element sizes. The numerical calculation shows that the averaged Lorentz force at the wall converges toward 1 as the size of the mesh element decreases. Indeed, Expression (3.19) applied at the wall ($y = 0$) reduces to

$$\left. \frac{F}{J_0 B_0} \right|_{y=0} = \frac{2e^{-\frac{\pi y}{a}}}{1 + e^{-\frac{2\pi y}{a}}} \Bigg|_{y=0} = 1 \quad (3.23)$$

This shows that the analytical expression given by Equation (3.19) is in good agreement with the numerical result at the wall. Figure 3.6 presents the comparison of the numerical results with the analytical expression derived in this dissertation for any distance from the wall. It can be seen that both curves are in excellent agreement in the entire computational domain.

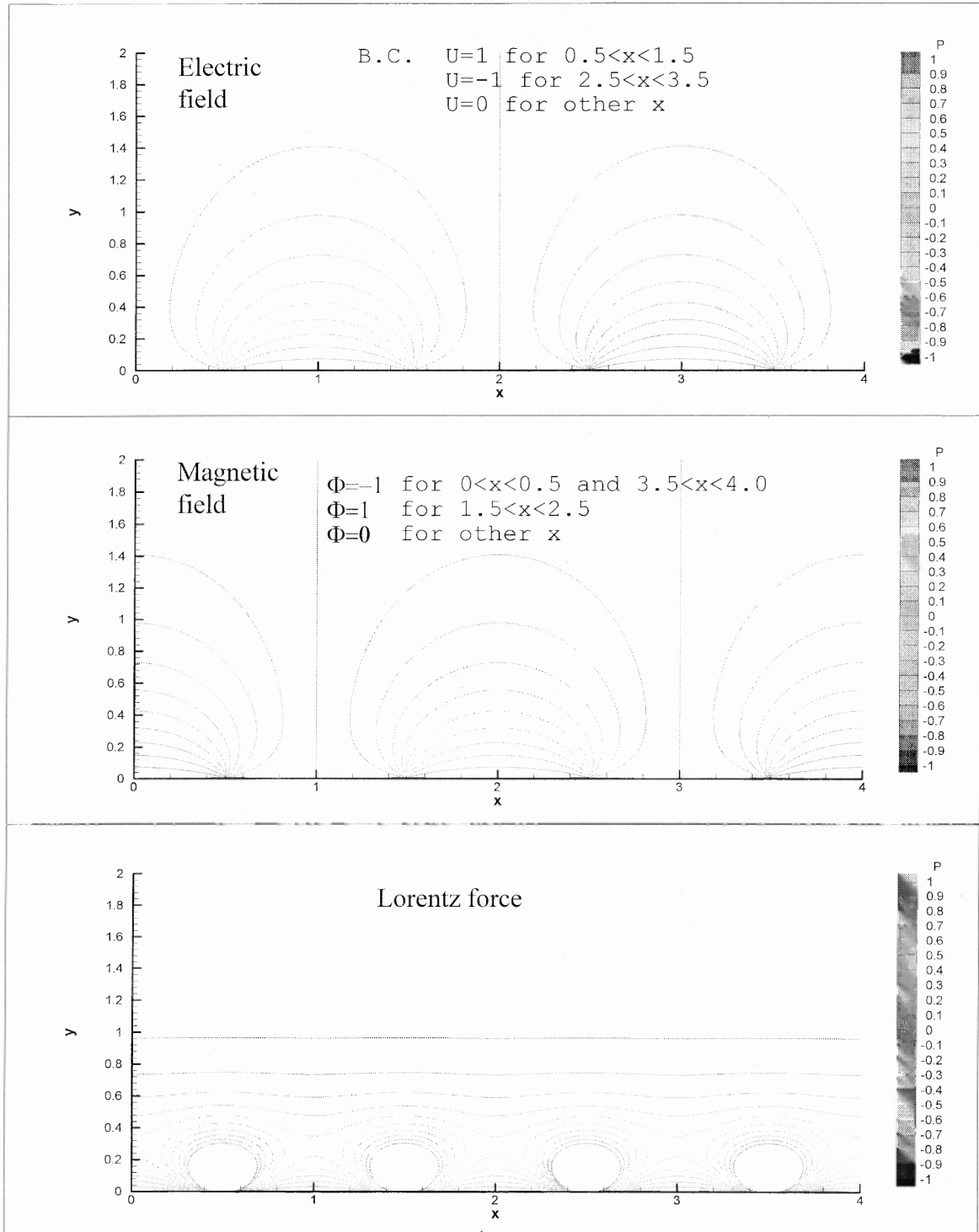


Figure 3.5 Numerical result for the electric and magnetic potential distributions and the corresponding Lorentz force.

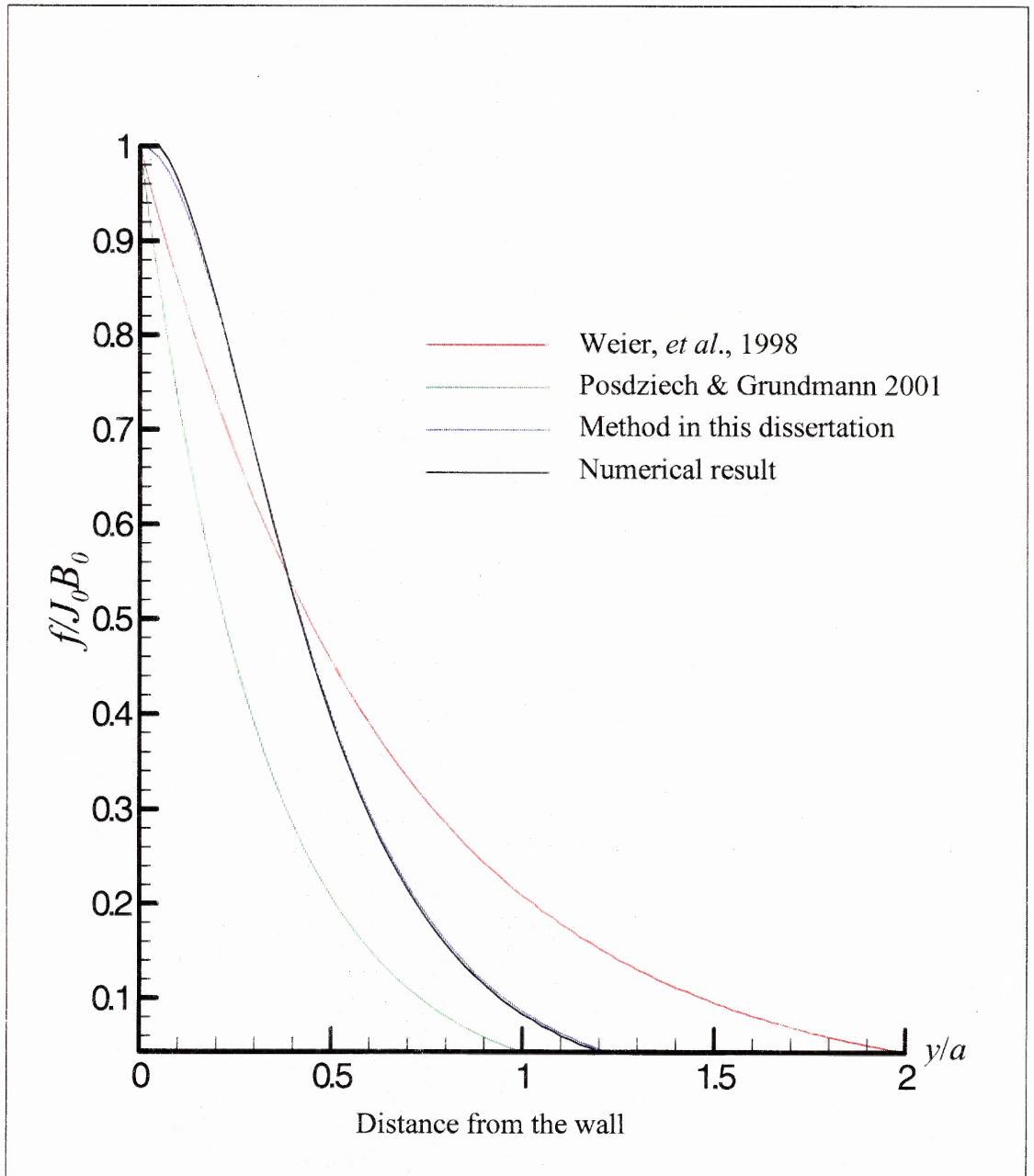


Figure 3.6 Comparison of the average Lorentz force in the case of a flat plate showing good agreement between the analytical and numerical results derived in this dissertation.

CHAPTER 4

ANALYSIS OF LORENTZ FORCE IN THE CASE OF AN INFINITE CIRCULAR CYLINDER

4.1 Introduction

Although there is evidence that an electromagnetic field can control vortex shedding past a cylinder in a conducting fluid, there has not been any quantitative analysis, either theoretical or experimental, of the Lorentz force generated.

While the postponement of flow separation on a circular cylinder was shown with crossed electric and magnetic fields more than ten years ago (Tsinober, 1989), the use of such a force for controlling vortex shedding has been published more recently (Weier *et al.* 1998; Posdziech and Grundmann, 2001; Kim and Lee, 2001). Nevertheless, due to the lack of discussion on the Lorentz force either analytically or experimentally, a considerable scatter of results was found, even on very similar arrangements.

Recalling the previous analysis of the generation of an electromagnetic field in the case of a flat plate, two alternative arrangements of electromagnets can be considered also in the case of a cylinder. Figure 4.1 shows an arrangement where the electric rods are arranged anti-symmetrically while the magnets are arranged symmetrically with respect to the midplane of the cylinder. The Lorentz force generated from the cross-product of the intensities of the electric and magnetic fields has a significant component in the direction tangential to the cylinder (azimuthal direction). When this component points in the flow direction, it has the potential to either defer or even suppress the generation of vortices from the cylinder surface.

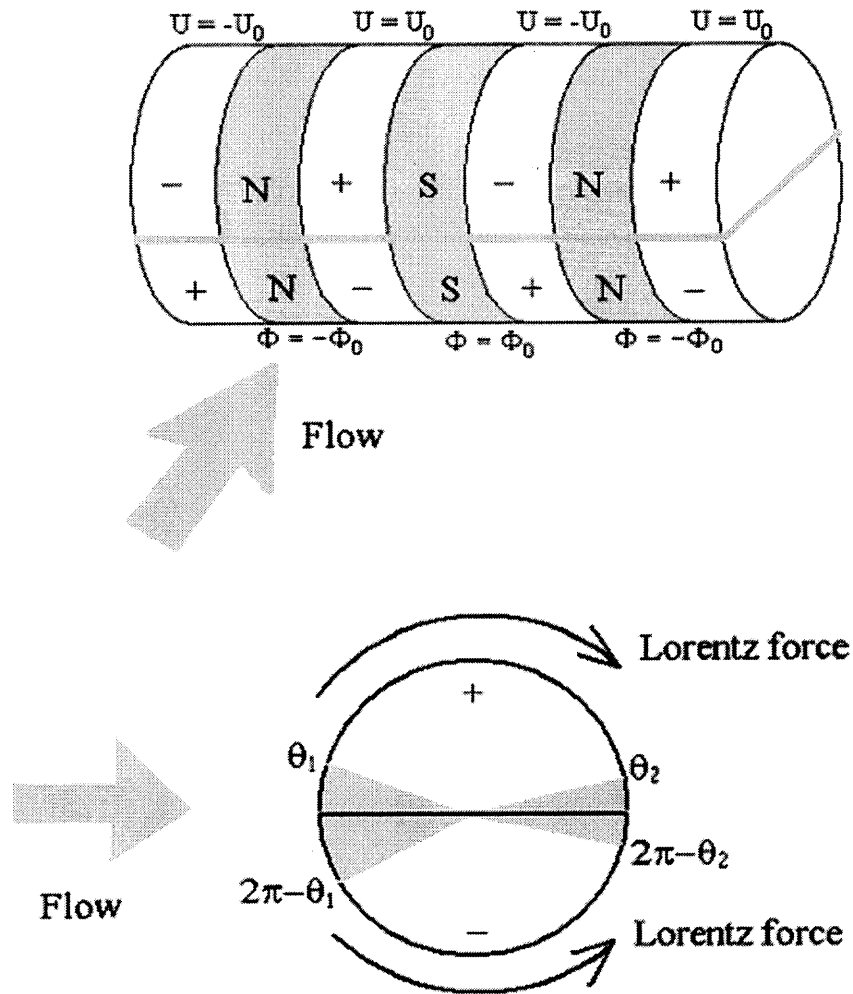


Figure 4.1 Alternating arrangement of electrodes and magnets generating a Lorentz force in the flow past a cylinder.

In past studies, researchers have considered only the azimuthal component of the force, extrapolating in an ad-hoc manner the expression of the force in the case of a flat plate as follows:

$$F = J_0 B_0 e^{-\frac{\pi y}{2a}} f(\theta), \quad y = r - b \quad (\text{Weier et al. 1998}) \quad (4.1)$$

or

$$F = J_0 B_0 e^{-\frac{\pi y}{a}} f(\theta), \quad y = r - b \quad (\text{Posdziech and Grundmann, 2001}) \quad (4.2)$$

where the distribution function $f(\theta)$ is defined by

$$f(\theta) = \begin{cases} -1, & \theta_1 < \theta \leq \theta_2 \\ 1, & 2\pi - \theta_2 < \theta \leq 2\pi - \theta_1 \\ 0, & \text{otherwise} \end{cases} \quad (4.3)$$

Here, a is the width of the electrodes and magnets; b is the radius of the cylinder; θ_1 and θ_2 are the beginning and ending angles of the electromagnetic actuation area on the upper semi-cylinder surface; $2\pi - \theta_2$ and $2\pi - \theta_1$ are the beginning and ending angles of the electromagnetic actuation area on the lower semi-cylinder surface. All angles are measured from the front stagnation point on the cylinder.

This expression is discontinuous in the θ -direction and the decay law in the y -direction is based on the assumption that the current density is sinusoidal on the wall ($J = J_0 \cos(\frac{\pi x}{2a})$) (Berger et al., 2000) or on series expansions (Grienberg, E. 1961).

Hereafter, this model is denoted as Discontinuous Model (DM). This discontinuity is obviously an artifact of the model. The goal of the present work is to get rid of the discontinuity, although it may have to be done at the expense of losing the model simplicity.

4.2 Numerical Method

The problem is first solved numerically by integrating the Laplace equation in three-dimensions and taking the force average in the axial direction in order to determine the force in the infinite cylinder case. According to the arrangement of electrodes and magnets shown in Figure 4.1, the governing equations and the corresponding boundary conditions for the electric and magnetic potential functions in cylindrical coordinates are as follows.

Electric potential function $U(r, \theta, x)$:

$$\frac{1}{r} \frac{\partial}{\partial r} \left(r \frac{\partial U}{\partial r} \right) + \frac{1}{r^2} \frac{\partial^2 U}{\partial \theta^2} + \frac{\partial^2 U}{\partial x^2} = 0 \quad (4.4a)$$

$$U(r, \theta, x) = \begin{cases} U_0, & -\frac{a}{2} < x < \frac{a}{2}, \quad \theta_1 < \theta < \theta_2 \\ 0, & -a \leq x \leq -\frac{a}{2} \quad \text{or} \quad \frac{a}{2} \leq x \leq a, \quad \theta \text{ arbitrary} \end{cases} \quad (4.4b)$$

$$U(r, \theta, x) = \begin{cases} -U_0, & -\frac{a}{2} < x < \frac{a}{2}, \quad 2\pi - \theta_2 < \theta < 2\pi - \theta_1 \\ 0, & -a \leq x \leq -\frac{a}{2} \quad \text{or} \quad \frac{a}{2} \leq x \leq a, \quad \theta \text{ arbitrary} \end{cases} \quad (4.4c)$$

$$U(r, \theta, a) = U(r, 0, -a) = 0, \quad r \geq b, \quad \theta \text{ arbitrary} \quad (4.4d)$$

Magnetic potential function $\Phi(r, \theta, x)$:

$$\frac{1}{r} \frac{\partial}{\partial r} \left(r \frac{\partial \Phi}{\partial r} \right) + \frac{1}{r^2} \frac{\partial^2 \Phi}{\partial \theta^2} + \frac{\partial^2 \Phi}{\partial x^2} = 0 \quad (4.5a)$$

$$\Phi(b, \theta, x) = \begin{cases} \Phi_0, & \frac{a}{2} < x < \frac{3a}{2}, \quad \theta_1 < \theta < \theta_2 \quad \text{or} \quad 2\pi - \theta_2 < \theta < 2\pi - \theta_1 \\ 0, & 0 \leq x \leq \frac{a}{2} \quad \text{or} \quad \frac{3a}{2} \leq x \leq 2a, \quad \theta \text{ arbitrary} \end{cases} \quad (4.5b)$$

$$\Phi(r, \theta, 0) = 0, \quad r \geq b, \quad \theta \text{ arbitrary} \quad (4.5c)$$

$$\Phi(r, \theta, 2a) = 0, \quad r \geq b, \quad \theta \text{ arbitrary} \quad (4.5d)$$

Let $r = e^{2\pi\xi}$, $\theta = 2\pi\eta$ and $E(\xi) = 4\pi^2 e^{4\pi\xi}$, Equations (4.4a) and (4.5a) become

$$\frac{\partial^2 W}{\partial \xi^2} + \frac{\partial^2 W}{\partial \eta^2} + E(\xi) \frac{\partial^2 W}{\partial x^2} = 0 \quad (4.6)$$

where $W(\xi, \eta, x) = U(r, \theta, x)$ or $W(\xi, \eta, x) = \Phi(r, \theta, x)$.

The selected finite difference scheme is

$$\delta_\xi^2 W_{i,j,k} + \delta_\eta^2 W_{i,j,k} + E(\xi_i) \delta_x^2 W_{i,j,k} = 0 \quad (4.7a)$$

where

$$\delta_\xi^2 W_{i,j,k} = \frac{2}{\Delta \xi_{i-1} + \Delta \xi_i} \left(\frac{W_{i+1,j,k} - W_{i,j,k}}{\Delta \xi_i} - \frac{W_{i,j,k} - W_{i-1,j,k}}{\Delta \xi_{i-1}} \right) \quad (4.7b)$$

$$\delta_\eta^2 W_{i,j,k} = \frac{W_{i,j-1,k} - 2W_{i,j,k} + W_{i,j+1,k}}{(\Delta \eta)^2} \quad (4.7c)$$

$$\delta_x^2 W_{i,j,k} = \frac{W_{i,j,k-1} - 2W_{i,j,k} + W_{i,j,k+1}}{(\Delta x)^2} \quad (4.7d)$$

The subscripts i , j , and k correspond to ξ , η and x coordinates respectively and $\Delta \xi_i = \xi_{i+1} - \xi_i$. The boundary values are determined by the corresponding boundary conditions for $W(\xi, \eta, x) = U(r, \theta, x)$ or $W(\xi, \eta, x) = \Phi(r, \theta, x)$.

The boundary conditions for the electric and magnetic potential functions have certain discontinuities at specific locations. Numerical calculations, however, require that the boundary conditions be smooth for convergence. This issue is addressed by expanding in terms of a Fourier series the original discontinuous boundary condition, or step function, and imposing that the approximation function goes through the average value at the discontinuity point. Equation (4.7a) is a matrix equation that can be solved by iteration.

After the calculation reaches convergence, the Lorentz force is determined by finite difference according to the formula

$$\begin{aligned}
\bar{F}(r, \theta, x) &= \sigma(\delta_r^2 U_{i,j,k} \bar{i}_r + \frac{1}{r} \delta_\theta^2 U_{i,j,k} \bar{i}_\theta + \delta_x^2 U_{i,j,k} \bar{i}_x) \\
&\quad \times (\delta_r^2 U_{i,j,k} \bar{i}_r + \frac{1}{r} \delta_\theta^2 U_{i,j,k} \bar{i}_\theta + \delta_x^2 U_{i,j,k} \bar{i}_x) \\
&= F_r(r, \theta, x) \bar{i}_r + F_\theta(r, \theta, x) \bar{i}_\theta + F_x(r, \theta, x) \bar{i}_x
\end{aligned} \tag{4.8}$$

In order to compare the three dimensional result of the numerical solution and the two dimensional expression of the DM model, it is necessary to take the average of the three-dimensional force in the axial direction, that is

$$F_j(r, \theta) = \frac{1}{2a} \int_{-a}^a F_j(r, \theta, x) dx \tag{4.9}$$

where the subscript j refers to the r , θ and x -components of the Lorentz force. The numerical simulation results will be presented in the next section when it is possible to compare them with analytical expressions.

4.3 Analytical Investigation

In order to obtain the Lorentz force in the cylindrical case analytically, the method of separation of variables is used to solve Equations (4.4) and (4.5). Since the electrodes follow an anti-symmetric arrangement and the magnets a symmetric arrangement (see Figure 4.1), it is sufficient to determine the electromagnetic field in the upper semi-cylinder. In this case, the additional boundary condition for the electric and magnetic fields are as follows.

$$U(r, 0, x) = U(r, \pi, x) = 0, r \geq b \tag{4.4e}$$

$$\frac{d\Phi}{d\theta}(r, 0, x) = \frac{d\Phi}{d\theta}(r, \pi, x) = 0, r \geq b \tag{4.5e}$$

Letting $U(r, \theta, x) = R(r)G(\theta)X(x)$ and substituting in Equation (4.4a) yields

$$\frac{1}{X} \frac{\partial^2 X}{\partial x^2} = -\lambda_m^2; \quad X(-a) = X(a) = 0 \quad (4.10a)$$

$$\frac{1}{G} \frac{\partial^2 G}{\partial \theta^2} = -\lambda_n^2; \quad G(0) = G(\pi) = 0 \quad (4.10b)$$

and

$$\frac{1}{r} \frac{\partial}{\partial r} \left(r \frac{\partial R}{\partial r} \right) - \left(\lambda_m^2 + \frac{\lambda_n^2}{r^2} \right) R = 0; \quad R(r) < \infty \quad (4.10c)$$

The eigenvalues of Equations (4.5a) and (4.5b) are

$$\lambda_m = \left(m + \frac{1}{2} \right) \frac{\pi}{a} \quad (4.11)$$

$$\lambda_n = n \quad (4.12)$$

Equation (4.10c) is a modified Bessel equation. The characteristic solutions of Equations (4.10a), (4.10b) and (4.10c) subjected to the above boundary conditions are

$$X(x) = \cos \lambda_m x \quad (4.13a)$$

$$G(\theta) = \sin n\theta \quad (4.13b)$$

$$R(r) = K_n(\lambda_m r) \quad (4.13c)$$

where

$$\begin{aligned} K_n(x) = & \frac{1}{2} \sum_{k=0}^{n-1} (-1)^k \frac{(n-k-1)!}{k!} \left(\frac{x}{2} \right)^{2k-n} \\ & + (-1)^{n+1} \sum_{k=0}^{\infty} \frac{1}{k!(n+k)!} \left[\ln \frac{x}{2} - \frac{1}{2} \psi(n+k+1) - \frac{1}{2} \psi(k+1) \right] \left(\frac{x}{2} \right)^{2k+n} \end{aligned} \quad (4.14)$$

$K_n(\cdot)$, $n = 0, 1, 2, \dots$, is the modified Bessel function of second kind with

$$\psi(z) = -\gamma - \frac{1}{z} + z \sum_{k=1}^{\infty} \frac{1}{k(z+k)}, \quad \gamma \text{ being the Euler constant.}$$

Therefore, the general solution

of the electric potential takes the expression

$$U(r, \theta, x) = \sum_{m=0}^{\infty} \sum_{n=1}^{\infty} A_{mn} K_n(\lambda_m r) \sin n\theta \cos \lambda_m x \quad (4.15a)$$

where m and n are integers and A_{mn} are the coefficients determined by the boundary conditions from Equations (4.4b) to (4.4e) such that

$$A_{mn} = \frac{4U_0}{\lambda_m a n \pi} \frac{\sin \frac{\lambda_m a}{2}}{K_n(\lambda_m b)} (\cos n\theta_1 - \cos n\theta_2) \quad (4.15b)$$

Similarly, the solution for the magnetic potential function can be found from its governing Equation (4.5) and corresponding boundary conditions as

$$\Phi(r, \theta, x) = \sum_{p=0}^{\infty} \sum_{q=1}^{\infty} \frac{4\Phi_0}{\lambda_p a q \pi} \frac{K_q(\lambda_p r)}{K_q(\lambda_p b)} \cdot (\cos q\theta_1 - \cos q\theta_2) \sin\left(\frac{\lambda_p a}{2}\right) \sin q\theta \cos \lambda_p (x - a) \quad (4.16)$$

$$\text{with } \lambda_p = \left(p + \frac{1}{2}\right) \frac{\pi}{a} \quad (4.17)$$

where p and q are integers.

Equations (4.15) and (4.16) show that, the aspect ratio $\frac{a}{b}$ plays an important role in the distribution of the potentials U and Φ in terms of $K_n(\cdot)$ which is the modified Bessel functions of second kind. The Lorentz force in such an arrangement can be deduced from the cross product

$$F(r, \theta, x) = \sigma \nabla U \times \nabla \Phi = F_r(r, \theta, x) \vec{i}_r + F_\theta(r, \theta, x) \vec{i}_\theta + F_x(r, \theta, x) \vec{i}_x \quad (4.18a)$$

where

$$\begin{aligned}
F_r(r, \theta, x) = & -\frac{a}{r} \sum_{m=0}^{\infty} \sum_{n=1}^{\infty} \sum_{p=0}^{\infty} \sum_{q=1}^{\infty} \frac{16J_0 B_0}{\pi^2} \frac{K_n(\lambda_m r)}{K_n(\lambda_m b)} \frac{K_q(\lambda_p r)}{K_q(\lambda_p b)} \\
& \cdot \sin \lambda_m \frac{a}{2} \sin \lambda_p \frac{a}{2} (\cos n\theta_1 - \cos n\theta_2)(\sin q\theta_2 - \sin q\theta_1) \\
& \cdot \left\{ \frac{\cos n\theta \cos q\theta \cos \lambda_m x \sin \lambda_p (x-a)}{\lambda_m q} - \frac{\sin n\theta \sin q\theta \sin \lambda_m x \cos \lambda_p (x-a)}{\lambda_p n} \right\}
\end{aligned} \tag{4.18b}$$

$$\begin{aligned}
F_\theta(r, \theta, x) = & \sum_{m=0}^{\infty} \sum_{n=1}^{\infty} \sum_{p=0}^{\infty} \sum_{q=1}^{\infty} \frac{16J_0 B_0}{nq\pi^2} \frac{K_n(\lambda_m r)K_q(\lambda_p r)}{K_n(\lambda_m b)K_q(\lambda_p b)} \sin \lambda_m \frac{a}{2} \sin \lambda_p \frac{a}{2} \\
& \cdot (\cos n\theta_1 - \cos n\theta_2)(\sin q\theta_2 - \sin q\theta_1) \sin n\theta \cos q\theta \\
& \cdot \left\{ \sin \lambda_m x \cos \lambda_p (x-a) \cdot \frac{K'_q(\lambda_p r)}{K_q(\lambda_p r)} - \cos \lambda_m x \sin \lambda_p (x-a) \cdot \frac{K'_n(\lambda_m r)}{K_n(\lambda_m b)} \right\}
\end{aligned} \tag{4.18c}$$

$$\begin{aligned}
F_x(r, \theta, x) = & -\frac{a}{r} \sum_{m=0}^{\infty} \sum_{n=1}^{\infty} \sum_{p=0}^{\infty} \sum_{q=1}^{\infty} \frac{16J_0 B_0}{\pi^2} \frac{K_n(\lambda_m r)}{K_n(\lambda_m b)} \frac{K_q(\lambda_p r)}{K_q(\lambda_p b)} \sin \lambda_m \frac{a}{2} \sin \lambda_p \frac{a}{2} \\
& \cdot (\cos n\theta_1 - \cos n\theta_2)(\sin q\theta_2 - \sin q\theta_1) \cos \lambda_m x \cos \lambda_p (x-a) \\
& \cdot \left\{ \frac{K'_q(\lambda_p r)}{K_q(\lambda_p b)} \frac{\cos n\theta \cos q\theta}{\lambda_m q} + \frac{K'_n(\lambda_m r)}{K_n(\lambda_m b)} \frac{\sin n\theta \sin q\theta}{\lambda_q n} \right\}
\end{aligned} \tag{4.18d}$$

These expressions show that the radial and axial components, $F_r(r, \theta, x)$ and $F_x(r, \theta, x)$, are of the order $\frac{a}{b}$ compared to the azimuthal component, $F_\theta(r, \theta, x)$. This

implies that if the ratio $\frac{a}{b}$ is much less than 1, then the radial and axial force components can be neglected in front of the azimuthal component of the Lorentz force which then dominates. It is then useful to average each force component in the axial direction.

$$F_j(r, \theta) = \frac{1}{2a} \int_{-a}^a F_j(r, \theta, x) dx \tag{4.19}$$

where the subscript j refers to r , θ , and x , respectively.

After mathematical manipulations, the axial averages of the various components of the Lorentz force are given by

$$F_r(r, \theta) = -\frac{a}{r} \sum_{m=0}^{\infty} \sum_{n=1}^{\infty} \sum_{q=1}^{\infty} \frac{8J_0 B_0}{\lambda_m \pi^2} \frac{K_n(\lambda_m r)}{K_n(\lambda_m b)} \frac{K_q(\lambda_m r)}{K_q(\lambda_m b)} \cdot (\cos n\theta_1 - \cos n\theta_2)(\sin q\theta_2 - \sin q\theta_1) \left\{ \frac{\cos n\theta \cos q\theta}{q} - \frac{\sin n\theta \sin q\theta}{n} \right\} \quad (4.20a)$$

$$F_\theta(r, \theta) = \sum_{m=0}^{\infty} \sum_{n=1}^{\infty} \sum_{q=1}^{\infty} \frac{4J_0 B_0}{nq\pi^2} \cdot (\cos n\theta_1 - \cos n\theta_2)(\sin q\theta_2 - \sin q\theta_1) \cdot \frac{K_n(\lambda_m r)K'_q(\lambda_m r) - K_q(\lambda_m r)K'_n(\lambda_m r)}{K_n(\lambda_m b)K_q(\lambda_m b)} \sin n\theta \cos q\theta \quad (4.20b)$$

$$F_x(r, \theta) = 0 \quad (4.20c)$$

Using the Bessel functions identity $K'_\nu(z) = \frac{\nu}{z}K_\nu(z) - K_{\nu+1}(z)$, it is possible to eliminate

the derivative of the modified Bessel functions in the expression of $F_\theta(r, \theta)$, so that

$$F_\theta(r, \theta) = \sum_{m=0}^{\infty} \sum_{n=1}^{\infty} \sum_{q=1}^{\infty} \frac{4J_0 B_0}{nq\pi^2} (\cos n\theta_1 - \cos n\theta_2)(\sin q\theta_2 - \sin q\theta_1) \cdot \frac{\{K_{n+1}(\lambda_m r)K_q(\lambda_m r) - K_n(\lambda_m r)K_{q+1}(\lambda_m r)\}}{K_n(\lambda_m b)K_q(\lambda_m b)} \sin n\theta \cos q\theta \quad (4.21)$$

This expression is still rather complicated, and needs further simplifications for any practical applications. The next section focuses on seeking a simpler expression.

4.4 Approximate Solution

Further simplifications are sought by considering limit cases. Particularly, two cases are considered, depending on the value of the aspect ratio $\frac{a}{b}$, i.e., the ratio of electrodes/magnets width to the cylindrical radius. In the first case, it is considered that the aspect ratio is extremely small and, in the limit, tends to zero; in the other case, it is considered that the aspect ratio is extremely large and, in the limit, tends to infinity.

Case I: $\frac{a}{b} \rightarrow 0$

In this case, the derivative of the potential function in the azimuthal direction vanishes. The degenerated potential function $U(r, \theta, x)$ is then denoted $H(r, x)$ such that

$$\lim_{a/b \rightarrow 0} \frac{U(r, \theta, x)}{U_0} = H(r, x) \quad (4.22)$$

This implies that the Laplace equation reduces to:

$r - x$ plane:

$$\frac{1}{r} \frac{\partial}{\partial r} \left(r \frac{\partial H}{\partial r} \right) + \frac{\partial^2 H}{\partial x^2} = 0 \quad (4.23a)$$

$$\text{with} \quad H(-a, y) = H(a, y) = 0, \quad y = r - b \geq 0, \quad (4.23b)$$

$$H(x, 0) = 1, \quad -\frac{a}{2} < x < \frac{a}{2}, \quad (4.23c)$$

$$\text{and} \quad H(x, 0) = 0, \quad -a < x < -\frac{a}{2} \text{ or } \frac{a}{2} < x < a \quad (4.23d)$$

Following the procedure previously outlined for solving Equation (4.3), it is found that the solution of Equation (4.23) is

$$H(r, x) = \sum_{m=0}^{\infty} \frac{2}{a\lambda_m} \frac{K_0(\lambda_m r)}{K_0(\lambda_m b)} \sin(\lambda_m a) \cos(\lambda_m x), \quad \lambda_m = \left(n + \frac{1}{2}\right) \frac{\pi}{a} \quad (4.24)$$

Case II: $\frac{a}{b} \rightarrow \infty$

In this case, the derivative of the potential function in the r - and θ -directions are much greater than the derivative in the x -direction. The degenerated potential function $U(r, \theta, x)$, denoted $K(r, \theta)$, becomes

$$\lim_{a/b \rightarrow \infty} \frac{U(r, \theta, x)}{U_0} = K(r, \theta) \quad (4.25)$$

It follows that the Laplace equation gets the simplified form

$$\frac{1}{r} \frac{\partial}{\partial r} \left(r \frac{\partial K}{\partial r} \right) + \frac{1}{r^2} \frac{\partial^2 K}{\partial \theta^2} = 0 \quad (4.26a)$$

with

$$K(b, \theta) = f(\theta) = \begin{cases} 1, & \theta_1 < \theta \leq \theta_2 \\ -1, & 2\pi - \theta_2 < \theta \leq 2\pi - \theta_1, r \geq b \\ 0, & \text{other } \theta \end{cases} \quad (4.26b)$$

This is the Laplace equation subjected to Dirichlet boundary conditions in cylindrical geometry. Appendix A gives the solution of such equation as

$$K(r, \theta) = \frac{1}{2\pi} \int_0^{2\pi} \frac{r^2 - b^2}{r^2 - 2rb \cos(\theta + \varphi) + b^2} f(\varphi) d\varphi, \quad r \geq b \quad (4.27)$$

For the particular case where $f(\varphi)$ is given by

$$f(\varphi) = \begin{cases} 1, & \theta_1 < \varphi \leq \theta_2 \\ -1, & 2\pi - \theta_2 < \varphi \leq 2\pi - \theta_1 \\ 0, & \text{otherwise} \end{cases} \quad (4.28)$$

(through the boundary condition), the above integral (4.27) reduces to

$$K(r, \theta) = S^+(r, \theta) - S^-(r, \theta), \quad r > b \quad (4.29)$$

with

$$S^-(r, \theta) = S^+(r, 2\pi - \theta) \quad (4.30a)$$

$$S^+(r, \theta) = \begin{cases} 1 + \frac{1}{\pi} \left(\tan^{-1} \left(\frac{r+b}{r-b} \tan \frac{\theta - \theta_1}{2} \right) + \tan^{-1} \left(\frac{r+b}{r-b} \tan \frac{\theta_2 - \theta}{2} \right) \right), & \theta_1 + \pi < \theta < \theta_2 + \pi \\ \frac{1}{\pi} \left(\tan^{-1} \left(\frac{r+b}{r-b} \tan \frac{\theta - \theta_1}{2} \right) + \tan^{-1} \left(\frac{r+b}{r-b} \tan \frac{\theta_2 - \theta}{2} \right) \right), & \text{otherwise} \end{cases} \quad (4.30b)$$

The details of the derivation of such expression can be found in Appendix B.

In realistic applications, the aspect ratio $\frac{a}{b}$ is not always very small or always very large, and therefore the above approximations may have to be corrected. Since $-1 \leq H(r, x) \leq 1$ and $-1 \leq K(r, \theta) \leq 1$, a way to generalize the above results is to consider a three-dimensional dependency such that

$$\frac{U_{mix}(r, \theta, x)}{U_0} = H(r, x)K(r, \theta) \quad (4.31)$$

where the r - and θ -dependencies are still in the form of separated variables. In a certain sense, this is a way to mix the solutions of the two limit cases, and for that reason, the particular solutions in the form (4.31) are referred to as “mixed” solutions hereafter. The subscript *mix* refers to the latter and the corresponding model is referred to as the MIX model.

Similarly, the magnetic problem can be solved by a similar MIX model and the magnetic potential is then assumed to be of the form

$$\frac{\Phi_{mix}(r, \theta, x)}{\Phi_0} = H(r, x - a)K^*(r, \theta) \quad (4.32)$$

where

$$K(r, \theta) = S^+(r, \theta) + S^-(r, \theta), \quad r > b \quad (4.33)$$

The Lorentz force derived from the MIX model takes the form

$$\begin{aligned}\vec{F}_{mix}(r, \theta, x) &= \sigma \nabla U_{mix} \times \nabla \Phi_{mix} \\ &= \sigma U_0 \Phi_0 \nabla (H(r, x) K(r, \theta)) \times \nabla (H(r, x - a) K^*(r, \theta))\end{aligned}\quad (4.34)$$

with its three components being given by the expressions

$$\begin{aligned}f_r(r, \theta, x) &= \frac{1}{r} \sum_{m=0}^{\infty} \sum_{n=0}^{\infty} 4J_0 B_0 \frac{K_0(\lambda_m r) K_0(\lambda_n r)}{K_0(\lambda_m b) K_0(\lambda_n b)} \sin \lambda_m a \sin \lambda_n a \\ &\cdot \left[\left(\frac{\cos \lambda_m x \sin \lambda_n (x - a)}{\lambda_m} - \frac{\sin \lambda_n x \cos \lambda_m (x - a)}{\lambda_n} \right) \left(S^+ \frac{\partial S^+}{\partial \theta} - S^- \frac{\partial S^-}{\partial \theta} \right) \right. \\ &\left. + \left(\frac{\sin \lambda_m x \cos \lambda_n (x - a)}{\lambda_n} + \frac{\cos \lambda_n x \sin \lambda_m (x - a)}{\lambda_m} \right) \left(S^+ \frac{\partial S^-}{\partial \theta} - S^- \frac{\partial S^+}{\partial \theta} \right) \right]\end{aligned}\quad (4.35a)$$

$$\begin{aligned}f_\theta(r, \theta, x) &= \sum_{m=0}^{\infty} \sum_{n=0}^{\infty} 4J_0 B_0 \sin \lambda_m a \sin \lambda_n a \cdot ((S^+)^2 - (S^-)^2) \\ &\cdot \left[\frac{K'_0(\lambda_m r) K_0(\lambda_n r)}{K_0(\lambda_m b) K_0(\lambda_n b)} \sin \lambda_m x \cos \lambda_n (x - a) - \frac{K_0(\lambda_m r) K'_0(\lambda_n r)}{K_0(\lambda_m b) K_0(\lambda_n b)} \cos \lambda_m x \sin \lambda_n (x - a) \right] \\ &+ \sum_{m=0}^{\infty} \sum_{n=0}^{\infty} 4J_0 B_0 \frac{K_0(\lambda_m r) K_0(\lambda_n r)}{K_0(\lambda_m b) K_0(\lambda_n b)} \sin \lambda_m a \sin \lambda_n a \\ &\cdot \left[\left(\frac{\cos \lambda_m x \cos \lambda_n (x - a)}{\lambda_m} - \frac{\sin \lambda_n x \cos \lambda_m (x - a)}{\lambda_n} \right) \left(S^+ \frac{\partial S^+}{\partial r} - S^- \frac{\partial S^-}{\partial r} \right) \right. \\ &\left. + \left(\frac{\sin \lambda_m x \cos \lambda_n (x - a)}{\lambda_n} + \frac{\cos \lambda_n x \sin \lambda_m (x - a)}{\lambda_m} \right) \left(S^+ \frac{\partial S^-}{\partial r} - S^- \frac{\partial S^+}{\partial r} \right) \right]\end{aligned}\quad (4.35b)$$

$$\begin{aligned}f_x(r, \theta, x) &= \frac{1}{r} \sum_{m=0}^{\infty} \sum_{n=0}^{\infty} \frac{2J_0 B_0}{\lambda_m \lambda_n} \frac{K_0(\lambda_m r) K_0(\lambda_n r)}{K_0(\lambda_m b) K_0(\lambda_n b)} \sin \lambda_m a \sin \lambda_n a \\ &\cdot \cos \lambda_m x \cos \lambda_n (x - a) \left(\frac{\partial S^+}{\partial r} \frac{\partial S^-}{\partial \theta} - \frac{\partial S^+}{\partial \theta} \frac{\partial S^-}{\partial r} \right) \\ &+ \frac{1}{r} \sum_{m=0}^{\infty} \sum_{n=0}^{\infty} \left(\frac{4J_0 B_0 \sin \lambda_m a \sin \lambda_n a}{K_0(\lambda_m b) K_0(\lambda_n b)} \right) \cos \lambda_m x \cos \lambda_n (x - a) \\ &\cdot \left\{ \left[\frac{K'_0(\lambda_m r) K_0(\lambda_n r)}{\lambda_n} - \frac{K_0(\lambda_m r) K'_0(\lambda_n r)}{\lambda_m} \right] \left(S^+ \frac{\partial S^+}{\partial \theta} - S^- \frac{\partial S^-}{\partial \theta} \right) \right. \\ &\left. + \left[\frac{K'_0(\lambda_m r) K_0(\lambda_n r)}{\lambda_n} + \frac{K_0(\lambda_m r) K'_0(\lambda_n r)}{\lambda_m} \right] \left(S^+ \frac{\partial S^-}{\partial \theta} - S^- \frac{\partial S^+}{\partial \theta} \right) \right\}\end{aligned}\quad (4.35c)$$

The averages in the axial direction of the components of the Lorentz force are as follows in cylindrical coordinates.

$$f_r(r, \theta) = \frac{1}{r} \sum_{m=0}^{\infty} \sum_{n=0}^{\infty} (-1)^n J_0 B_0 \frac{K_0^2(\lambda_n r)}{\lambda_n K_0^2(\lambda_n b)} \frac{\partial}{\partial \theta} \left((S^+)^2 - (S^-)^2 \right) \quad (4.36a)$$

$$f_\theta(r, \theta) = \sum_{n=0}^{\infty} 2(-1)^n J_0 B_0 \frac{K_0(\lambda_n r) K_1(\lambda_n r)}{K_0^2(\lambda_n b)} \left((S^+)^2 - (S^-)^2 \right) - \sum_{n=0}^{\infty} (-1)^n J_0 B_0 \frac{K_0^2(\lambda_n r)}{\lambda_n K_0^2(\lambda_n b)} \frac{\partial}{\partial r} \left((S^+)^2 - (S^-)^2 \right) \quad (4.36b)$$

$$f_x(r, \theta) = 0 \quad (4.36c)$$

4.5 Simplified Approximate Solution

In the case of the aspect ratio $\frac{a}{b} \leq 1$, the minimum value for the variable in the modified zero order modified Bessel function is $z = \frac{\pi b}{2a} > 1$. When $z \rightarrow \infty$, corresponding to the limit case where the ratio a/b tends to zero, the modified Bessel functions can be approximated by $K_n(z) \sim \sqrt{\frac{2}{\pi z}} e^{-z}$. In this case, the square of the zero order Bessel function takes the simplified expression

$$K_0^2(z) = c_{00}(z) K_0^2(1) \frac{e^{-2z}}{z}, \quad z > 1 \quad (4.37a)$$

Similarly, the product of the zero order with the first order modified Bessel functions simplifies to

$$K_0(z) K_1(z) = c_{01}(z) K_0(1) K_1(1) \frac{e^{-2z}}{z}, \quad z > 1 \quad (4.37b)$$

In Equations (4.37a) and (4.37b), the values taken by the coefficient functions $c_{00}(z)$ and $c_{01}(z)$ at various z points ($z > 1$) are given in Table 4.1.

Table 4.1 Values of the coefficient functions $c_{00}(z)$ and $c_{01}(z)$ at various z values.

z	1.0	1.5	2.0	2.5	3.0	3.5	4.0	4.5	5.0	6.0
$c_{00}(z)$	1.3098	1.3772	1.4165	1.4423	1.4606	1.4743	1.4850	1.4935	1.5005	1.5112
$c_{01}(z)$	1.8725	1.7868	1.7395	1.7093	1.6884	0.6730	1.6611	1.6518	1.6442	1.6326
z	7.0	8.0	9.0	10.0	15.0	20.0	25.0	30.0	40.0	50.0
$c_{00}(z)$	1.5191	1.5251	1.5299	1.5338	1.5456	1.5517	1.5555	1.5580	1.5611	1.5630
$c_{01}(z)$	1.6242	1.6178	1.6127	1.6087	1.5964	1.5901	1.5863	1.5837	1.5805	1.5786

Substituting these simplifications into Equation (4.36), the Lorentz force components take the following forms.

$$f_r(r, \theta) = \frac{2ab}{\pi r^2} J_0 B_0 \frac{\partial}{\partial \theta} \left((S^+)^2 - (S^-)^2 \right) \cdot \left\{ c_{00} \left(\frac{3\pi b}{2a} \right) \arctan \left(e^{\frac{\pi}{a}(r-b)} \right) + \left[c_{00} \left(\frac{\pi b}{2a} \right) - c_{00} \left(\frac{3\pi b}{2a} \right) \right] e^{-\frac{\pi}{a}(r-b)} \right\} \quad (4.38a)$$

$$f_\theta(r, \theta) = 2J_0 B_0 \left[c_{01} \left(\frac{\pi b}{2a} \right) e^{\frac{\pi}{a}(r-b)} - c_{01} \left(\frac{3\pi b}{2a} \right) \frac{e^{-\frac{3\pi}{a}(r-b)}}{1 + e^{-\frac{2\pi}{a}(r-b)}} \right] \left((S^+)^2 - (S^-)^2 \right) - \frac{2ab}{\pi r} J_0 B_0 \frac{\partial}{\partial r} \left((S^+)^2 - (S^-)^2 \right) \cdot \left\{ c_{00} \left(\frac{3\pi b}{2a} \right) \arctan \left(e^{\frac{\pi}{a}(r-b)} \right) + \left[c_{00} \left(\frac{\pi b}{2a} \right) - c_{00} \left(\frac{3\pi b}{2a} \right) \right] e^{-\frac{\pi}{a}(r-b)} \right\} \quad (4.38b)$$

A further approximation leads to

$$f_r(r, \theta) = \frac{2ab}{\pi r^2} c_{00} \left(\frac{\pi b}{2a} \right) J_0 B_0 \arctan \left(e^{\frac{\pi}{a}(r-b)} \right) \frac{\partial}{\partial \theta} \left((S^+)^2 - (S^-)^2 \right) \quad (4.39a)$$

$$\begin{aligned}
f_{\theta}(r, \theta) = & \frac{2b}{r} J_0 B_0 c_{01} \left(\frac{\pi b}{2a} \right) \frac{e^{-\frac{\pi}{a}(r-b)}}{1 + e^{-\frac{2\pi}{a}(r-b)}} \left((S^+)^2 - (S^-)^2 \right) \\
& - \frac{2ab}{\pi r} c_{00} \left(\frac{\pi b}{2a} \right) J_0 B_0 \arctan \left(e^{-\frac{\pi}{a}(r-b)} \right) \frac{\partial}{\partial r} \left((S^+)^2 - (S^-)^2 \right)
\end{aligned} \tag{4.39b}$$

In Equation (4.36) or even in its simplified forms, Equations (4.38) and (4.39), the r -component of the Lorentz force is nonzero, although it decreases extremely fast with distance from the cylinder (much faster than the θ -component).

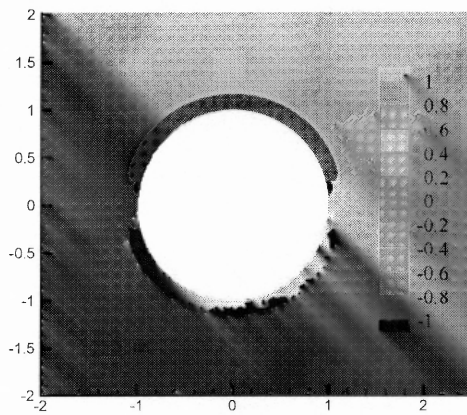
The effect of discontinuities in the boundary conditions on the cylinder surface is reflected in the factor $\frac{\partial}{\partial r} \left((S^+)^2 - (S^-)^2 \right)$. It is also found that the aspect ratio $\frac{a}{b}$ plays an important role in the expression of Lorentz force, particularly in both its decreasing rate with distance from the cylinder and its maximum value on the wall.

Figures 4.2 - 4.6 present the comparison of the Lorentz force from the numerical simulation, the MIX model and the DM model used by Weier *et al.* (1998). All calculations were set with the same actuation area defined by the interval $[\theta = 5^\circ, \theta = 175^\circ]$ on the upper semi-cylinder surface and the symmetric interval on the lower semi-cylinder surface. The aspect ratio of the width a of the electrodes and magnets to the cylindrical radius b was changed from 0.1 to 0.5. It is clear from these figures that the main difference between the various methods and models lies in the distribution of the Lorentz force in the θ -direction. The DM model has a clear azimuthal discontinuity in the Lorentz force everywhere in the fluid domain where it is non-zero, while this discontinuity is absent in both the numerical simulation results and the MIX model.

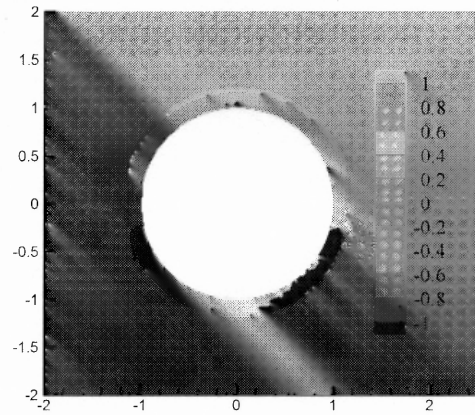
When the aspect ratio $\frac{a}{b}$ decreases to zero, the function $(S^+)^2 - (S^-)^2$ tends to either 1 or -1 (depending on the particular arrangement of electrodes and magnets) so that the terms with $\frac{\partial}{\partial r}((S^+)^2 - (S^-)^2)$ and $\frac{\partial}{\partial \theta}((S^+)^2 - (S^-)^2)$ vanish. The coefficients become $c_{01}\left(\frac{\pi b}{2a}\right) = c_{01}\left(\frac{3\pi b}{2a}\right) = 1$ and only the first term in the θ -component of the Lorentz force remains nonzero. Setting $y = r - b$, that component becomes

$$\begin{aligned}
 f_{\theta}(r, \theta) \Big|_{\frac{a}{b} \rightarrow 0} &= 2J_0 B_0 \left[c_{01} \left(\frac{\pi b}{2a} \right) e^{-\frac{\pi}{a}(r-b)} - c_{01} \left(\frac{3\pi b}{2a} \right) \frac{e^{-\frac{3\pi}{a}(r-b)}}{1 + e^{-\frac{2\pi}{a}(r-b)}} \right] \left((S^+)^2 - (S^-)^2 \right) \\
 &= 2J_0 B_0 c_{01} \left(\frac{\pi b}{2a} \right) \left[e^{-\frac{\pi}{a}(r-b)} - \frac{e^{-\frac{3\pi}{a}(r-b)}}{1 + e^{-\frac{2\pi}{a}(r-b)}} \right]_{y=r-b} \\
 &= 2J_0 B_0 \frac{e^{-\frac{\pi y}{a}}}{1 + e^{-\frac{2\pi y}{a}}}
 \end{aligned} \tag{4.41}$$

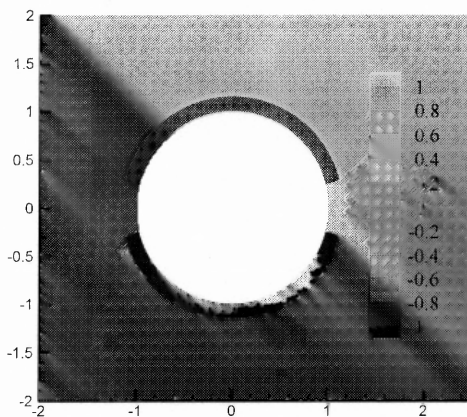
This result coincides with the expression of the Lorentz force in the case of the flat plate. It makes sense to recover the case of a plate as $a/b \rightarrow 0$.



(a)



(b)



(c)

Calculation parameters

Ratio:

$$a/b = 0.1$$

Actuation area:

5 - 175°, upper semi-cylindrical surface

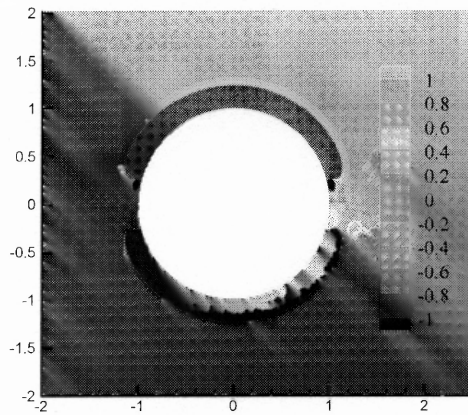
185 - 355°, lower semi-cylindrical surface

(a) Numerical result

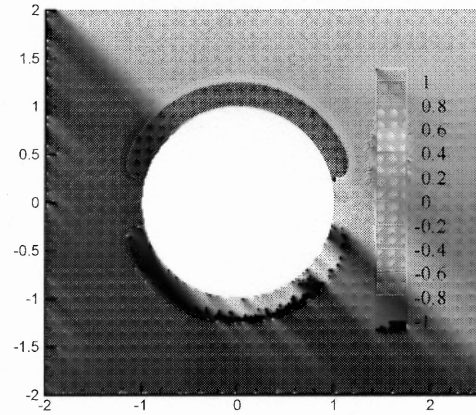
(b) MIX model

(c) DM model

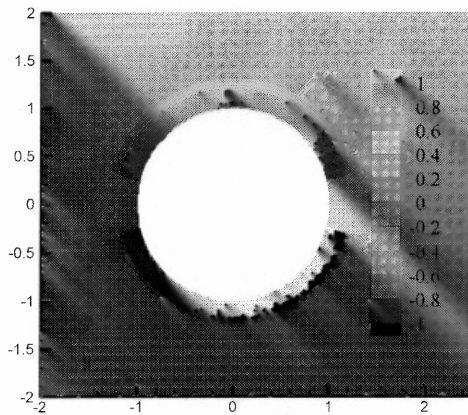
Figure 4.2 Comparison of the Lorentz force computed from the DM model, the MIX model and numerical simulations for the aspect ratio $a/b = 0.1$.



(a)



(b)



(c)

Calculation parameters

Ratio:

$$a/b = 0.2$$

Actuation area:

5 - 175°, upper semi-cylindrical surface

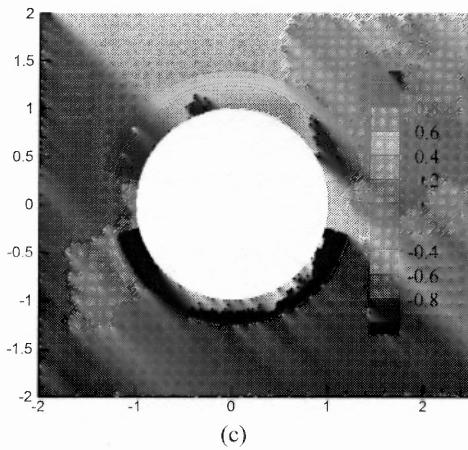
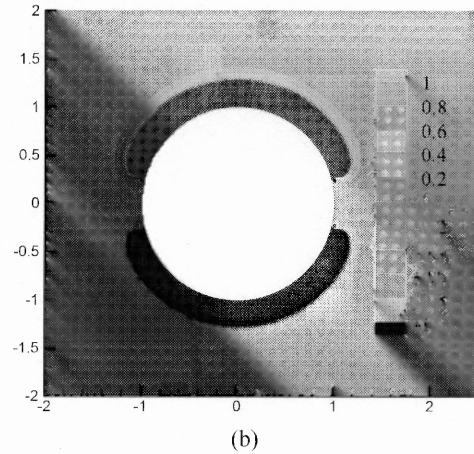
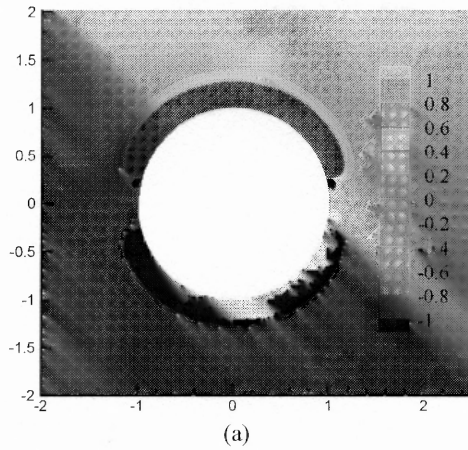
185 - 355°, lower semi-cylindrical surface

(a) Numerical result

(b) MIM model

(c) DM model

Figure 4.3 Comparison of the Lorentz force computed from the DM model, the MIM model and numerical simulations for the aspect ratio $a/b = 0.2$.



Calculation parameters

Ratio:

$$a/b = 0.3$$

Actuation area:

5 - 175°, upper semi-cylindrical surface

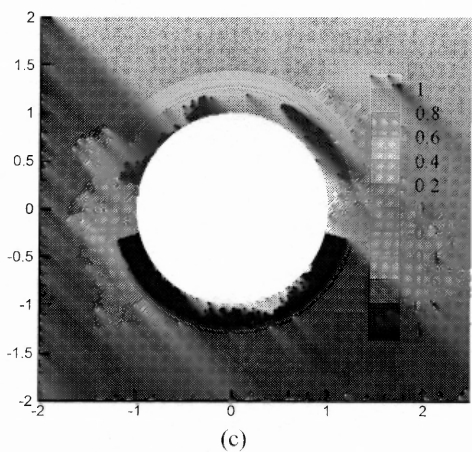
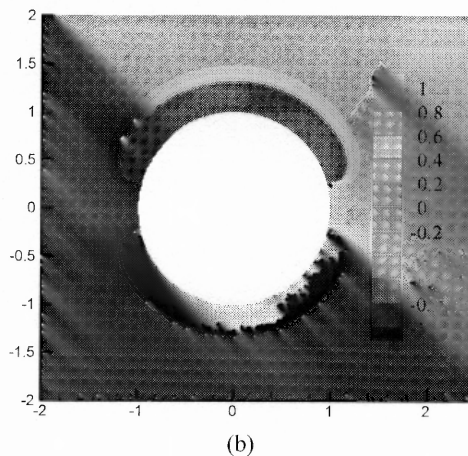
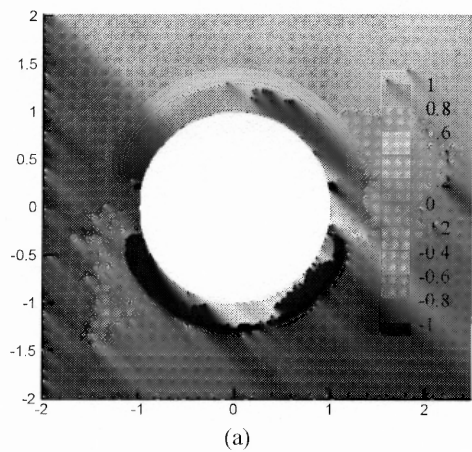
185 - 355°, lower semi-cylindrical surface

(a) Numerical result

(b) MIX model

(c) DM model

Figure 4.4 Comparison of the Lorentz force computed from the DM model, the MIX model and the numerical simulations for the aspect ratio $a/b = 0.3$.



Calculation parameters

Ratio:

$$a/b = 0.4$$

Actuation area:

5 - 175°, upper semi-cylindrical surface

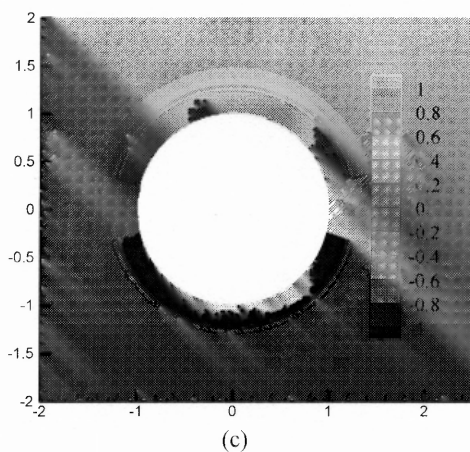
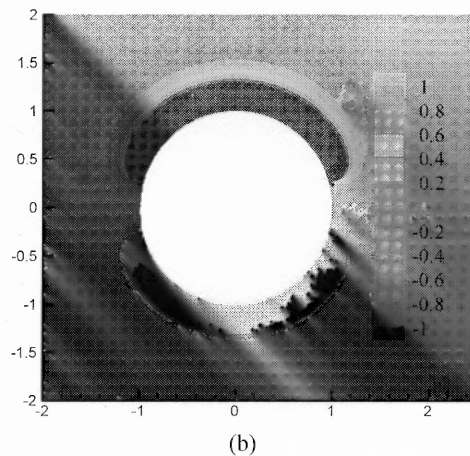
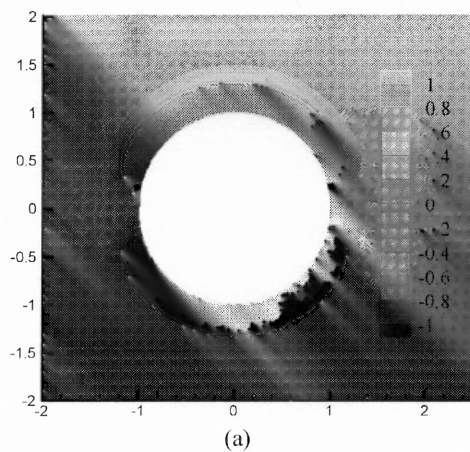
185 - 355°, lower semi-cylindrical surface

(a) Numerical result

(b) MIM model

(c) DM model

Figure 4.5 Comparison of the Lorentz force computed from the DM model, the MIM model and the numerical simulations for the aspect ratio $a/b = 0.4$.



Calculation parameters

Ratio:

$$a/b = 0.5$$

Actuation area:

5 - 175°, upper semi-cylindrical surface

185 - 355°, lower semi-cylindrical surface

(a) Numerical result

(b) MIM model

(c) DM model

Figure 4.6 Comparison of the Lorentz force computed from the DM model, the MIM model and the numerical simulations for the aspect ratio $a/b = 0.5$.

CHAPTER 5

CONTROL OF VORTEX SHEDDING FROM CYLINDER BY ELECTROMAGNETIC FIELDS

5.1 Introduction

In this chapter, the flow of a conducting fluid is considered. For example, the electric conductivity of liquid mercury is $\sigma \approx 10^6$ mhos/m and that of seawater is $\sigma \approx 4$ mhos/m. Due to many potential applications such as ships and sea vessels, seawater is often the selected fluid in many studies. Seawater is only slightly conducting since its electric conductivity, as recalled above, is low. This dissertation focuses on a low conducting fluid such as seawater. When an electromagnetic field is applied to a conducting fluid, the cross product of the current density \vec{J} and the magnetic flux density \vec{B} leads to the Lorentz force

$$\vec{F} = \vec{J} \times \vec{B} \quad (5.1)$$

where \vec{J} is the sum of the electric density of the applied electric field and induced electric field, i.e.

$$\vec{J} = \sigma \vec{E} + \sigma \vec{u} \times \vec{B} \quad (5.2)$$

Therefore, the Lorentz force takes the expression

$$\vec{F} = \sigma(\vec{E} \times \vec{B}) + \sigma(\vec{u} \times \vec{B}) \times \vec{B} \quad (5.3)$$

In three-dimensional coordinates, the components of the Lorentz force are given by

$$F_x = \sigma(E_y B_z - E_z B_y) + \sigma[u_y B_x B_y + u_z B_x B_z - u_x (B_z^2 + B_y^2)] \quad (5.4a)$$

$$F_y = \sigma(E_y B_z - E_z B_y) + \sigma[u_x B_x B_y + u_z B_y B_z - u_y (B_x^2 + B_z^2)] \quad (5.4b)$$

$$F_z = \sigma(E_y B_z - E_z B_y) + \sigma[u_x B_x B_z + u_y B_y B_z - u_z (B_x^2 + B_y^2)] \quad (5.4c)$$

For a slightly conducting fluid, the induced electric field is small, and the second term in Equations (5.2) and (5.3) is negligible in front of the first term. The Lorentz force originates in the cross-product of the external electric and magnetic fields, and a magnetic field alone is not enough. In addition, the force is independent of the flow velocity, which makes the electro-magnetism problem independent of the fluid mechanics one and, therefore, greatly simplifies the analysis.

In Appendix C, the electrodes and magnets are arranged continuously in the azimuthal direction, forming circular stripes wrapping the entire cylinder. The Lorentz force generated from such an arrangement generates an azimuthal, vortex flow around the cylinder. For the purpose of controlling the flow past a cylinder, the component of the Lorentz force in the flow direction is kept nonzero in order to exert a body force on the fluid that compensates the loss of momentum associated with flow separation. In the flat plate case analyzed in Chapter 3, the components of the electric and magnetic fields are such that $\vec{E}_z = \vec{B}_z = 0$, and \vec{E}_x , \vec{E}_y , \vec{B}_x , and \vec{B}_y are nonzero. It follows (from Equation (5.4)) that the only nonzero component of the Lorentz force generated is the z -component, in the flow direction. The next section focuses on the control of the fluid flow past a circular cylinder at the Reynolds numbers $Re = 100$ and 200 .

5.2 Open Control

Open control is the simplest mode of active control since it only requires actuators (see Figure 5.1). Because it does not need to sense the flow in time, it is easy to apply. However, its drawback is obvious: since it is preset, it does not adapt to temporal changes in the flow conditions.

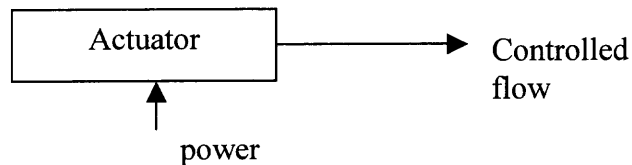


Figure 5.1 Schematics of open loop control.

In previous studies addressing the electro-magnetic control of vortex shedding, the actuation area of the Lorentz force is selected arbitrarily, that is over most of the cylinder surface (Weier *et al.*, 1998) or over a preset angular area (Kim and Lee, 2001). Furthermore, the Lorentz force is defined by the interaction parameter taking the respective values $N = 1$, $N = 2$, $N = 3$, $N = 5$, etc. The numerical simulations reported in this dissertation are based on the two-dimensional Navier-Stokes solver recalled earlier (Aubry and Tang, 1998). As the flow field is impulsively started, periodic vortex shedding sets in only after some time. In order to guarantee that the flow is fully developed, the flow control is introduced at $t = 560$ seconds.

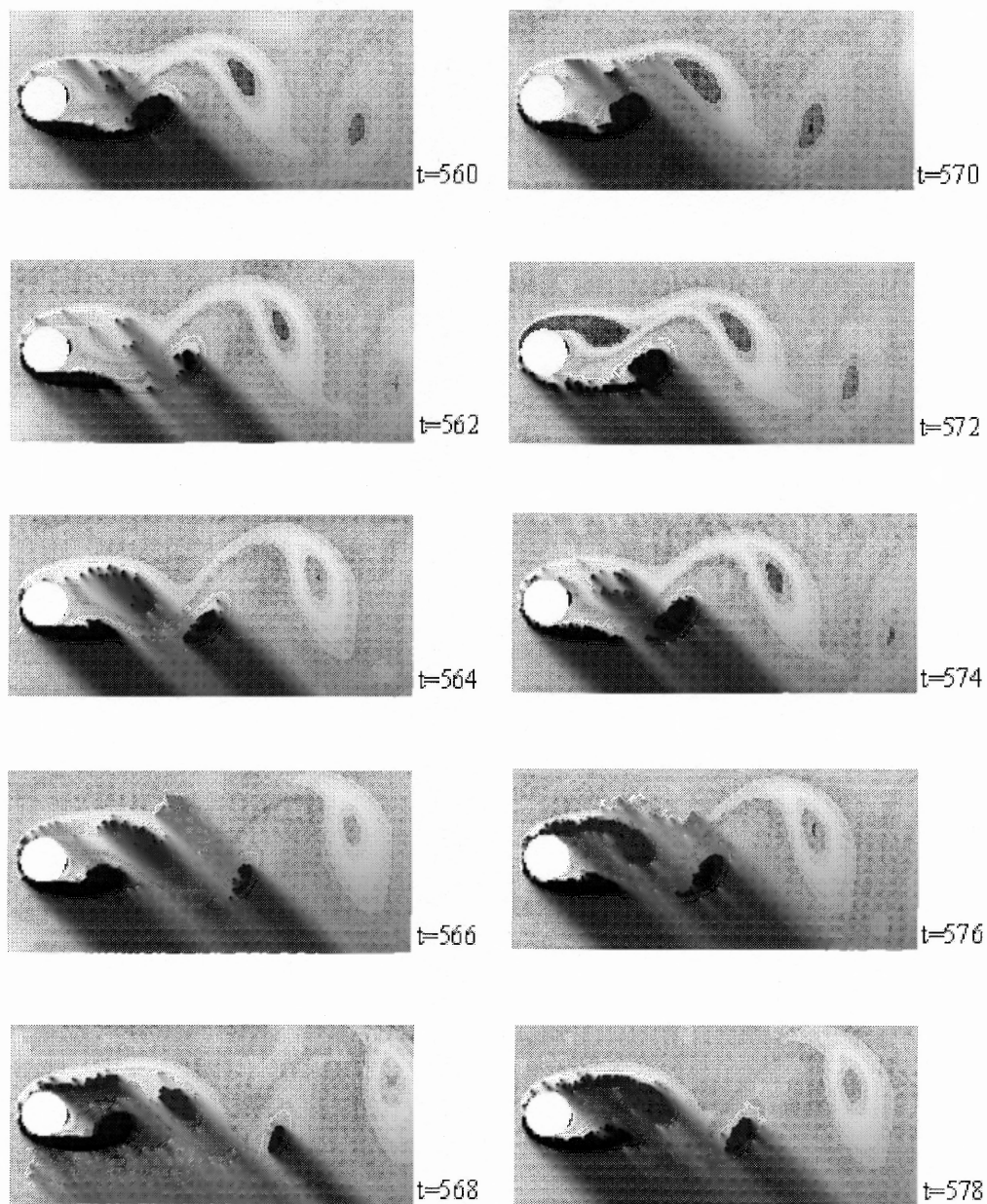


Figure 5.2 Visualization of the flow by vorticity contours for the flow without control at the Reynolds number $Re = 100$, showing vortex shedding.

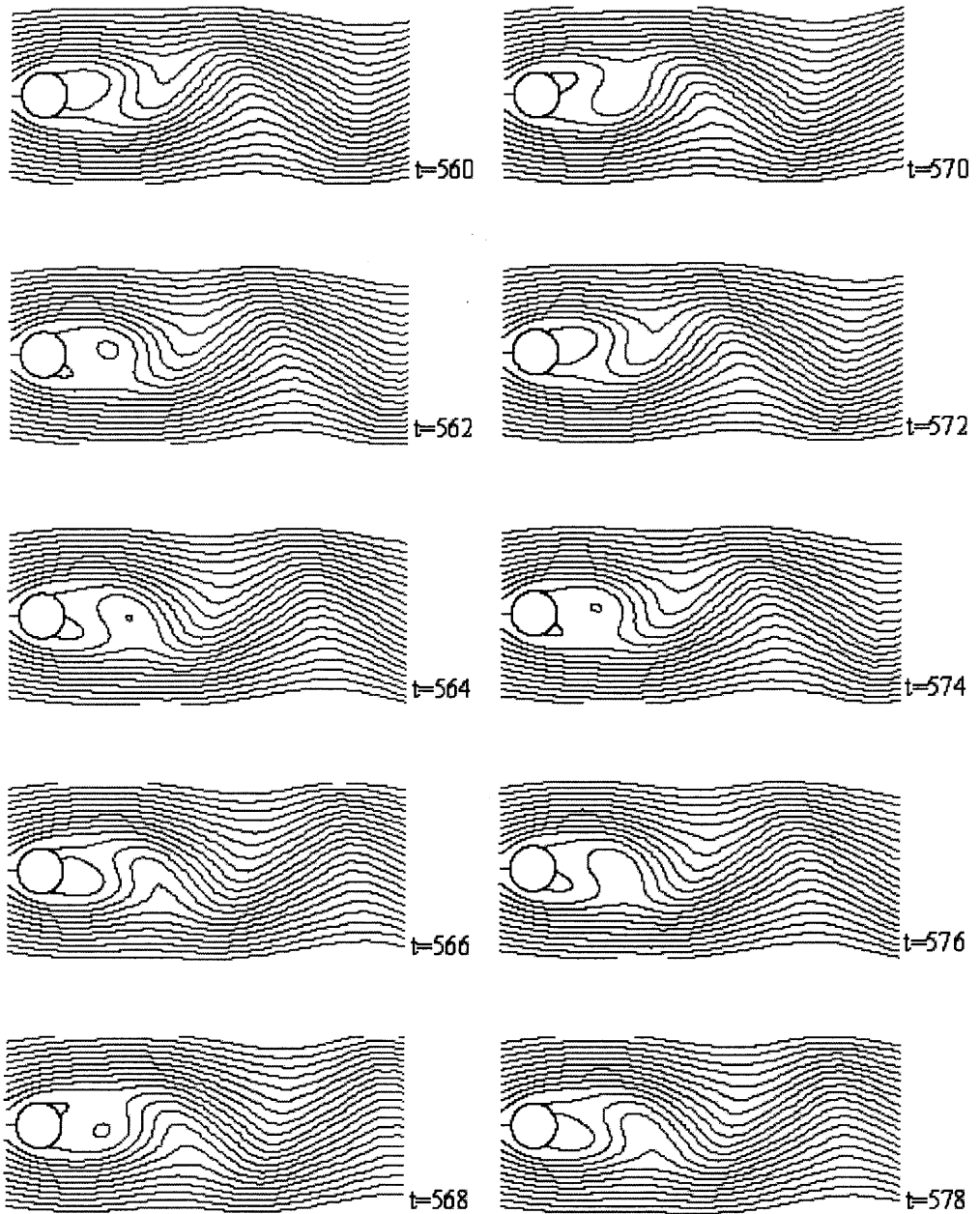


Figure 5.3 Visualization of the flow by streamlines for the flow without control at the Reynolds number $Re = 100$, showing vortex shedding.

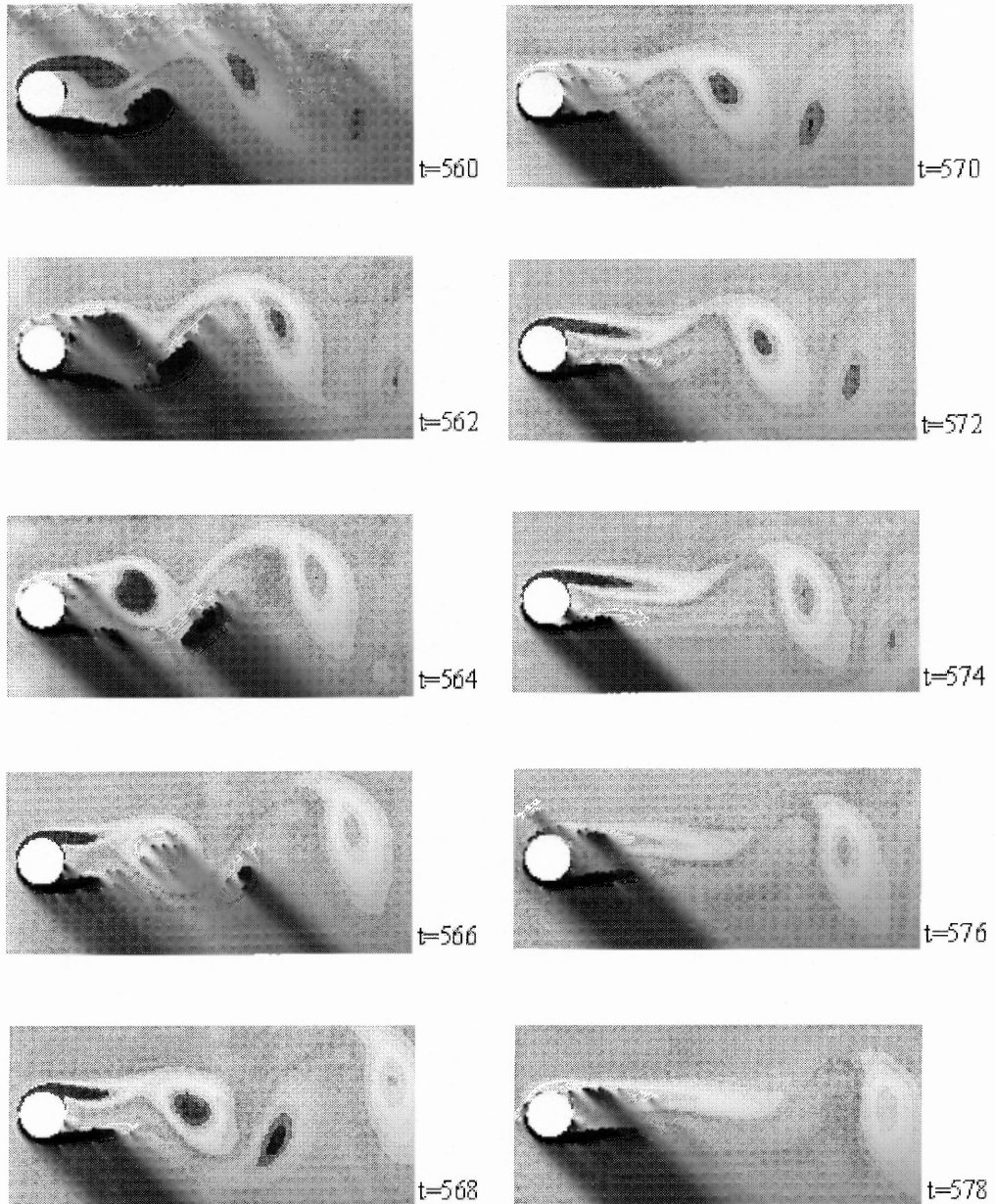


Figure 5.4 Visualization of the flow by vorticity contours for the flow after open loop control at the Reynolds number $Re = 100$. The interaction parameter value is $N = 2$. This clearly shows vortex shedding is fully suppressed by the control.

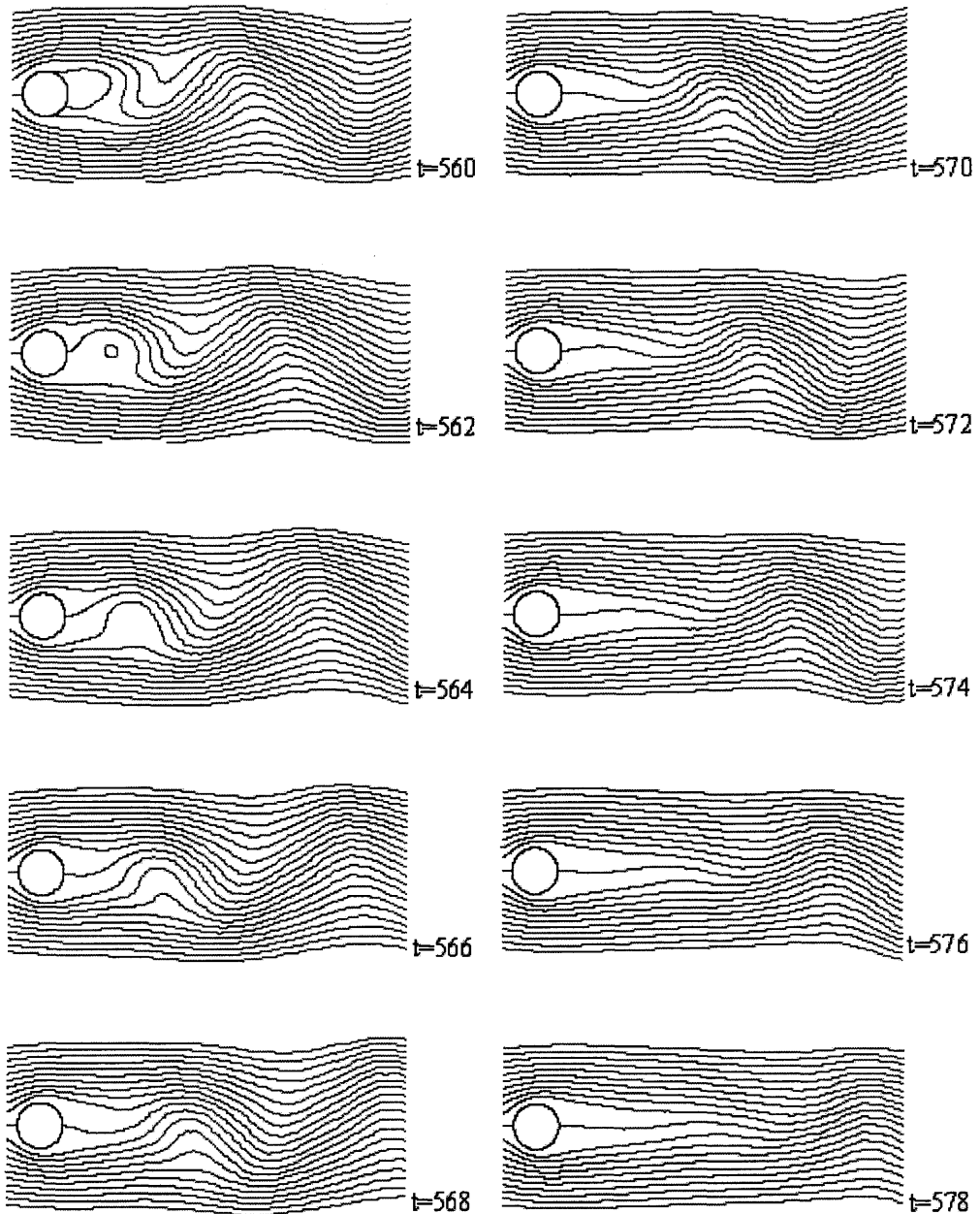


Figure 5.5 Visualization of the flow by streamlines for the flow with open loop control at the Reynolds number $Re = 100$. The interaction parameter is $N = 2$. The control scheme suppresses vortex shedding, the streamline originating at the rear stagnation point becoming eventually straight and horizontal.

Figures 5.2 and 5.4 display the time evolution of the vorticity contours at the Reynolds numbers $Re = 100$ in the absence of control and with open loop control when the interaction parameter is $N = 2$ and aspect ratio is 0.4. Vortex shedding is fully developed at time $t = 560$ second for the flow at Reynolds number $Re = 100$. When control is applied, one pair of vortices sheds away from the cylinder but the new vorticity formed on the cylinder stays attached to the solid surface. The intensity of vorticity, greatly reduced, is concentrated in two vorticity trails in the rear of the cylinder. The vortex shedding control occurs very fast, in about one vortex shedding cycle, i.e. about 10 seconds.

Figures 5.3 and 5.5 show the time evolution of the flow streamlines for the same flow as those displayed in Figures 5.2 and 5.4. Without control, the streamlines show strong curvatures past the cylinder typical of upper and lower flow vortices. The shedding of the vortices is also obvious from the streamline patterns. With control, the streamlines flatten so that the one connected to the rear stagnation point eventually becomes straight and horizontal. The other streamlines become fully symmetric with respect to the centerline.

5.3 Closed-loop Control

Closed-loop control uses a combination of actuators and sensors. Sensors are utilized to detect flow information and send feedback to the actuators. Actuators exert a force or energy in the fluid to control the flow based on the information received from the sensors (Figure 5.6). This control takes place through a flow adjustment by the actuators in order to optimize a certain cost function. In many theoretical and/or numerical studies,

actuators and sensors are located in the fluid itself, which, in addition of potentially disturbing the flow, may not be convenient in many practical applications.

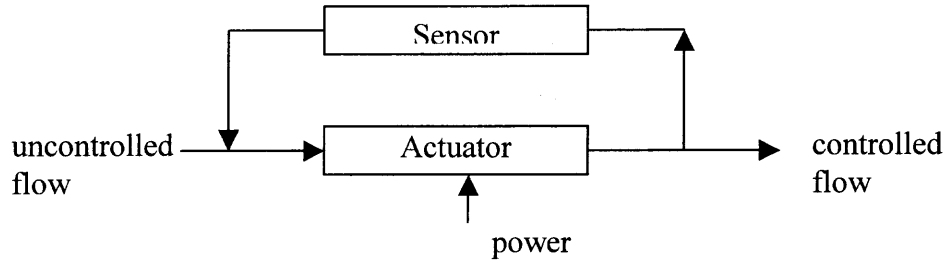


Figure 5.6 Schematics of closed-loop control.

Closed-loop control is usually based on a cost function that is needed in order to determine the suitable parameters for control. For example, Li *et al.* (2000) used the time averaged enstrophy as the cost function:

$$J_z = \frac{1}{2} \int_1^2 \int_{\Omega} \zeta^2 d\Omega dt \quad (5.5)$$

where $\zeta = \nabla \times \bar{u}$ refers to the vorticity and Ω is the whole computational domain.

This expression of the cost function, while attractive theoretically, requires the vorticity at all points in the flow domain as time evolves, and, therefore, may not be suitable in many applications.

Another approach consists in collecting the flow information only at the cylinder surface. Min and Choi (1999) devised the three following cost functions based on the pressure at the cylinder wall,

$$J_1(\phi) = \int -p(\theta)|_{r=R} \cos\theta R d\theta \quad (5.6a)$$

$$J_2(\phi) = \int (p_t(\theta) - p(\theta)|_{r=R})^2 \cos\theta R d\theta \quad (5.6b)$$

$$J_3(\phi) = \frac{1}{2} \int \left(\left. \frac{\partial p(\theta)}{\partial \theta} \right|_{r=R} \right)^2 \cos \theta R d\theta \quad (5.6c)$$

where R refers to the radius of cylinder, p is the pressure on the cylinder and p_t the target pressure on the cylinder surface as well (Figure 5.7).

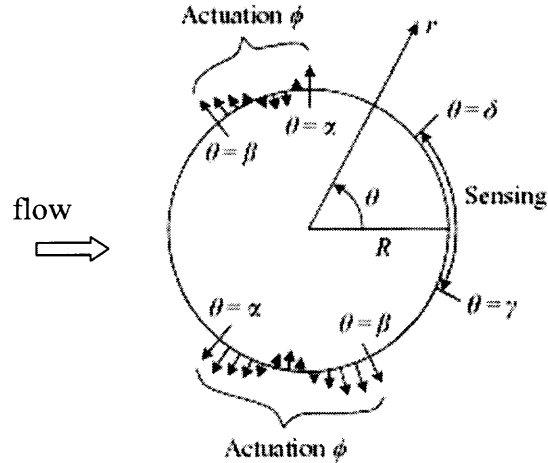


Figure 5.7 Schematics of actuation and sensing arrangement on the cylindrical surface.

The idea behind the three previous functions is to compare the pressure of the viscous flow to that of the potential flow. Indeed, if the flow is potential, all three cost functions (5.6a-c) vanish if p_t is chosen to be the potential flow pressure on the cylinder surface. Minimizing these three cost functions thus makes the viscous flow as close to the potential flow as possible.

Another way to approach closed-loop control is to target flow separation from the solid surface and design a control algorithm to avoid it. In this case, as in the situation of the potential flow, the fluid follows the cylinder in a smooth fashion. Flow separation occurs when the local derivative of the tangential velocity on the cylinder surface

becomes less than zero in the upper half-plane or greater than zero in the lower half-plane. A sensor detecting flow separation would thus measure the vorticity on the cylinder surface. According to the no-slip boundary condition, the velocity on the cylinder surface satisfies $u_\theta = u_r = 0$ and $\frac{\partial u_r}{\partial \theta} = \frac{\partial u_\theta}{\partial \theta} = 0$, which makes the vorticity

there reduce to $\omega = \nabla \times \vec{u} = \frac{\partial u_\theta}{\partial r}$. The latter is proportional to the wall shear stress since,

at the wall,

$$\tau_{r\theta} = \mu \left[r \frac{\partial}{\partial r} \left(\frac{u_\theta}{r} \right) + \frac{1}{r} \frac{\partial u_r}{\partial \theta} \right] = \frac{1}{2} \rho u_\infty^2 \frac{4}{\text{Re}} \Omega_{surf} \quad (2.28)$$

or, equivalently,

$$\Omega_{surf} = \text{Re} \frac{\tau_{surf}}{2 \rho u_\infty^2} \quad (5.7)$$

In other words, the local vorticity on the cylinder surface can be detected by means of shear stress sensors. The detection of the flow separation point requires an array of sensors on the entire cylinder surface, $0 \leq \theta \leq 2\pi$. Since after control, the flow is symmetric with respect to the centerline, sensors are placed only on the upper semi-cylinder. Since flow separation is characterized by negative local vorticity, the objective control function is chosen to $\delta > |\omega_{\min}| > 0$ along the upper semi-cylinder.

The control algorithm is realized by the bilinear searching method as follows.

$$\text{If } \omega_{\min} > \delta > 0 \text{ or } \omega_{\min} < -\delta, N^{new} = N^{old} - \alpha \frac{\omega_{\min}}{1 + |\omega_{\min}|} (\Delta N)_{preset} \quad (5.8a)$$

$$\text{If } \omega_{\min} < |\delta|, N^{new} = N^{old} - \alpha \frac{\delta}{1 + |\omega_{\min}|} (\Delta N)_{preset} \quad (5.8b)$$

Figure 5.8 demonstrates the effect of such a closed loop control algorithm on the flow vorticity contours at the Reynolds number $Re = 100$ and aspect ratio 0.4. As before, control starts to be applied at time $t = 560$ second and the actuation area for the electromagnetic field lies in the interval $[\theta_1 = 5^\circ, \theta_2 = 175^\circ]$ on the upper cylinder surface, and symmetrically on the lower surface. The flow dynamics under control is very similar to that observed in the case of open flow control. A vortex trail forms behind the cylinder, which remains attached to the body. It takes about 10 seconds to suppress the shedding of the vortices attached to the cylinder.

Figures 5.9-5.12 display the time history of the flow parameters such as drag coefficient C_d , lift coefficient C_L , interaction parameter N , and vorticity at the rear stagnation point ω_{rear} for the controlled flow. It is observed that after a large decrease of the drag shortly after the control is applied, the drag coefficient settles at a constant value approximately equal to the mean drag of the flow before control. The lift oscillations also disappear altogether, thus making the lift zero. One can clearly see that it takes one vortex shedding period for the control to suppress the shedding of the vortices born on the cylinder surface. The time history of the interaction parameter shows that the magnitude of the Lorentz force increases sharply to a value slightly above $N = 2$. Finally, the vorticity at the rear stagnation point fully vanishes under control.

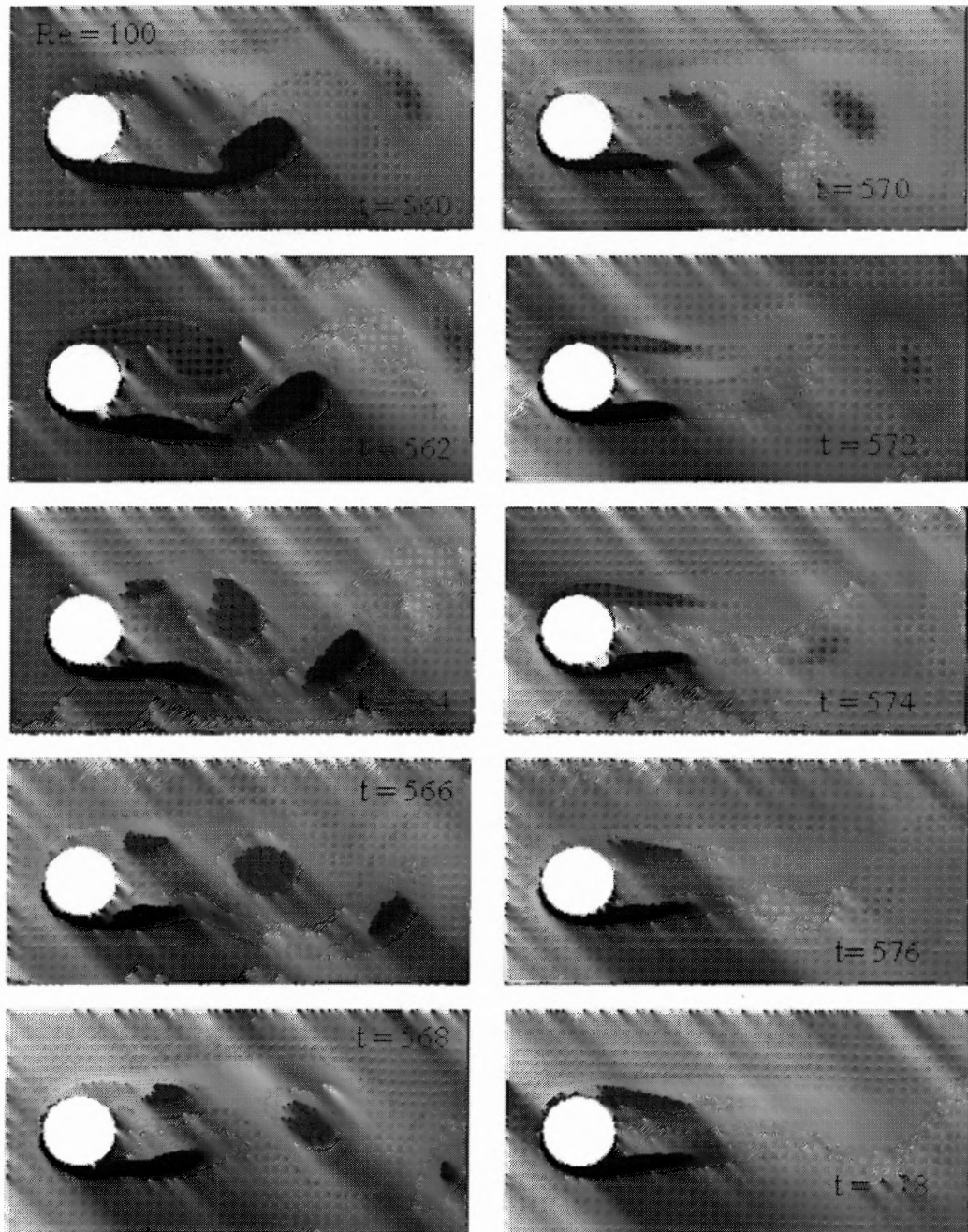


Figure 5.8 Visualization of the flow by vorticity contours after closed loop control (using the algorithm given by Equation (5.8) in the text) at the Reynolds number $Re = 100$. This clearly shows that vortex shedding is fully suppressed by closed loop control.

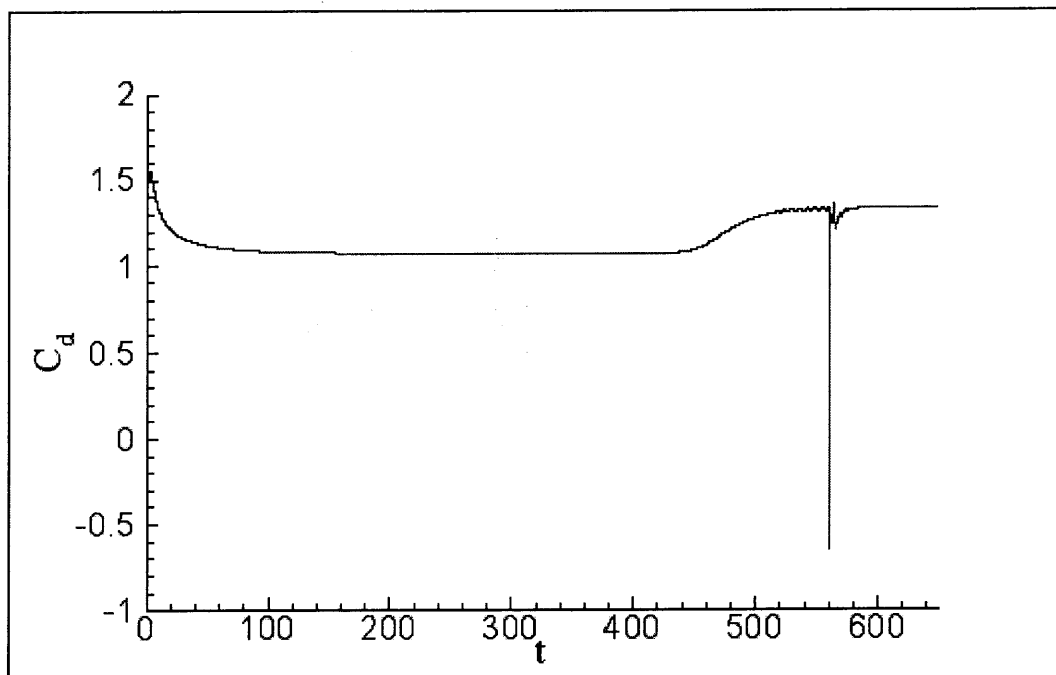


Figure 5.9 Time history of the drag coefficient for the closed-loop controlled flow of Figure 5.8.

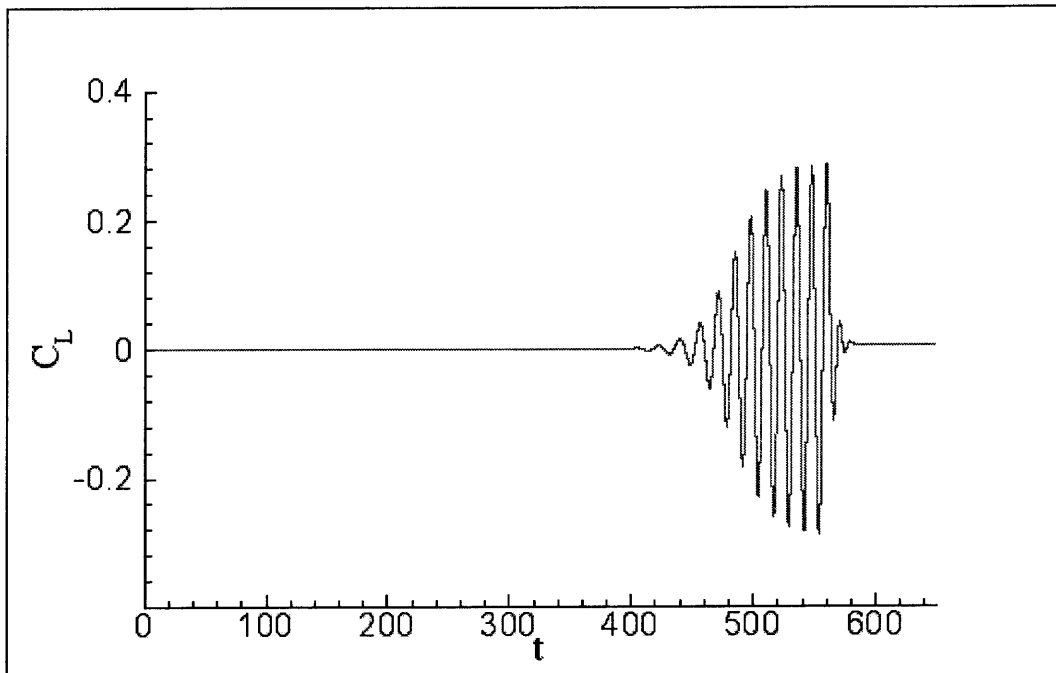


Figure 5.10 Time history of the lift coefficient for the closed-loop controlled flow of Figure 5.8.

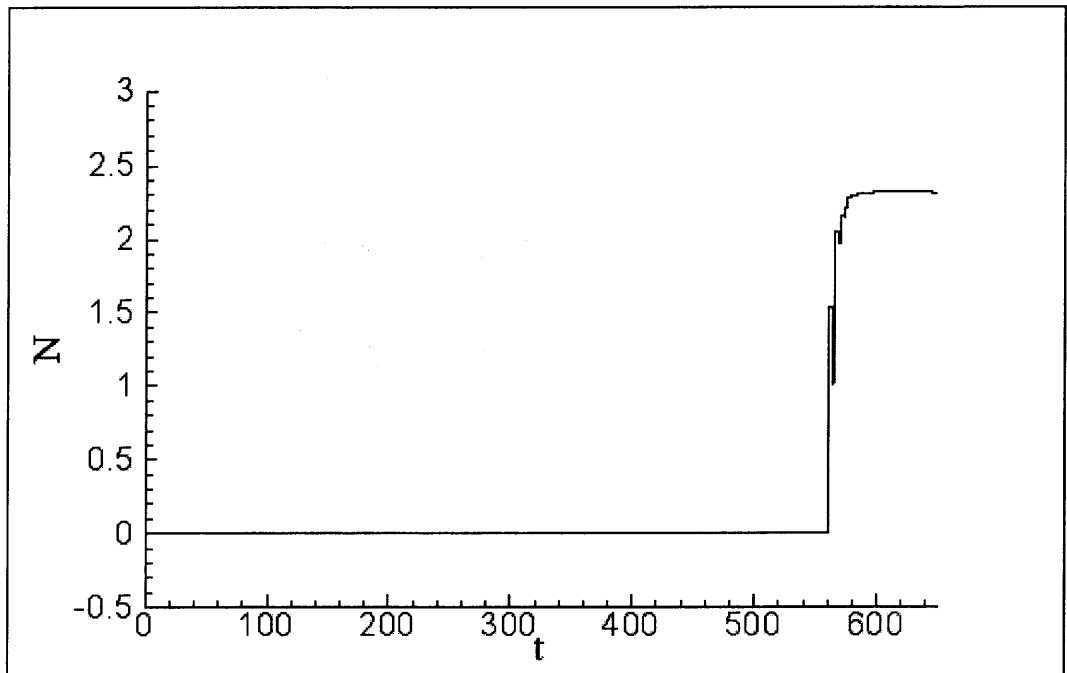


Figure 5.11 Time history of the interaction parameter N for the closed-loop control flow of Figure 5.8.

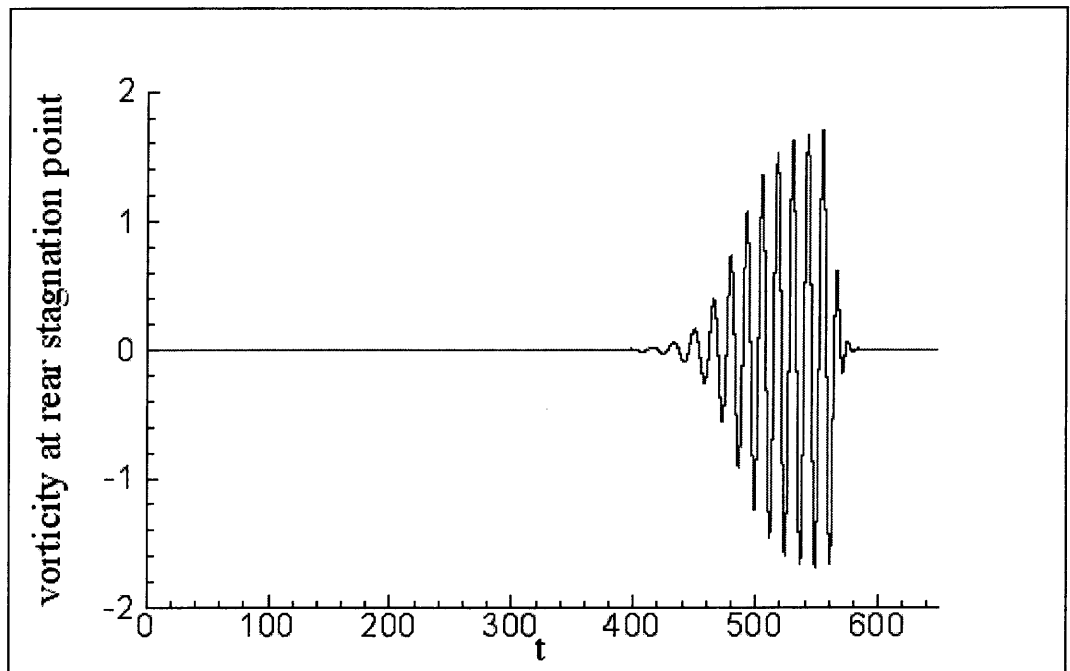


Figure 5.12 Time history of the vorticity at the rear stagnation point for the closed loop controlled flow of Figure 5.8.

In order to test the robustness of the closed-loop control algorithm, the same technique is applied to the flow at the Reynolds number $Re = 200$. Figure 5.13 visualizes the flow by vorticity contours after control. Comparing Figure 5.13 with Figure 5.8, it is clear that the intensity of vorticity is much larger at the Reynolds number $Re = 200$ than at $Re = 100$. Nevertheless, the control technique works efficiently in this case too. As in the previous case, the flow is controlled after one vortex shedding period, the drag decreases abruptly to increase again to its stable value below that of the uncontrolled flow, and the lift and vorticity at the rear stagnation point decrease to zero. The interaction parameter increases sharply to a value around two, slightly below that needed in the case of the Reynolds number $Re = 100$.

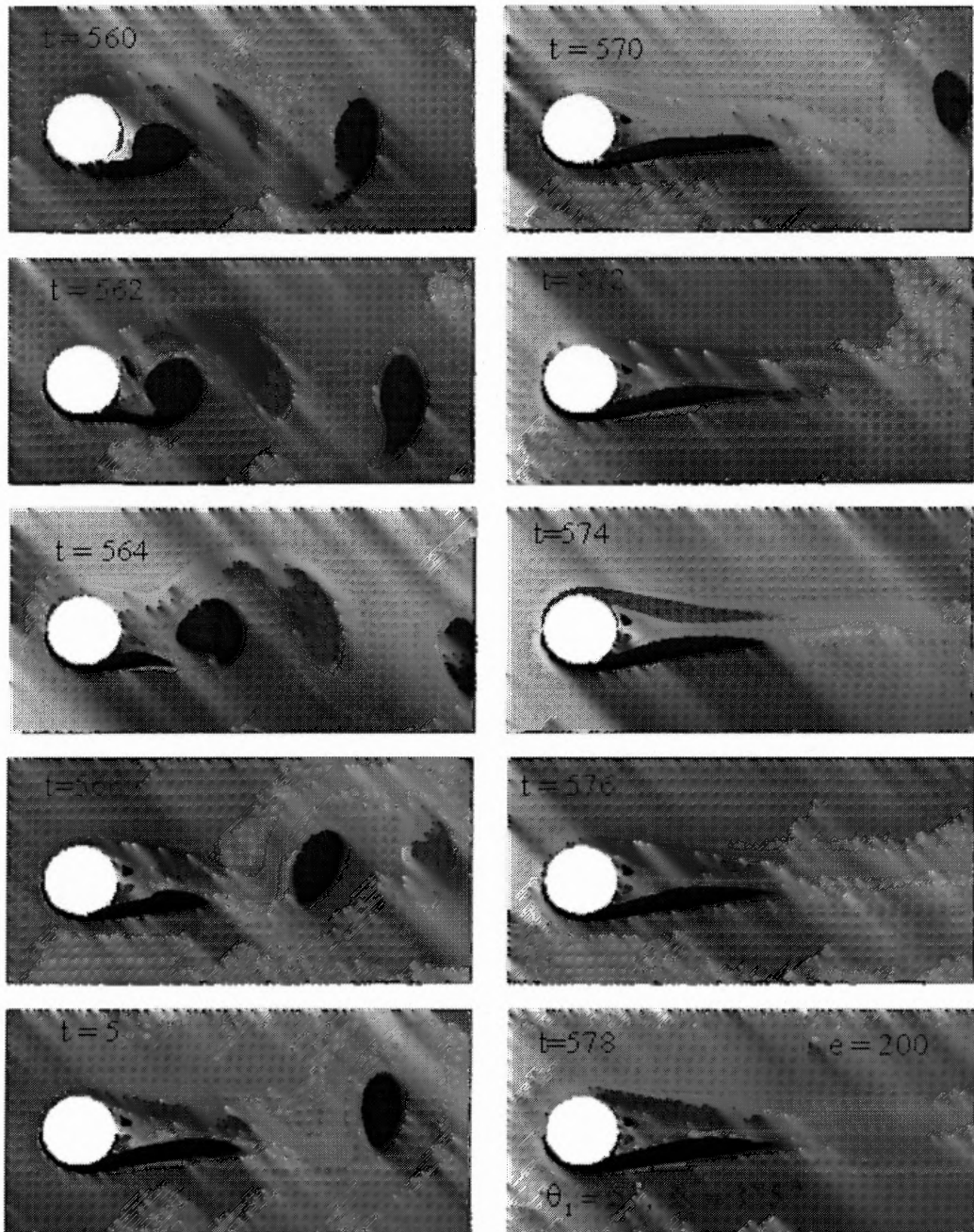


Figure 5.13 Visualization of the flow by vorticity contours after closed loop control (using the algorithm given by Equation (5.8) in the text) at the Reynolds number $Re = 200$. This clearly shows that vortex shedding is fully suppressed by closed loop control.

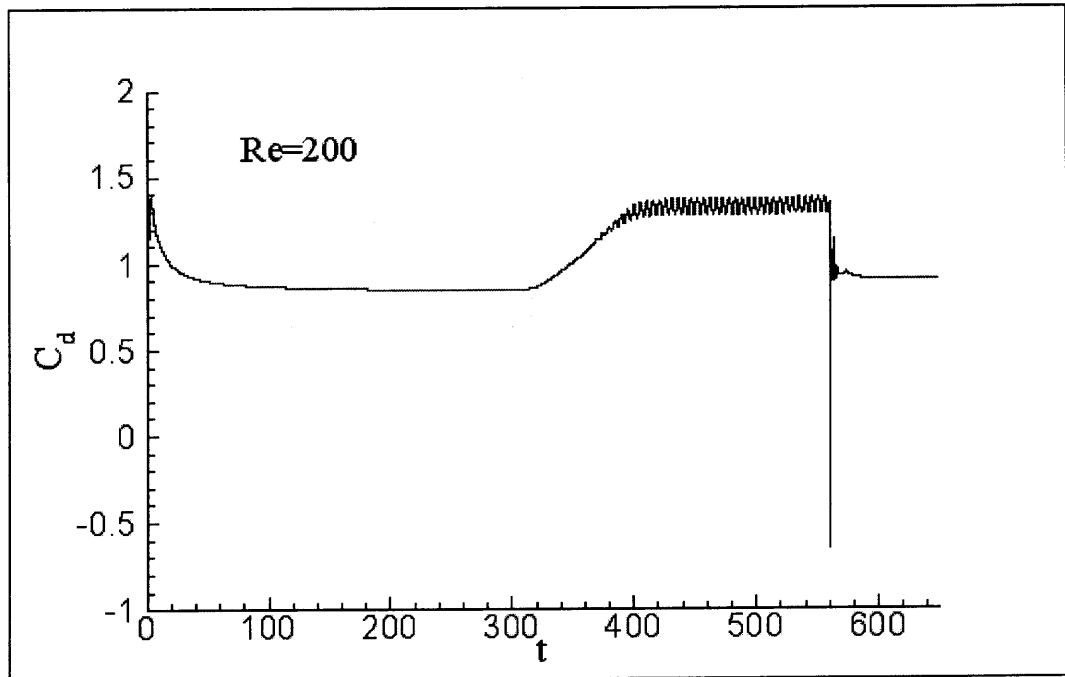


Figure 5.14 Time history of the drag coefficient for the closed-loop controlled flow of Figure 5.13.

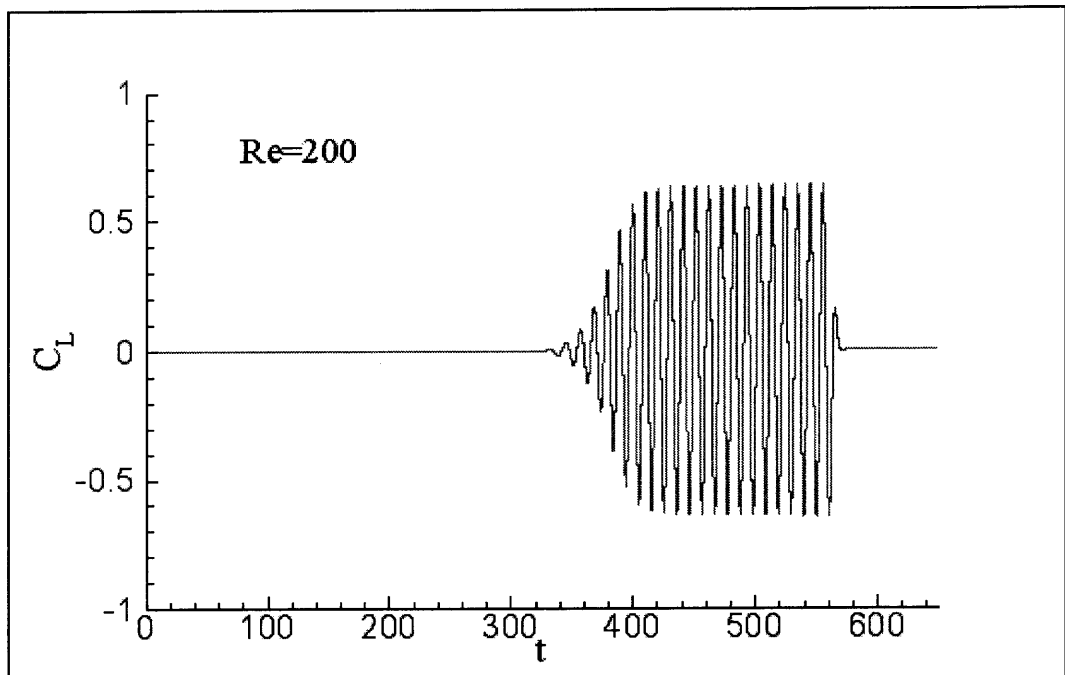


Figure 5.15 Time history of the lift coefficient for the closed-loop controlled flow of Figure 5.13.

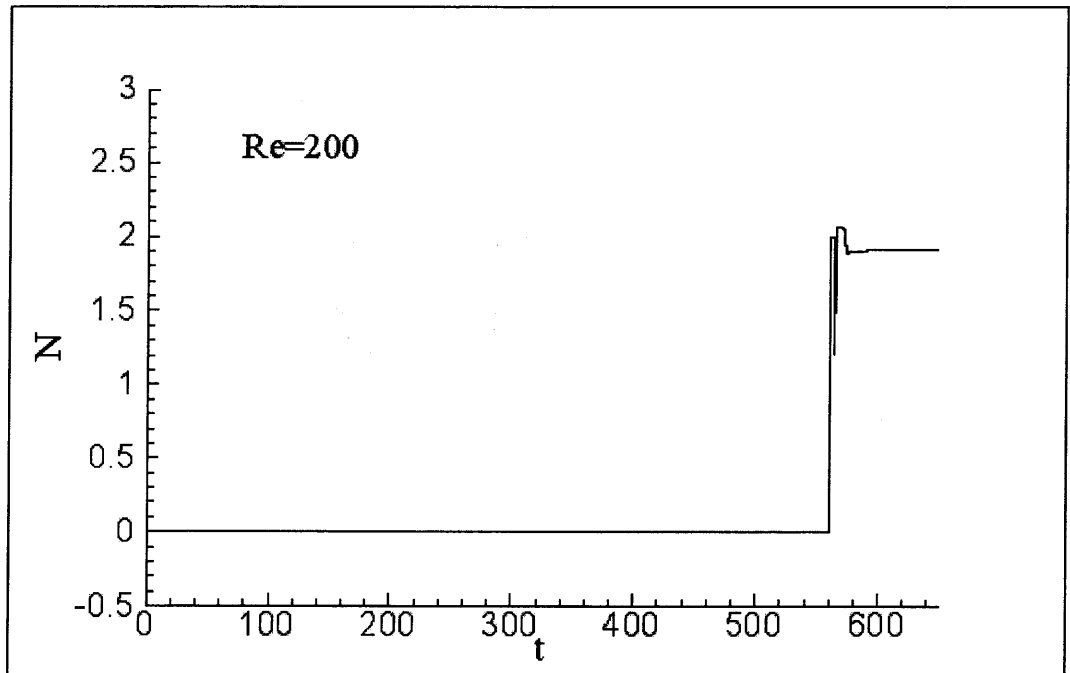


Figure 5.16 Time history of the interaction parameter for the closed-loop controlled flow of Figure 5.13.

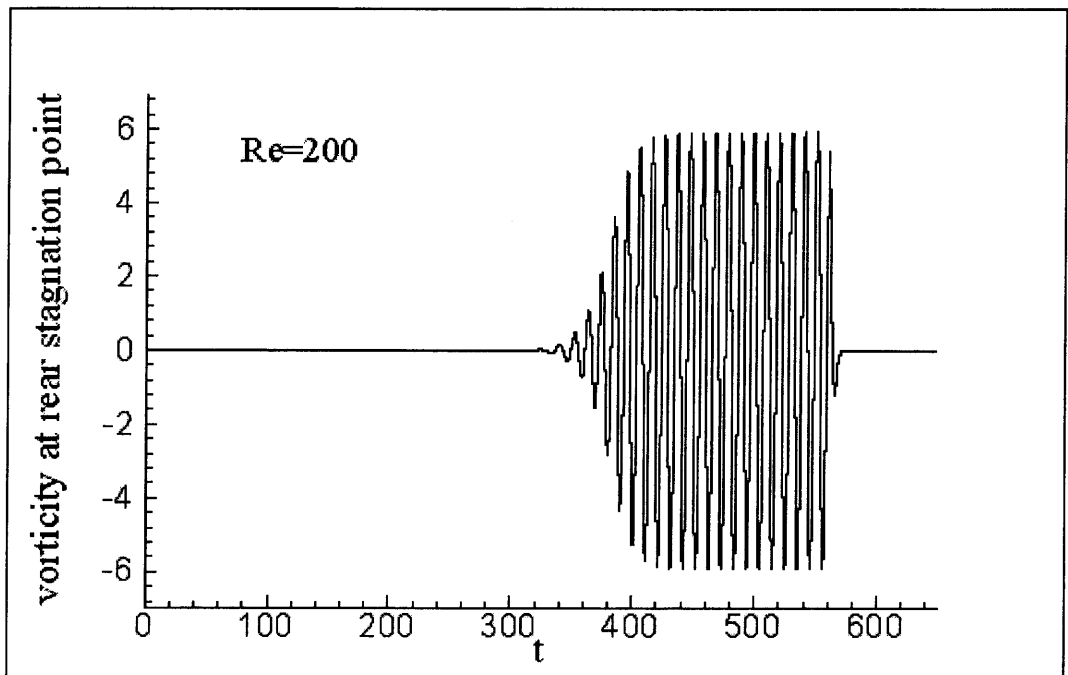


Figure 5.17 Time history of the vorticity at the rear stagnation point for the closed-loop controlled flow of Figure 5.13.

5.4 Closed-loop Control with a Single Sensor

A challenging problem is to investigate how many sensors one needs in order to detect sufficient information for the implementation of an efficient closed-loop control algorithm. In the previous section, one needed sensors along the whole cylinder surface. Would it be possible to decrease this information to only one single point, and, therefore, use one sensor only? One particular point that plays an important role is the rear stagnation point, which is selected in the present work for positioning one single sensor and deriving an alternative closed-loop control algorithm. As before, the vorticity (or, equivalently, the wall shear stress) is selected as the tested variable and its value at the rear stagnation point is denoted ω_{rear} . Ideally, the value of ω_{rear} should be zero in a perfectly controlled flow. In both numerical simulations and experiments, it is never exactly zero due to noise and, therefore, the objective function is set to be smaller in absolute value than a small threshold, δ , such that

$$-\delta < \omega_{rear} < \delta \quad (5.9)$$

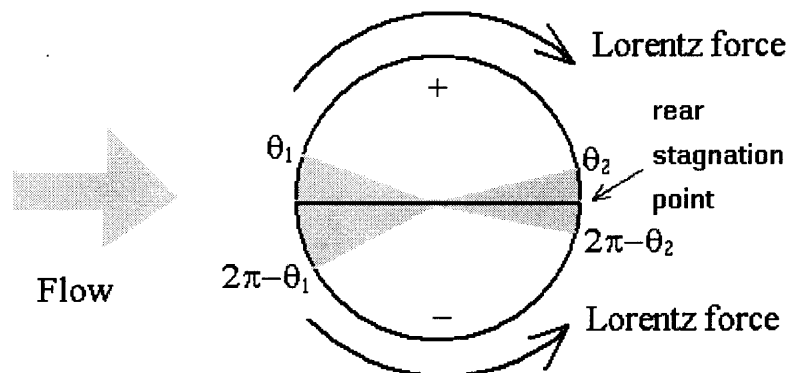


Figure 5.18 Detecting position of the single sensor closed-loop control algorithm.

If the flow is controllable, the larger the magnitude of the Lorentz force, the smaller the absolute value of the vorticity at the rear stagnation point. Based on this idea, the control algorithm is realized by using the linear searching method in the following manner.

If $\omega_{rear} > \delta > 0$,

$$N^{new} = N^{old} + \alpha \frac{\omega_{rear}}{1 + \omega_{rear}} (\Delta N)_{preset} \quad (5.10a)$$

If $\omega_{rear} < -\delta < 0$,

$$N^{new} = N^{old} - \alpha \frac{\omega_{rear}}{1 - \omega_{rear}} (\Delta N)_{preset} \quad (5.10b)$$

If $-\delta \leq \omega_{rear} \leq \delta$,

$$N^{new} = N^{old} - \beta \frac{\exp(1 - \omega_{rear} / \delta) - 1}{e - 1} (\Delta N)_{preset} \quad (5.10c)$$

In order to investigate the suitable interaction parameter N for various actuation angle areas, the following different actuation angles are selected.

Case I: $\theta_1 = 5^\circ$, $\theta_2 = 175^\circ$.

Case II: $\theta_1 = 60^\circ$, $\theta_2 = 175^\circ$.

Case III: $\theta_1 = 90^\circ$, $\theta_2 = 175^\circ$.

Case IV: $\theta_1 = 120^\circ$, $\theta_2 = 175^\circ$.

Case V: $\theta_1 = 50^\circ$, $\theta_2 = 135^\circ$.

The single sensor closed-loop control algorithm is applied numerically to the flow at the two Reynolds number $Re = 100$ and $Re = 200$ and aspect ratio 0.4.

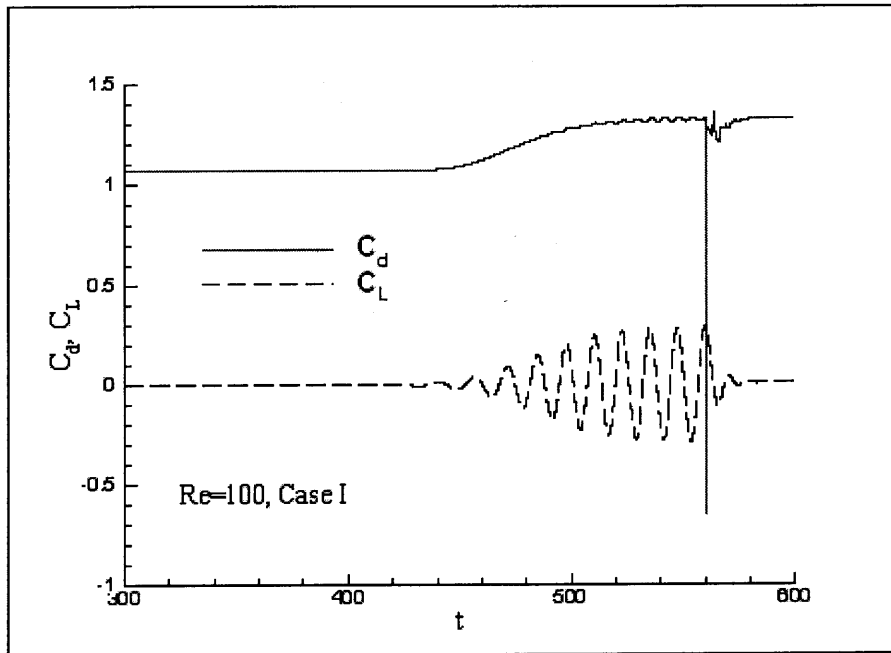


Figure 5.19 Drag and lift coefficients C_d and C_L for the closed-loop controlled flow with a single sensor at the Reynolds number $Re = 100$, in Case I described in the text.

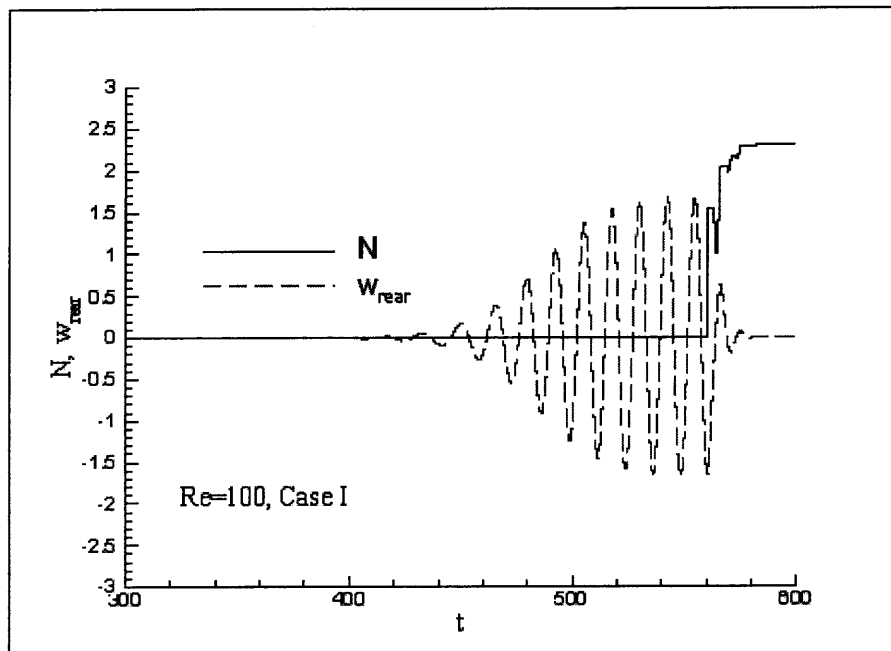


Figure 5.20 Interaction parameter N and vorticity ω_{rear} at the rear stagnation point for the closed-loop controlled flow with a single sensor at the Reynolds number $Re = 100$, in Case I described in the text.

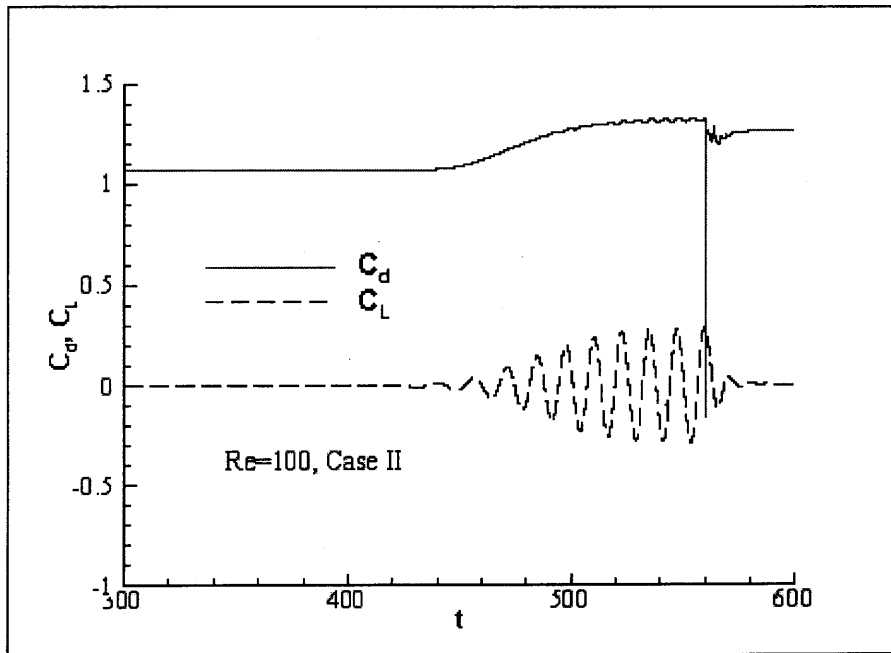


Figure 5.21 Drag and lift coefficients C_d and C_L for the closed-loop controlled flow with a single sensor at the Reynolds number $Re = 100$, in Case II described in the text.

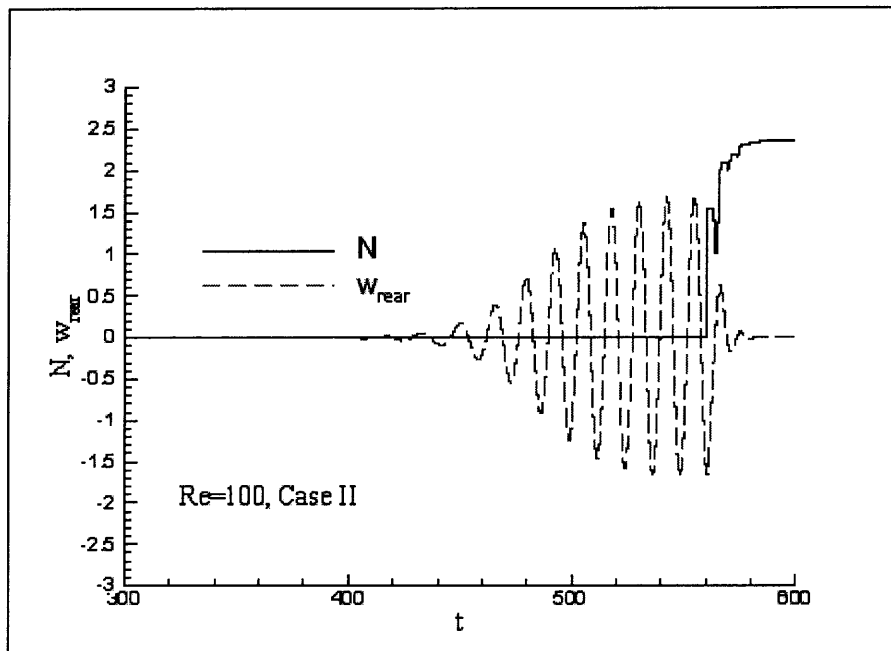


Figure 5.22 Interaction parameter N and vorticity ω_{rear} at the rear stagnation point for the closed-loop controlled flow with a single sensor at the Reynolds number $Re = 100$, in Case II described in the text.

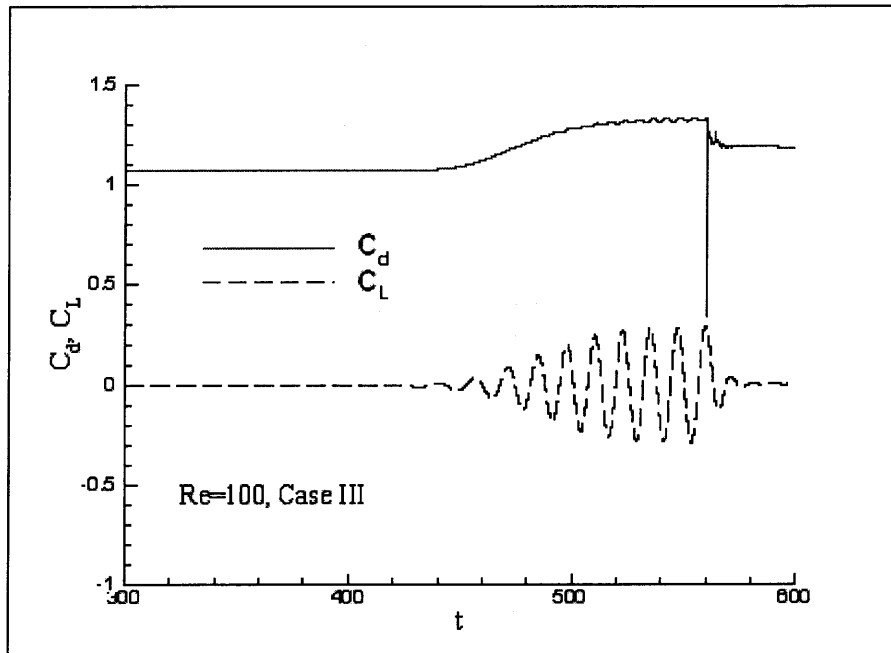


Figure 5.23 Drag and lift coefficients C_d and C_L for the closed-loop controlled flow with a single sensor at the Reynolds number $Re = 100$, in Case III described in the text.

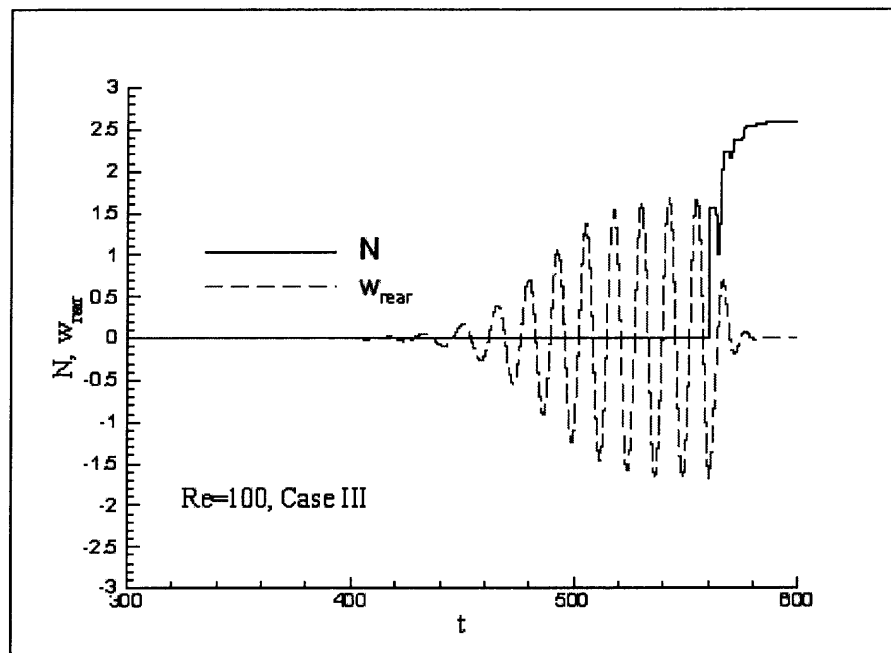


Figure 5.24 Interaction parameter N and vorticity ω_{rear} at the rear stagnation point for the closed-loop controlled flow with a single sensor at the Reynolds number $Re = 100$, in Case III described in the text.

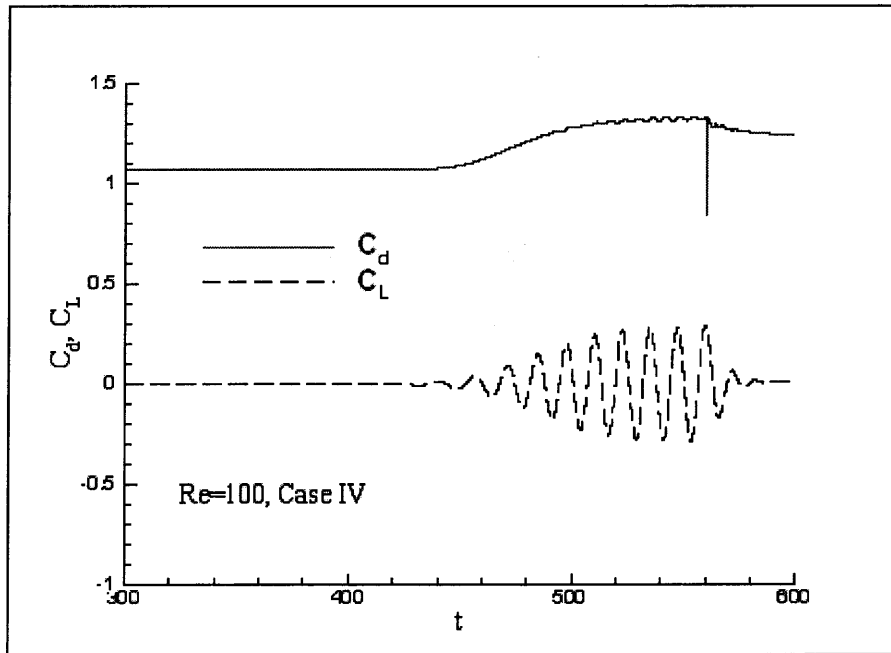


Figure 5.25 Drag and lift coefficients C_d and C_L for the closed-loop controlled flow with a single sensor at the Reynolds number $Re = 100$, in Case III described in the text.

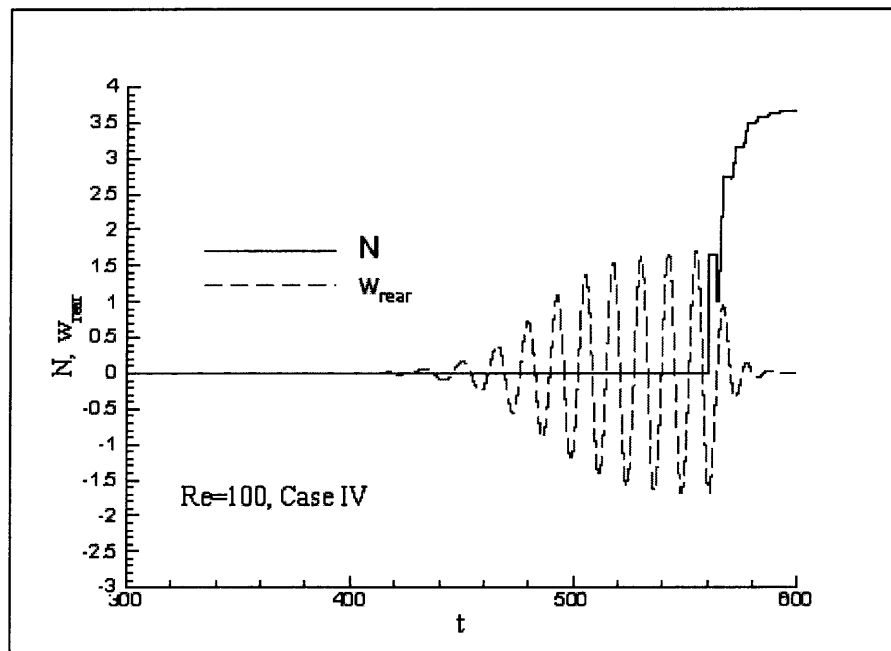


Figure 5.26 Interaction parameter N and vorticity ω_{rear} at the rear stagnation point for the closed-loop controlled flow with a single sensor at the Reynolds number $Re = 100$, in Case IV described in the text.

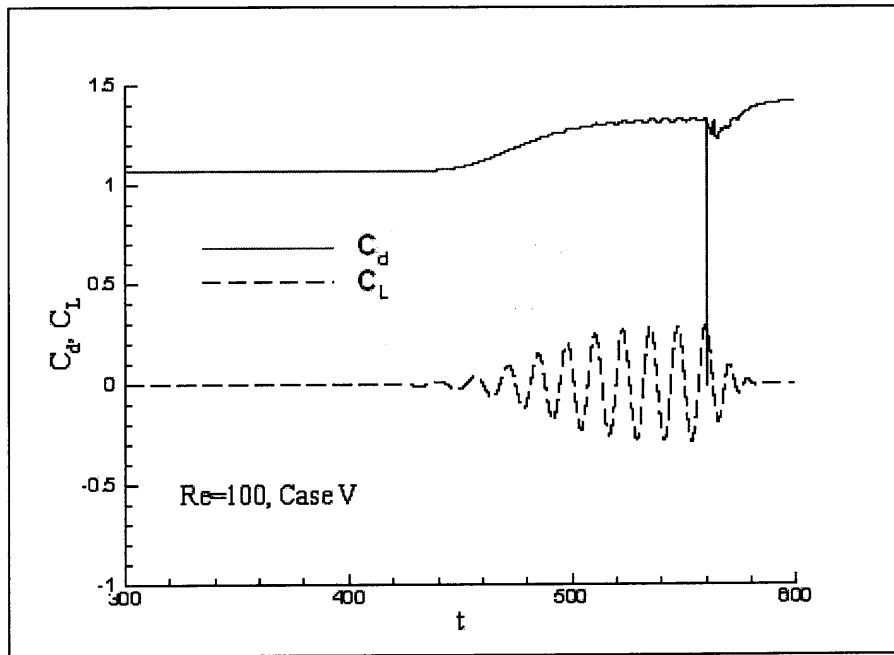


Figure 5.27 Drag and lift coefficients C_d and C_L for the closed-loop controlled flow with a single sensor at the Reynolds number $Re = 100$, in Case V described in the text.

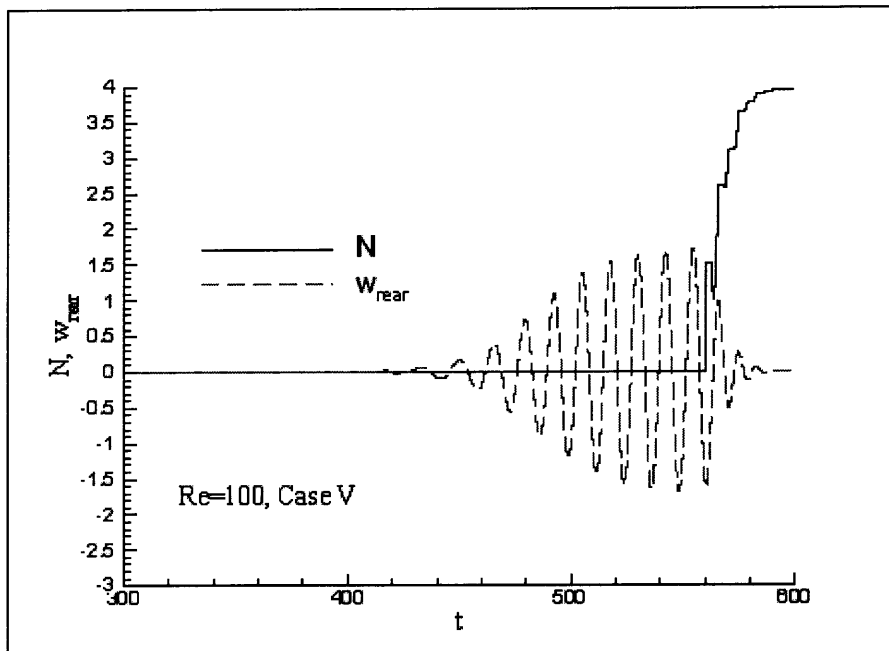


Figure 5.28 Interaction parameter N and vorticity w_{rear} at the rear stagnation point for the closed-loop controlled flow with a single sensor at the Reynolds number $Re = 100$, in Case V described in the text.

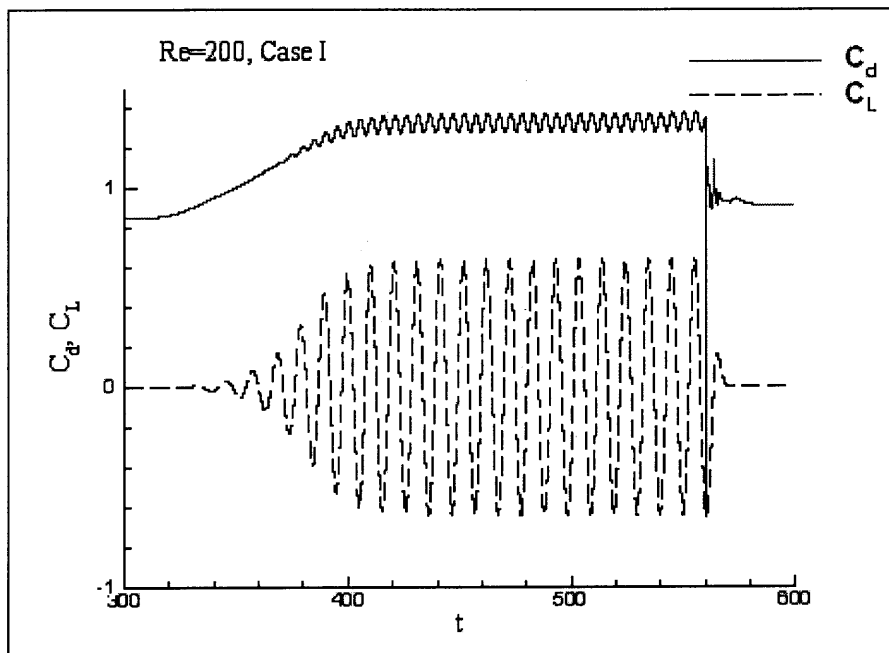


Figure 5.29 Drag and lift coefficients C_d and C_L for the closed-loop controlled flow with a single sensor at the Reynolds number $Re = 200$, in Case I described in the text.

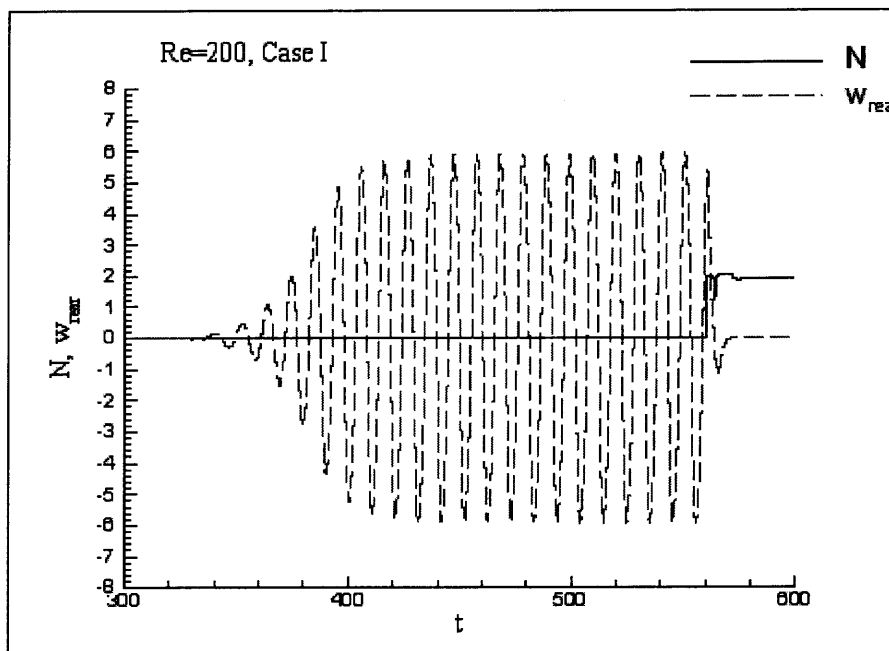


Figure 5.30 Interaction parameter N and vorticity ω_{rear} at the rear stagnation point for the closed-loop controlled flow with a single sensor at the Reynolds number $Re = 200$, in Case I described in the text.

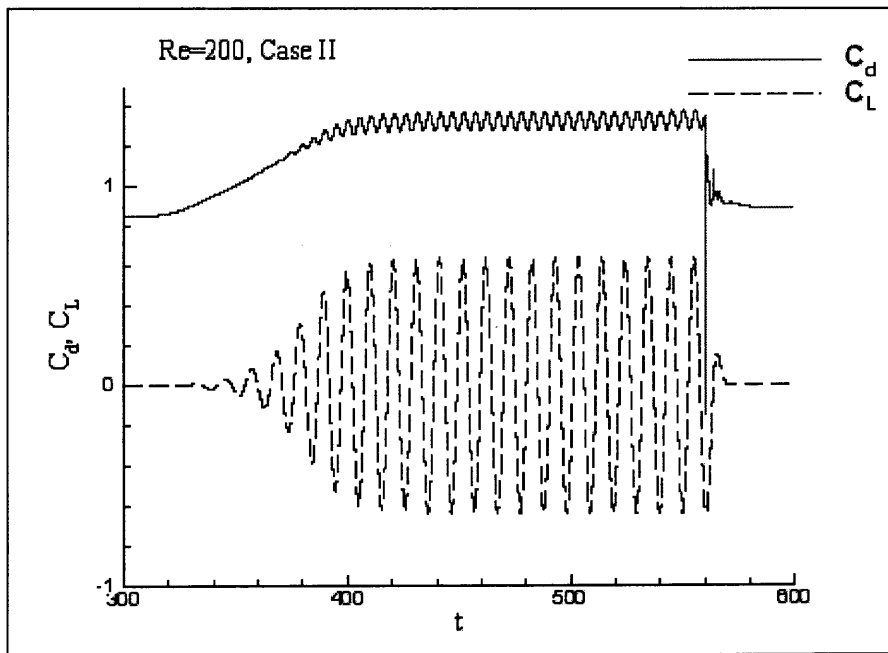


Figure 5.31 Drag and lift coefficients C_d and C_L for the closed-loop controlled flow with a single sensor at the Reynolds number $Re = 200$, in Case II described in the text.

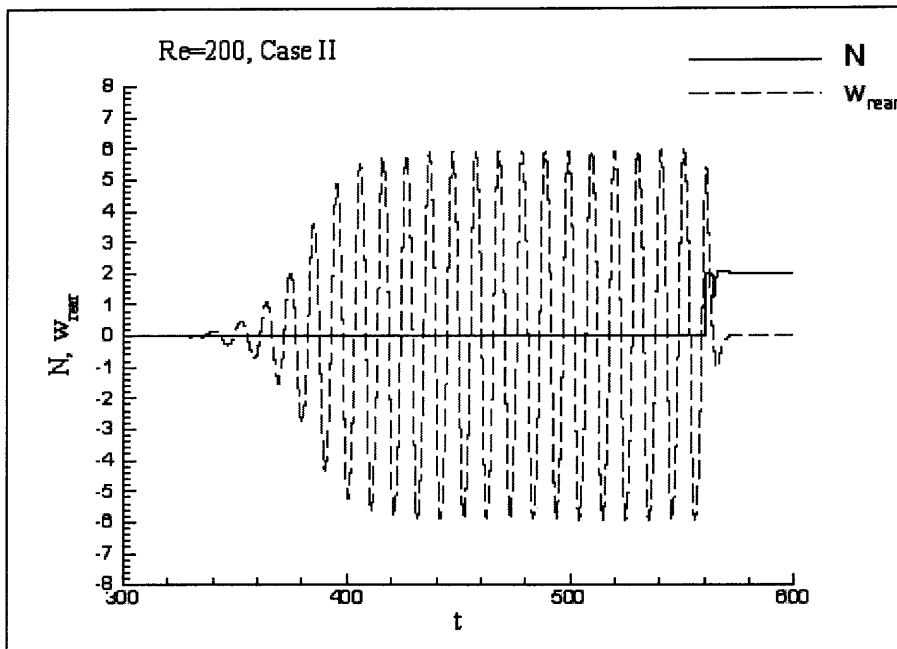


Figure 5.32 Interaction parameter N and vorticity ω_{rear} at the rear stagnation point for the closed-loop controlled flow with a single sensor at the Reynolds number $Re = 200$, in Case II described in the text.

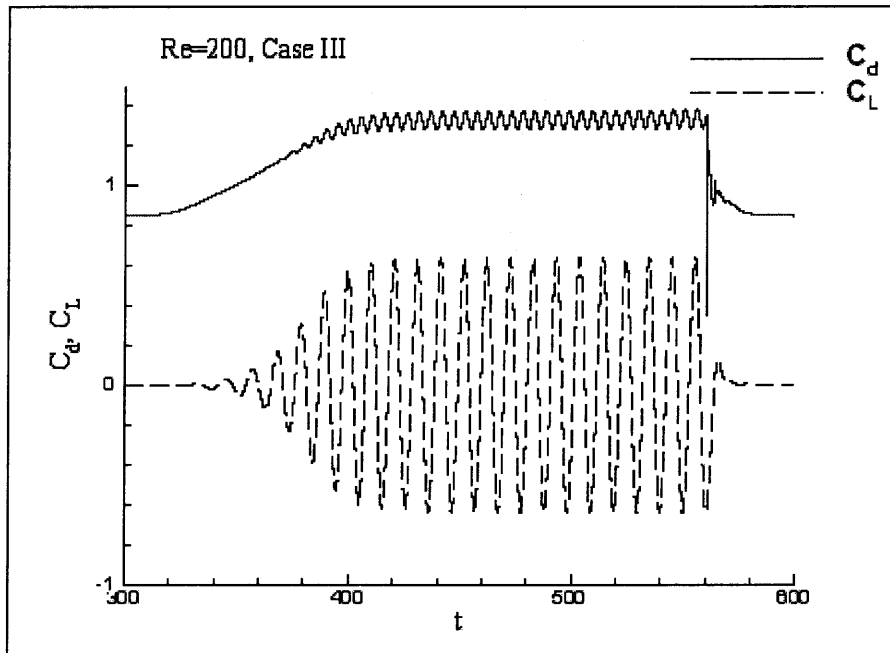


Figure 5.33 Drag and lift coefficients C_d and C_L for the closed-loop controlled flow with a single sensor at the Reynolds number $Re = 200$, in Case III described in the text.

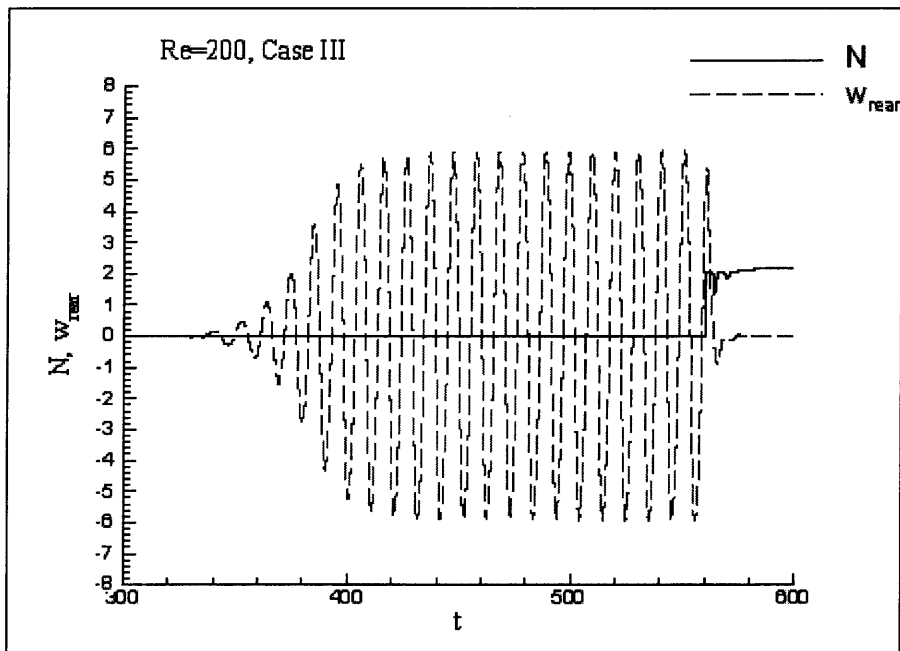


Figure 5.34 Interaction parameter N and vorticity ω_{rear} at the rear stagnation point for the closed-loop controlled flow with a single sensor at the Reynolds number $Re = 200$, in Case III described in the text.

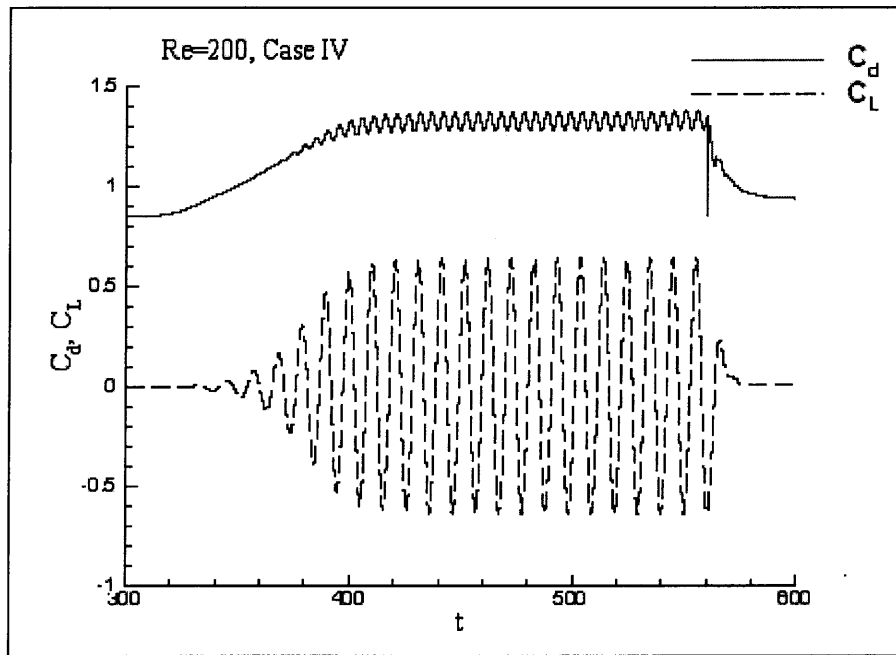


Figure 5.35 Drag and lift coefficients C_d and C_L for the closed-loop controlled flow with a single sensor at the Reynolds number $Re = 200$, in Case IV described in the text.

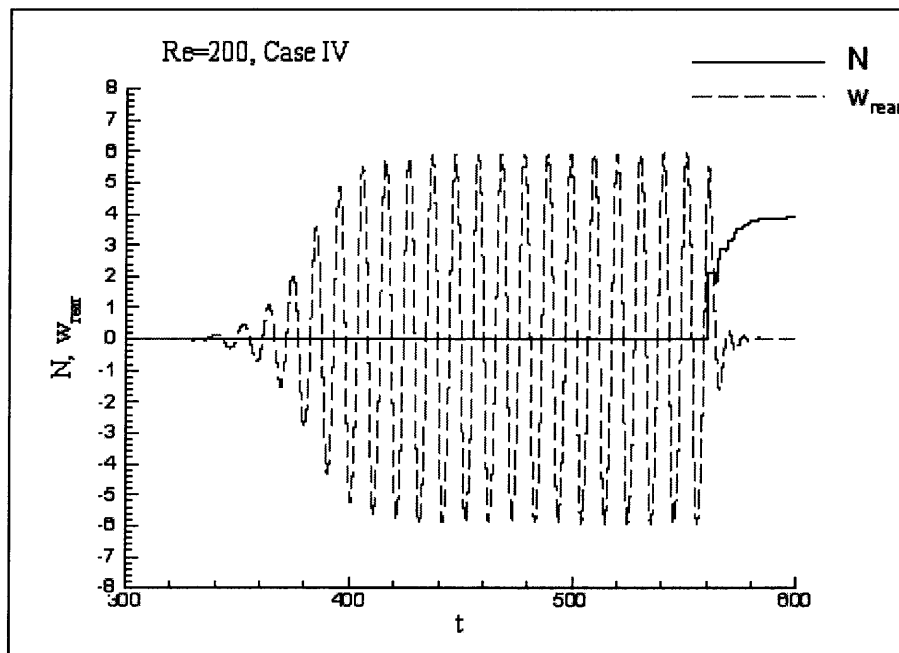


Figure 5.36 Interaction parameter N and vorticity ω_{rear} at the rear stagnation point for the closed-loop controlled flow with a single sensor at the Reynolds number $Re = 200$, in Case IV described in the text.

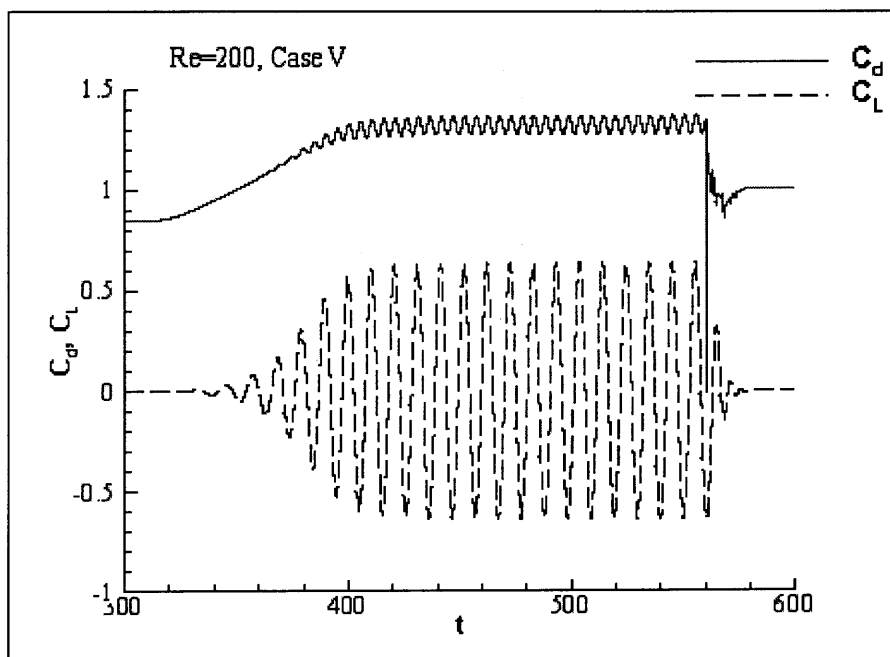


Figure 5.37 Drag and lift coefficients C_d and C_L for the closed-loop controlled flow with a single sensor at the Reynolds number $Re = 200$, in Case V described in the text.

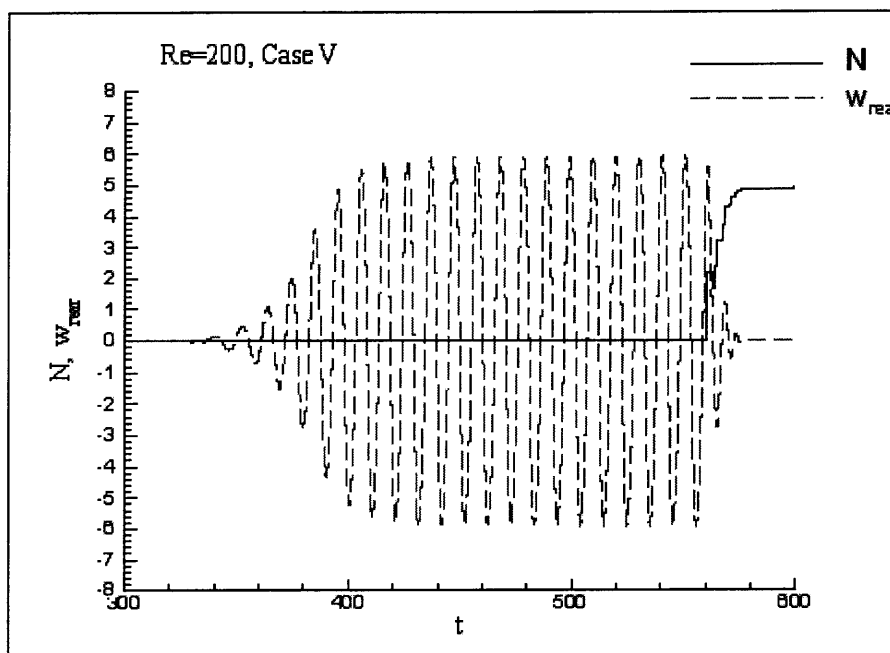


Figure 5.38 Interaction parameter N and vorticity ω_{rear} at the rear stagnation point for the closed-loop controlled flow with a single sensor at the Reynolds number $Re = 200$, in Case V described in the text.

Figures 5.19 - 5.28 show the drag coefficient C_d , the lift coefficient C_L , the interaction parameter N , and the vorticity ω_{rear} at the rear stagnation point for the closed-loop controlled flow with a single sensor at the Reynolds number $Re = 100$. The control starts at time $t = 560$ seconds. It shows that the extent and location of the actuation area plays a role in the controlled flow, particularly in the drag coefficient. The drag coefficient obtained in Case I is almost identical to the average drag of the uncontrolled flow, but is smaller in Cases II – IV (being the smaller in Case III) and larger in Case V. Furthermore, the value of the interaction parameter also varies with the actuation area.

Figure 5.29 – 5.38 display the drag coefficient C_d , the lift coefficient C_L , the interaction parameter N , and the vorticity ω_{rear} at the rear stagnation point of the cylinder for the single sensor closed-loop controlled flow at the Reynolds number $Re = 200$. The control time starts at $t = 560$ second too. Compared to the previously studied flow (at the Reynolds number $Re=100$), the flow experiences stronger vorticity generated from the cylinder surface. Here again, the control is effective, fully suppressing vortex shedding, and making both the lift coefficient C_L and the vorticity at the rear stagnation point ω_{rear} go to zero. At both Reynolds numbers, it is interesting to notice that the lift and vorticity at the rear stagnation point go faster to zero than the drag and interaction parameter reach their stable value. The results of the numerical simulations after applying the single sensor closed loop control are summarized in Table 5.1 for $Re = 100$, and in Table 5.2 for $Re = 200$.

Table 5.1 Summary of the effect of the single sensor closed-loop control algorithm on the flow at the Reynolds number $Re = 100$, for various actuation areas.

Case	θ_1	θ_2	$\theta_2 - \theta_1$	N	$(\theta_2 - \theta_1) * N$	Result
I	5^0	175^0	170^0	2.31	6.85	controlled
II	60^0	175^0	115^0	2.34	4.70	controlled
III	90^0	175^0	85^0	2.59	3.84	controlled
IV	120^0	175^0	55^0	3.68	3.53	controlled
V	50^0	135^0	85^0	3.92	5.82	controlled

Table 5.2 Summary of the effect of the single sensor closed-loop control algorithm on the flow at the Reynolds number $Re = 200$, for various actuation areas.

Case	θ_1	θ_2	$\theta_2 - \theta_1$	N	$(\theta_2 - \theta_1) * N$	Result
I	5^0	175^0	170^0	1.91	5.67	controlled
II	60^0	175^0	115^0	1.99	3.99	controlled
III	90^0	175^0	85^0	2.17	3.22	controlled
IV	120^0	175^0	55^0	4.16	3.99	controlled
V	50^0	135^0	85^0	5.18	7.68	controlled

From this tables, it can be deduced that the angle defining the actuation area $\theta_2 - \theta_1$ and the value of the interaction parameter N are directly related. Generally speaking, the interaction parameter increases when the actuation area decreases, although the location of the actuation does play a role as well. For example, when the starting angle varies from $\theta_1 = 5^0$ to $\theta_1 = 90^0$, the interaction parameter N increases slowly. In contrast, when the starting angle varies from $\theta_1 = 90^0$ to $\theta_1 = 120^0$, the interaction parameter N increases fast. This means that actuators in the front of the cylinder plays a lesser role than those in the rear where vortex shedding occurs. The fact that the interaction parameter is not directly proportional to the inverse of the actuation area can

be seen by calculating the power needed to control the flow, that is the product $(\theta_2 - \theta_1) * N$ of the interaction parameter with the actuation area. This power is far from being constant between the various cases. At both Reynolds numbers studied here, the “best” control corresponding to the smallest power is given by Case III. In this case, the actuation area spans from 90^0 to 175^0 . It would be both challenging and interesting to derive an optimal control technique capable of determining both the intensity of the Lorentz force (i.e. the interaction parameter) and the actuation area, which not only minimizes a given cost function based on the flow physical parameters, but also minimizes the power needed to control the flow.

CHAPTER 6

CONCLUSIONS

Novel analytical expressions of the Lorentz force generated by an alternating arrangement of electrodes and magnets on a flat plate and a cylinder were derived using mathematical analysis. In the case of a flat plate, the decay of the electro-magnetic force with distance to the wall is described by the expression $2 \exp(-z)/[1 + \exp(-2z)]$ rather than $\exp(-z)$ for $z > 0$. The results of the numerical simulation of the Laplace equations (subjected to the Dirichlet boundary condition) are in close agreement with the novel expression.

In the application of the Lorentz force in the case of a circular cylinder, the Dirichlet boundary condition is also assumed for the electric and magnetic potentials. An analytical expression is also derived in this case, showing that the distribution of the Lorentz force in the radius direction is a combination of modified Bessel functions of the second kind of various orders. When the radius of the cylinder tends to infinity, this expression is shown to reduce to the form of the force obtained in the case of a flat plate. It is further demonstrated that such an expression compares well with results of numerical simulations.

In the control of vortex shedding from a circular cylinder, the calculation of the Lorentz force is decoupled from the fluid mechanics problem under the assumption that the electric current induced by the magnetic field is small compared to that generated by the electric field, which is the case for fluids of low electric conductivity such as saltwater. The previous calculation of the Lorentz force then applies, and can be directly inserted into the fluid equations of motion, that is the Navier-Stokes equations. The electrodes and magnets are arranged symmetrically on both sides of the centerline so that the Lorentz

force is oriented in the flow direction with a preset actuation area along the cylinder surface. Both open and closed-loop control are investigated to suppress vortex shedding from the circular cylinder. Numerical simulations with open-loop control show that vortex shedding can be fully suppressed at both Reynolds numbers $Re = 100$ and $Re = 200$.

In the derivation of a closed-loop control algorithm, the vorticity on the surface of the cylinder is chosen as the cost function. While the control technique works well, the next step was to address the challenge of using only one sensor in the control loop. It was found that a single sensor strategically located at the rear stagnation point indeed suffices.

Next, the location of the actuation areas was studied in detail. Numerical investigations showed that the length and location of the actuation area played an important role in the control. It was found that with a fixed ending actuation angle, the magnitude of the force had to be increased with the decrease of the actuation area. Furthermore, actuators placed on the rear side of the cylinder were more efficient than actuators located on the front side.

When considering the power consumption in the control technique, it was found that the energy necessary to control the flow could vary with the location and extent of the actuation area. For instance, a less efficient technique using too much actuation area toward the front side of the cylinder unnecessarily increased the power consumption.

APPENDIX A

SOLUTION OF THE TWO-DIMENSIONAL LAPLACE EQUATION WITH DIRICHLET BOUNDARY CONDITIONS ON A CIRCLE

The Laplace equation subjected to the Dirichlet boundary conditions considered here is as follows:

$$\frac{1}{r} \frac{\partial}{\partial r} \left(r \frac{\partial K}{\partial r} \right) + \frac{1}{r^2} \frac{\partial^2 K}{\partial \theta^2} = 0 \quad (\text{A.1a})$$

$$K(b, \theta) = f(\theta) = \begin{cases} 1, & \theta_1 < \theta \leq \theta_2 \\ -1, & 2\pi - \theta_2 < \theta \leq 2\pi - \theta_1, r \geq b \\ 0, & \text{other } \theta \end{cases} \quad (\text{A.1b})$$

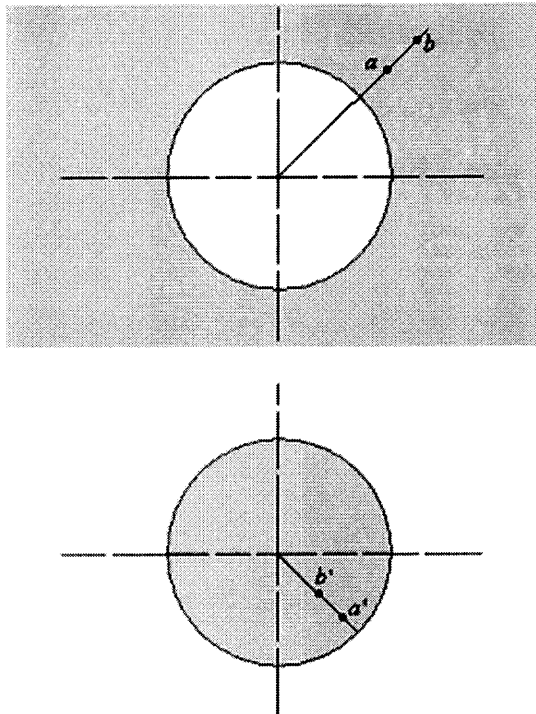


Figure A.1 Conformal mapping of the computational domain outside the cylinder to a circle.

By using the conformal mapping $w = \frac{1}{z}$, with z being the complex variable $z = x + iy$, the computational domain outside the circular cylinder in the z - plane is transformed into the domain inside a circle in the w - plane (see Figure A.1). The relation between the z - plane and the w - plane is given by

$$r_w = \frac{1}{r_z} \text{ and } \xi = 2\pi - \theta \quad (\text{A.2})$$

where $z = r_z e^{i\theta}$, $w = r_w e^{i\xi}$, the subscripts z and w refer to the z - and w -planes, respectively. The computational domain outside the cylinder of radius b is transformed into a circle of radius $r_0 = \frac{1}{b}$. Equation (A.1) becomes

$$\nabla^2 K(r_w, \theta) = 0, \quad 0 \leq r \leq a, \quad 0 \leq \theta \leq 2\pi \quad (\text{A.3a})$$

$$K(r_0, \xi) = f(\xi) = \begin{cases} -1 & \theta_1 < \xi < \theta_2 \\ 1 & 2\pi - \theta_2 < \xi < 2\pi - \theta_1, \quad r \leq r_0 \\ 0 & \text{otherwise} \end{cases} \quad (\text{A.3b})$$

Let $K(r_w, \xi) = \sum C_n R_n(r_w) S_n(\xi)$ where C_n are the constants to be determined.

Equation (A.3) becomes

$$\frac{r_w}{R_n} \frac{d}{dr_w} \left(r_w \frac{dR_n}{dr_w} \right) = -\frac{1}{S_n} \frac{d^2 S_n}{d\xi^2} = \lambda_n \quad (\text{A.4})$$

with the boundary conditions $S_n(0) = S_n(2\pi)$, $S'_n(0) = S'_n(2\pi)$. The solution is such that

$\lambda_n = n^2$, $n = 0, 1, 2, 3, \dots$, which gives

$n = 0$:

$$S_0(\varphi) = A_0 \quad (\text{A.5a})$$

$$R_0(r) = C_0 + D_0 \ln r_w \quad (\text{A.5b})$$

$n \neq 0$:

$$S_n(\xi) = A_n e^{in\xi} + B_n e^{-in\xi} \quad (\text{A.6a})$$

$$R_n(r) = C_n r^n + D_n r^{-n} \quad (\text{A.6b})$$

In order to avoid the singularity at the origin $r_w = 0$, the solution $R_n(r_w)$ satisfies either $C_n = 0$ for $n < 0$ or $D_n = 0$ for $n > 0$. In all cases, $R_n(r_w)$ can be written as

$$R_n(r) = C_n r^{|n|} \quad (\text{A.7})$$

The combination of all single solutions gives the expression

$$K(r_w, \xi) = \sum_{n=-\infty}^{\infty} c_n r_w^{|n|} e^{in\xi} \quad (\text{A.8})$$

The reformulation of the boundary condition $f(\theta)$ in Fourier series

$$f(\xi) = \sum_{n=-\infty}^{\infty} c_n r_0^{|n|} e^{in\xi} \quad (\text{A.9a})$$

implies

$$c_n = \frac{r_0^{-|n|}}{2\pi} \int_{-\pi}^{\pi} f(\varphi) e^{-in\varphi} d\varphi \quad (\text{A.9b})$$

$$K(r_w, \xi) = \int_{-\pi}^{\pi} \left[\frac{1}{2\pi} \sum_{n=-\infty}^{\infty} \left(\frac{r_w}{r_0} \right)^{|n|} e^{in(\xi-\varphi)} \right] f(\varphi) d\varphi, \quad r_w \leq r_0 = \frac{1}{b} \quad (\text{A.10})$$

Introducing the dimensionless variable $z = \frac{r_w}{r_0}$, then

$$\begin{aligned} \sum_{n=-\infty}^{\infty} z^{|n|} e^{inq} &= 1 + \sum_{n=1}^{\infty} z^n e^{inq} + \sum_{n=1}^{\infty} z^n e^{-inq} \\ &= 1 + \frac{ze^{iq}}{1 - ze^{iq}} + \frac{ze^{-iq}}{1 - ze^{-iq}} \\ &= \frac{1 - z^2}{1 - 2z \cos q + z^2} \end{aligned} \quad (\text{A.11})$$

The function

$$k(r, \xi) = \frac{1}{2\pi} \frac{1 - r^2}{1 + r^2 - 2r \cos \xi} \quad (\text{A.12})$$

is known as Green's function of the unit circle domain for the Laplace problem subjected to the Dirichlet boundary condition. This function is valid for any complex z with $|z| < 1$ and for any real $r_w < r_0$. Equation (A.10) can then be rewritten as

$$K(r_w, \xi) = \frac{1}{2\pi} \int_0^{2\pi} \frac{r_0^2 - r_w^2}{r_0^2 + r_w^2 - 2r_0 r_w \cos(\xi - \varphi)} f(\varphi) d\varphi, \quad r \leq r_0 = \frac{1}{b} \quad (\text{A.13})$$

where $f(\varphi)$ is the dimensionless boundary value on the cylinder wall in the w - plane.

The substitution of Equation (A.2) into Equation (A.13) gives the solution of Equation (A.1) as

$$K(r, \theta) = \frac{1}{2\pi} \int_0^{2\pi} \frac{r^2 - b^2}{r^2 - 2rb \cos(\theta + \varphi) + b^2} f(\varphi) d\varphi, \quad r \geq b \quad (\text{A.14})$$

APPENDIX B

SIMPLIFICATION OF THE INTEGRAL EXPRESSION IN THE ANALYTICAL EXPRESSION OF THE ELECTRIC POTENTIAL

The solution of the Laplace equation $\nabla^2 U = 0$ subjected to the Dirichlet boundary conditions

$$f(\varphi) = \begin{cases} 1, & \theta_1 < \varphi < \theta_2 \\ -1, & 2\pi - \theta_2 < \varphi < 2\pi - \theta_1 \\ 0, & \text{otherwise} \end{cases} \quad (\text{B.1a})$$

along the cylinder surface of radius b is

$$U(r, \theta) = \frac{1}{2\pi} \left[\int_b^{2\pi} \frac{b^2 - r^2}{b^2 - 2rb \cos(\varphi - \theta) + r^2} f(\varphi) d\varphi \right] \quad (\text{B.1b})$$

where $0 < \theta_1 < \theta_2 < \pi$, $0 \leq \theta \leq 2\pi$

The functions defined as

$$S^+(r, \theta) = \frac{1}{2\pi} \int_{\theta_1}^{\theta_2} \frac{b^2 - r^2}{b^2 - 2rb \cos(\varphi - \theta) + r^2} d\varphi \quad (\text{B.2})$$

$$S^-(r, \theta) = \frac{1}{2\pi} \int_{2\pi - \theta_2}^{2\pi - \theta_1} \frac{b^2 - r^2}{b^2 - 2rb \cos(\varphi - \theta) + r^2} d\varphi \quad (\text{B.3})$$

satisfy the relations

$$S^-(r, \theta) = S^+(r, 2\pi - \theta) \quad (\text{B.4})$$

$$U(r, \theta) = S^+(r, \theta) - S^-(r, \theta) = S^+(r, \theta) - S^+(r, 2\pi - \theta) \quad (\text{B.5})$$

In a continuous x -domain, where $x = \varphi - \theta$, the integrand function

$\frac{1}{2\pi} \frac{b^2 - r^2}{b^2 - 2rb \cos(\varphi - \theta) + r^2}$ can be integrated by the substitution of variable as

$$F(x) = \frac{1}{2\pi} \int \frac{b^2 - r^2}{b^2 - 2br \cos(\varphi - \theta) + r^2} d\varphi = \frac{1}{\pi} \tan^{-1} \left(\frac{b+r}{b-r} \tan \frac{x}{2} \right) + const \quad (\text{B.6})$$

The function $F(x)$ is not continuous at the specific x -values $x = \pm(2n-1)\pi$, $n = 0, 1, 2, 3, \dots$. Therefore, in the subdomains such that $\varphi - \theta \neq (2n-1)\pi$ at all points, $S^+(r, \theta)$ is the definite integral of $f(x)$ with the corresponding upper and lower limits of integration. For a subdomain containing points such that $\varphi - \theta = (2n-1)\pi$, the Riemann integral is used to find the result. The following discussion is for $0 < \theta_1 < \varphi < \theta_2 < \pi$ and $0 < \theta < 2\pi$.

1) Domain defined by $\theta = 0$, $0 < \frac{\theta_1}{2} < \frac{\varphi - \theta}{2} < \frac{\theta_2}{2} < \frac{\pi}{2}$. The function $F(x)$ is continuous in this domain. $S^+(r, \theta)$ can be directly integrated from Equation (B.6):

$$S^+(r, \theta) = \frac{1}{\pi} \left(\tan^{-1} \left(\frac{a+r}{a-r} \tan \frac{\theta_2}{2} \right) - \tan^{-1} \left(\frac{a+r}{a-r} \tan \frac{\theta_1}{2} \right) \right) \quad (\text{B.7})$$

2) Domain defined by $0 < \theta < \pi$, $-\frac{\pi}{2} < -\frac{\theta_2}{2} < \frac{\varphi - \theta}{2} < \frac{\pi - \theta_1}{2} < \frac{\pi}{2}$. $S^+(r, \theta)$ is continuous in this domain, so that

$$S^+(r, \theta) = \frac{1}{\pi} \left(\tan^{-1} \left(\frac{a+r}{a-r} \tan \frac{\theta_2 - \theta}{2} \right) + \tan^{-1} \left(\frac{a+r}{a-r} \tan \frac{\theta - \theta_1}{2} \right) \right) \quad (\text{B.8})$$

3) Domain defined by $\theta = \pi$, $-\frac{\pi}{2} < -\frac{\pi - \theta_1}{2} < \frac{\varphi - \theta}{2} < -\frac{\pi - \theta_2}{2} < 0$. The case is similar to $\theta = 0$, and, therefore,

$$S^+(r, \theta) = \frac{1}{\pi} \left(\tan^{-1} \left(\frac{a+r}{a-r} \tan \frac{\theta_1}{2} \right) - \tan^{-1} \left(\frac{a+r}{a-r} \tan \frac{\theta_2}{2} \right) \right) \quad (\text{B.9})$$

4) Domain $\pi < \theta < \theta_1 + \pi$, $-\frac{\pi}{2} < \frac{\varphi - \theta}{2} < -\frac{\pi - \theta_2}{2} < 0$. $S^+(r, \theta)$ is continuous in that domain so that

$$S^+(r, \theta) = \frac{1}{\pi} \left(\tan^{-1} \left(\frac{a+r}{a-r} \tan \frac{\theta - \theta_1}{2} \right) + \tan^{-1} \left(\frac{a+r}{a-r} \tan \frac{\theta_2 - \theta}{2} \right) \right) \quad (\text{B.10})$$

5) Domain defined by $\theta = \theta_1 + \pi$, $-\frac{\pi}{2} < -\frac{\pi - \theta_1}{2} < \frac{\varphi - \theta}{2} < -\frac{\pi - \theta_2}{2} < 0$. In this case,

$S^+(r, \theta)$ becomes

$$S^+(r, \theta) = \frac{1}{\pi} \left(\frac{\pi}{2} - \tan^{-1} \left(\frac{a+r}{a-r} \tan \frac{\theta_2 - \theta_1}{2} \right) \right) \quad (\text{B.11})$$

6) Domain defined by $\theta_1 + \pi < \theta < \theta_2 + \pi$,

$-\pi < -\frac{\pi}{2} - \frac{\theta_2 - \theta_1}{2} < \frac{\varphi - \theta}{2} < -\frac{\pi - \theta_2}{2} - \frac{\theta_1}{2} < 0$. In this case, $\tan\left(\frac{\varphi - \theta}{2}\right)$ is

discontinuous at the points $\frac{\varphi - \theta}{2} = -\frac{\pi}{2}$. In this case, after introducing ε as a positive,

small number, the Riemann integral leads to

$$\begin{aligned} S^+(r, \theta) &= \frac{1}{\pi} \tan^{-1} \left(\frac{a+r}{a-r} \tan \frac{\varphi - \theta}{2} \right) \Bigg|_{\varphi=\theta_1}^{\varphi=\theta_2} \\ &= \frac{1}{\pi} \tan^{-1} \left(\frac{a+r}{a-r} \tan \frac{\varphi - \theta}{2} \right) \Bigg|_{\varphi=\theta_1}^{\varphi=\theta - \pi - \varepsilon} + \frac{1}{\pi} \tan^{-1} \left(\frac{a+r}{a-r} \tan \frac{\varphi - \theta}{2} \right) \Bigg|_{\varphi=\theta - \pi + \varepsilon}^{\varphi=\theta_2} \\ &= 1 + \frac{1}{\pi} \left(\tan^{-1} \left(\frac{a+r}{a-r} \tan \frac{\theta - \theta_1}{2} \right) + \tan^{-1} \left(\frac{a+r}{a-r} \tan \frac{\theta_2 - \theta}{2} \right) \right) \end{aligned} \quad (\text{B.12})$$

7) Domain defined by $\theta = \theta_2 + \pi$, $-\pi < -\frac{\pi}{2} - \frac{\theta_2 - \theta_1}{2} < \frac{\varphi - \theta}{2} < -\frac{\pi}{2}$. Similarly,

$$S^+(r, \theta) = \frac{1}{\pi} \left(\frac{\pi}{2} - \tan^{-1} \left(\frac{a+r}{a-r} \tan \frac{\theta_2 - \theta_1}{2} \right) \right) \quad (\text{B.13})$$

8) Domain defined by $\theta_2 + \pi < \theta < 2\pi$, $-\pi < -\pi + \frac{\theta_1}{2} < \frac{\varphi - \theta}{2} < -\frac{\pi}{2}$. $F(x)$ is continuous

and $S^+(r, \theta)$ takes the expression

$$S^+(r, \theta) = \frac{1}{\pi} \left(\tan^{-1} \left(\frac{a+r}{a-r} \tan \frac{\theta - \theta_1}{2} \right) + \tan^{-1} \left(\frac{a+r}{a-r} \tan \frac{\theta_2 - \theta}{2} \right) \right) \quad (\text{B.14})$$

9) Domain defined by $\theta = 2\pi$, $-\pi < -\pi + \frac{\theta_1}{2} < \frac{\varphi - \theta}{2} < -\frac{2\pi - \theta_2}{2} - \frac{\pi}{2}$. In this case,

$$S^+(r, \theta) = \frac{1}{\pi} \left(\tan^{-1} \left(\frac{a+r}{a-r} \tan \frac{\theta_2}{2} \right) - \tan^{-1} \left(\frac{a+r}{a-r} \tan \frac{\theta_1}{2} \right) \right) \quad (\text{B.15})$$

Therefore, it can be concluded that the expression for the electric potential is

$$U(r, \theta) = S^+(r, \theta) - S^+(r, 2\pi - \theta) \quad (\text{B.16})$$

with

$$S^+(r, \theta) = \begin{cases} \frac{1}{\pi} \left(\tan^{-1} \left(\frac{a+r}{a-r} \tan \frac{\theta - \theta_1}{2} \right) + \tan^{-1} \left(\frac{a+r}{a-r} \tan \frac{\theta_2 - \theta}{2} \right) \right), & 0 \leq \theta \leq \theta_1 + \pi \text{ or } \theta_2 + \pi \leq \theta \leq 2\pi \\ 1 + \frac{1}{\pi} \left(\tan^{-1} \left(\frac{a+r}{a-r} \tan \frac{\theta - \theta_1}{2} \right) + \tan^{-1} \left(\frac{a+r}{a-r} \tan \frac{\theta_2 - \theta}{2} \right) \right), & \theta_1 + \pi < \theta < \theta_2 + \pi \end{cases} \quad (\text{B.17})$$

APPENDIX C

GENERATION OF A VORTEX FLOW BY MEANS OF AN ELECTROMAGNETIC CYLINDER

This appendix gives the details of the electro-magnetic field and rotational fluid flow generated by an electro-magnetic cylinder. The schematic of the alternating arrangement of the electrodes and magnets on the surface of the cylinder is given in Figure C.1. In this case, there is no discontinuity of the electric and magnetic fields in the azimuthal direction and the resulting Lorentz force is oriented in the clockwise direction. On the surface of the cylinder, the no-slip boundary condition applies and the fluid velocity is zero. Sufficiently far away from the cylinder, the velocity is zero as well. At any intermediate position the velocity will increase and then decrease again. It follows that at some distance $r = r^*$, the fluid reaches its maximal velocity. It thus makes sense that the velocity profile is qualitatively a single peak function as shown in Figure C.1.

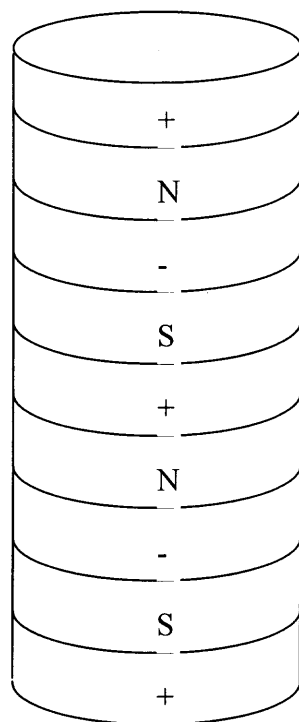
The electric and magnetic potential functions satisfy Laplace equations subjected to Dirichlet boundary conditions which, in the $r - x$ plane (r and x denoting the radial and axial directions, respectively), take the form:

$$\frac{1}{r} \left(\frac{\partial}{\partial r} r \frac{\partial U}{\partial r} \right) + \frac{\partial^2 U}{\partial x^2} = 0 \quad (\text{C.1a})$$

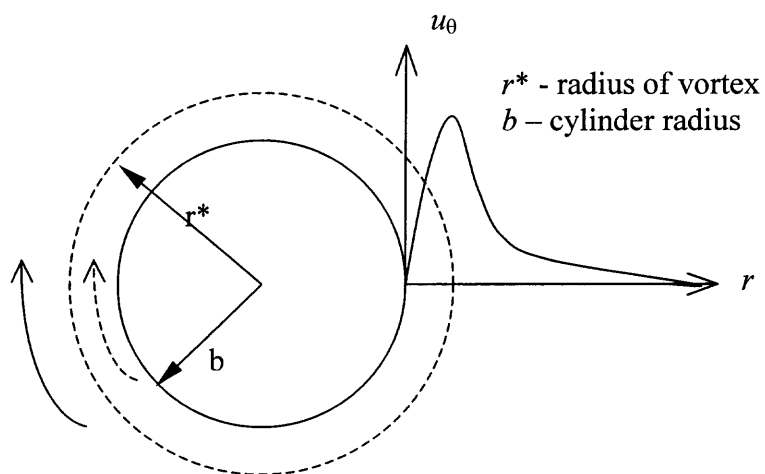
$$U(r, -a) = U(r, a) = 0, \quad r \geq b \quad (\text{C.1b})$$

$$U(b, x) = U_0, \quad -\frac{a}{2} < x < \frac{a}{2} \quad (\text{C.1c})$$

$$U(b, x) = 0, \quad -a < x < -\frac{a}{2} \quad \text{or} \quad \frac{a}{2} < x < a \quad (\text{C.1d})$$



(a) Alternating arrangement of electrodes and magnets.



(b) Qualitative azimuthal velocity profile in the radial direction.

Figure C.1 Scheme of the generation of a vortex by the displayed alternating arrangement of electrodes and magnets.

By applying the method of separation of variables, $U(r, x) = R(r)X(x)$, Equation

(C.1) can be split into two equations

$$\frac{\partial^2 X_n}{\partial x^2} + \lambda_n^2 X_n = 0 \text{ with } X_n(-a) = X_n(a) = 0 \quad (\text{C.2a})$$

$$\frac{1}{r} \left(\frac{\partial}{\partial r} r \frac{\partial R}{\partial r} \right) - \lambda_n^2 R = 0 \text{ with } R_n(r=b) = U_0 \text{ and } R_n(r > b) < \infty \quad (\text{C.2b})$$

The general solution is

$$U(r, x) = \sum_{n=0}^{\infty} A_n K_0(\lambda_n r) \cos(\lambda_n x) \quad \text{with } \lambda_n = \left(n + \frac{1}{2}\right) \frac{\pi}{a} \quad (\text{C.3})$$

where $K_0(\cdot)$ is the modified zero order Bessel function of second type. The coefficient A_n is

determined by the boundary condition (4.12c) as $A_n = \frac{2U_0}{a\lambda_n K_0(\lambda_n b)} \sin\left(n + \frac{1}{2}\right) \frac{\pi}{2}$.

Therefore, the electric potential takes the expression:

$$U(r, x) = \sum_{n=0}^{\infty} \frac{2U_0}{a\lambda_n K_0(\lambda_n b)} \sin\left(n + \frac{1}{2}\right) \frac{\pi}{2} \cdot K_0(\lambda_n r) \cos(\lambda_n x) \quad (\text{C.4a})$$

with

$$\lambda_n = \left(n + \frac{1}{2}\right) \frac{\pi}{a} \quad (\text{C.4b})$$

Similarly, the magnetic potential in the $r - x$ plane satisfies the Laplace equation

$$\frac{1}{r} \left(\frac{\partial}{\partial r} r \frac{\partial \Phi}{\partial r} \right) + \frac{\partial^2 \Phi}{\partial x^2} = 0 \quad (\text{C.5a})$$

subjected to the boundary conditions

$$\Phi(r, -a) = \Phi(r, a) = 0, \quad r \geq 1 \quad (\text{C.5b})$$

$$\Phi(x, 0) = \Phi_0, \quad \frac{a}{2} < x < \frac{3a}{2} \quad (\text{C.5c})$$

$$\Phi(x, 0) = 0, \quad 0 < x < \frac{a}{2} \text{ or } \frac{3a}{2} < x < 2a \quad (\text{C.5d})$$

Then, the solution for the magnetic potential becomes

$$\Phi(r, x) = \sum_{n=0}^{\infty} \frac{2\Phi_0}{a\lambda_n K_0(\lambda_n b)} \sin\left(n + \frac{1}{2}\right) \frac{\pi}{2} \cdot K_0(\lambda_n r) \cos(\lambda_n(x - a)) \quad (\text{C.6a})$$

with
$$\lambda_n = \left(n + \frac{1}{2}\right) \frac{\pi}{a} \quad (\text{C.6b})$$

It follows that the Lorentz force $\vec{F} = \sigma \nabla U \times \nabla \Phi$ takes the form

$$f_r = f_x = 0 \quad (\text{C.7})$$

$$\begin{aligned} f_\theta(r, x) = & - \sum_{m=0}^{\infty} \sum_{n=0}^{\infty} \frac{4\sigma U_0 \Phi_0}{a^2 K_0^2(\lambda_n b)} \cdot \sin\left(m + \frac{1}{2}\right) \frac{\pi}{2} \sin\left(n + \frac{1}{2}\right) \frac{\pi}{2} \\ & \cdot [K'_0(\lambda_m r) K_0(\lambda_n r) \cos(\lambda_m x) \sin(\lambda_n(x - a)) \\ & - K_0(\lambda_m r) K'_0(\lambda_n r) \sin(\lambda_m x) \cos(\lambda_n(x - a))] \end{aligned} \quad (\text{C.8})$$

For a two-dimensional flow, the axial average of the Lorentz force is considered, i.e.

$$f_\theta(r) = - \sum_{n=0}^{\infty} (-1)^n \frac{2\sigma U_0 \Phi_0}{a^2 K_0^2(\lambda_n b)} K'_0(\lambda_n r) K_0(\lambda_n r) \text{ with } \lambda_n = \left(n + \frac{1}{2}\right) \frac{\pi}{a} \quad (\text{C.9})$$

From the identity $K'_0(z) = -K_1(z)$, it follows that

$$\begin{aligned} f_\theta(r) = & \sum_{n=0}^{\infty} (-1)^n \frac{2\sigma U_0 \Phi_0}{a^2 K_0^2(\lambda_n b)} K_1(\lambda_n r) K_0(\lambda_n r) \\ = & 2 \sum_{n=0}^{\infty} (-1)^n J_0 B_0 \frac{K_1(\lambda_n b) K_1(\lambda_n r) K_0(\lambda_n r)}{K_0(\lambda_n b) K_1(\lambda_n b) K_0(\lambda_n b)} \end{aligned} \quad (\text{C.10})$$

where $J_0 = \frac{\sigma U_0}{a}$, $B_0 = \frac{\sigma \Phi_0}{a}$.

Since $\frac{K_0(z > 1) K_1(z > 1)}{K_0(1) K_1(1)} \sim \frac{e^{-2z}}{z}$ and $K_n(z)$ is a monotonic decreasing function, the

average of the component of the Lorentz force can be approximated as follows, provided

$$\frac{\pi b}{2a} > 1.$$

$$f_\theta = \frac{2J_0 B_0}{r/b} \left[\frac{K_1\left(\frac{\pi b}{2a}\right)}{K_0\left(\frac{\pi b}{2a}\right)} e^{-\frac{\pi(r-b)}{a}} - \frac{K_1\left(\frac{3\pi b}{2a}\right)}{K_0\left(\frac{3\pi b}{2a}\right)} \frac{e^{-\frac{3\pi(r-b)}{a}}}{1 + e^{-\frac{2\pi(r-b)}{a}}} \right] \quad (\text{C.11})$$

The momentum equation of the Navier-Stokes equations can be written in cylindrical coordinates

$$\begin{aligned} & \rho \left(\frac{\partial u_r}{\partial t} + u_r \frac{\partial u_r}{\partial r} - \frac{u_\theta^2}{r} + \frac{u_\theta}{r} \frac{\partial u_r}{\partial z} \right) \\ &= \mu \left[\frac{\partial}{\partial r} \left(\frac{1}{r} \frac{\partial}{\partial r} (r u_r) \right) + \frac{1}{r^2} \frac{\partial^2 u_r}{\partial \theta^2} + \frac{\partial^2 u_r}{\partial z^2} - \frac{2}{r^2} \frac{\partial u_\theta}{\partial \theta} \right] - \frac{\partial p}{\partial r} + \rho f_r \end{aligned} \quad (\text{C.12a})$$

$$\begin{aligned} & \rho \left(\frac{\partial u_\theta}{\partial t} + u_r \frac{\partial u_\theta}{\partial r} + \frac{u_\theta}{r} \frac{\partial u_\theta}{\partial \theta} + \frac{u_r u_\theta}{r} + u_z \frac{\partial u_\theta}{\partial z} \right) \\ &= \mu \left[\frac{\partial}{\partial r} \left(\frac{1}{r} \frac{\partial}{\partial r} (r u_\theta) \right) + \frac{1}{r^2} \frac{\partial^2 u_\theta}{\partial \theta^2} + \frac{\partial^2 u_\theta}{\partial z^2} + \frac{2}{r^2} \frac{\partial u_r}{\partial \theta} \right] - \frac{\partial p}{\partial \theta} + \rho f_\theta \end{aligned} \quad (\text{C.12b})$$

$$\begin{aligned} & \rho \left(\frac{\partial u_z}{\partial t} + u_r \frac{\partial u_z}{\partial r} + \frac{u_\theta}{r} \frac{\partial u_z}{\partial \theta} + u \frac{\partial u_z}{\partial z} \right) \\ &= \mu \left[\frac{\partial}{\partial r} \left(\frac{1}{r} \frac{\partial}{\partial r} (r u_z) \right) + \frac{1}{r^2} \frac{\partial^2 u_z}{\partial \theta^2} \right] - \frac{\partial p}{\partial z} + \rho f_z \end{aligned} \quad (\text{C.12c})$$

Assuming that the laminar flow generated by the previous Lorentz force is steady, has zero radial and axial components, and is independent of the azimuthal position θ , the momentum equations reduce to its projection onto the azimuthal direction:

$$\nu \frac{\partial}{\partial r} \left(\frac{1}{r} \frac{\partial}{\partial r} (r u_\theta) \right) + f_\theta(r) = 0 \quad (\text{C.13})$$

which leads to the expression of the azimuthal component of the generated velocity as follows.

$$u_\theta = \frac{1}{r} \int r \int f_\theta(r) dr + c_1 r + \frac{c_2}{r} \quad (\text{C.14})$$

Using the fact that the velocity is zero at infinity and on the cylinder surface, i.e.

$u_\theta(r = \infty) = 0$ and $u(r = b) = 0$, it follows that the constants vanish $c_1 = c_2 = 0$, and thus

$$u_\theta = \frac{1}{r} \int s \int f_\theta(y) dy ds \quad (\text{C.15})$$

At the distance $r = r^*$, u_θ reaches its maximal value so that its derivative is zero, that is

$u'_\theta(r = r^*) = 0$. The location at which the velocity reaches its maximum is thus given by

$$r^* = \left(\frac{\int s \int f_\theta(y) dy ds}{\int f_\theta(y) dy} \right)^{\frac{1}{2}} = \left(\frac{1}{2} \frac{\int (r^2 - y^2) f_\theta(y) dy}{\int f_\theta(y) dy} \right)^{\frac{1}{2}} \quad (\text{C.16})$$

The azimuthal velocity u_θ increases with r in the interval $0 < r < r^*$ close to the cylinder wall, and then decreases for r values larger than r^* , that is for $r > r^*$.

REFERENCES

- Abergei, F. and Terman, R. 1990 On some control problems in fluid mechanics. *Theor. Comput. Fluid Dyn.*, 1, 303.
- Apelt, C. J. and West, G. S. 1975 The effects of wake splitter plates on bluff body flow in the range $10^4 < R < 5 \times 10^4$, Part 2: *J. Fluid Mech.* 71, 145.
- Apelt, C. J., West, G. S., and Szewczyk, A. A. 1973 The effects of wake splitter plates on the flow past a circular cylinder in the range $10^4 < R < 5 \times 10^4$. *J. Fluid Mech.* 61, 187.
- Aubry, N., Chen, Z., and Li, F. 2000 Closed loop control of wake flows. IUTAM Sym. On bluff body and Vortex-induced vibrations, Marseille France.
- Aubry, N. and Tang, S. 1998 Controlling vortex shedding by insertion of vortices. Proceedings of the ASME Fluids Engineering Division Summer Meeting, June 21-25, Washington, D. C.
- Bearman, P. W. 1967 The effects of base bleed on the behind a two-dimensional model with a blunt trailing edge. *Aero. Q.* 18, 207.
- Berger, T. W., Kim, J. and Lee, C. 2000 Turbulent boundary layer control utilizing the Lorentz force. *Phys., Fluids* 12(3), pp. 631-649.
- Blackburn, H. M., and Karniadakis, G. E. 1993 Two and three-dimensional simulations of vortex induced vibration of a circular cylinder. Proc. 3rd inst Offshore and Polar Engng conf. Singapore, 3, 715-720.
- Blackburn, H. and Henderson, R. 1996 Lock-in Behavior in simulated vortex-induced vibration. *Experimental Thermal and Fluid Science* 12, 184-189.
- Bouard, R. and Coutanceau, M. 1980 The early stage of development of the wake behind an impulsively started cylinder for $40 \leq Re \leq 10^4$. *J. Fluid Mech.* 101, 583-607.
- Wood, C. J. 1967 Visualization of an incompressible wake with base bleed. *J. Fluid Mech.* 233, 246-263.
- Chang, C. C. and Chern, R. L. 1991 A numerical study of flow around an impulsively started circular cylinder by a deterministic vortex method. *J. Fluid Mech.* 233, 246-263.
- Choi, H., Temam, R., Moin, P., and Kim, J. 1993 Feedback control for unsteady flow and its application to the stochastic Burgers equation. *J. Fluid Mech.* 253, 509.

- Cimbala, J. M., and Garg, S. 1991 Flow in the wake of freely rotatable cylinder with splitter plate. *AIAA J.* 29,1001.
- Collins, W. M. and Dennis, S. C. R. 1973 Flow past an impulsively started circular cylinder. *J. Fluid Mech.* 60,105-127.
- Crawford, C. and Karniadakis, G. E. 1997 Reynolds stress analysis Of EMHD-controlled wall turbulence. Part I Streamwise forcing. *Phys. Fluids*, 9, No. 3, 788-806.
- Fan, X. and Brown, G. L. 1997 Experiments on the electromagnetic control of turbulence. *AIAA- paper 97- 2123.*
- Gad-el-Hak, M. 1996 Modern developments in flow control. *Appl. Mech.Rev.* 49(7), 365-379.
- Gailitis, A. and Leilausis, O. 1961 On a possibility to reduce the htdrodynamical resistance of a plate in an electrolyte. *Applied Magneto hydrodynamics. Reports of the Physics Institute Riga.* 12,143-146.
- Gerrard, J. H. 1966 The mechanics of the formation region of vortices behind bluff bodies. *J. Fluid Mech.* 25, 401.
- Griffin, O. M. & Hall, M. S. 1991 Review: Vortex Shedding Lock-on Control in Bluff Body Wakes. *Journal of Fluids Engineering.* 113, 526-537.
- Grienberg, E. 1961 On determination of properties of some potential fields (in Russian), in: *Applied Magnetohydrodynamics. Report of the Physics Institute 12 (Prikladnaya Magnitogidrodinamika, Trudy Instituta Fiziki,12), Riga, pp 147-154.*
- Gunzburger, M. D. and Lee, H. C. 1996 Feedback control of Karman vortex shedding. *Journal of Applied Mechanics*, 63,828-835.
- Hammache, M. and Gharib, M. 1991 An experimental study of the parallel and oblique vortex shedding from circular cylinder. *J. Fluid Mech.* 232, 567-590.
- Hartlen, R. T. and Currie, J. G. 1970 Lift oscillator model of vortex induced vibration. *J. Engng. Mech. Div. ASCE*, 96, 577-591.
- Henderson, R. D. and Barkley, d. 1996 Secondary instability in the wake of a circular cylinder. *Phys. Fluids* 7(6), 1371-1383.
- Henoeh, C. and Stace, J. 1995 Experimental investigation of a salt water turbulent boundary layer modified by an applied streamwise magneto hydrodynamic body force body force. *Phys. Fluids* 7 (6), 1371-1383.

- Hochney, R. W. 1970 The potential calculation and some applications. *Methods Comp. Phys.* 9, 135-177.
- Kang, S. and Choi, H. 1999 Laminar flow past a rotating circular cylinder. *Phys. Fluids* 11, 3312.
- Karniadakis, G. E. and Triantafyllou, G. S. 1989 Frequency selection and asymptotic states in laminar wakes. *J. Fluid Mech.* 199, 441-469.
- Kim, S. J. and Lee C. M. 2001 Investigation of the flow around a circular cylinder under the influence of electromagnetic field. *Exp. Fluids*, 28, 252-260.
- Kim, S. J. and Lee C. M. 2001 Control of flow around a circular cylinder: suppression of oscillatory lift force. *Fluid Dynamics Research* 29, 47-63.
- Kwon, K. and Choi, H. 1996 Control of laminar vortex shedding behind a circular cylinder using splitter plates. *Phys. Fluids* 8, 479.
- Lahjomri, J., Caperan, P. and Alemany, A. 1993 The cylinder wake in a magnetic field aligned with the velocity. *J. Fluid Mech.* 253, 421-448.
- Li, Z., Navon, I. M., Hussaini, M.Y., and Dimet, F. 2000 Optimal control of the unsteady Navier-Stokes equations. Research report, Florida State Univ., Tallahassee, Florida.
- Min, C. and Choi, H. 1999 Suboptimal feedback control of vortex shedding at low Reynolds numbers. *J. Fluid Mech.* 401, 123-156.
- Monkewitz, P. A., Beger, E., and Schumm, M. 1989 Feedback control of global oscillations in fluid systems. *AIAA Paper* 89 (0991).
- Mustschke, G. Gerbeth, G., and Shatrov, V. 1997 Two- and three-dimensional instabilities of the cylinder wake in an aligned magnetic field. *Phys. Fluids* 9, 3114.
- Mustschke, G. Shatrov, V. and Gerbeth, G. 1998 Cylinder wake control by magnetic fields in liquid metal flows. *Experimental Thermal and Fluid Science* 16, 92-99.
- Nosenchuck, D. M. and Brown G. L., 1993 The direct control of wall shear-stresses in a turbulent boundary layer, in: So R. M. C., Speziale C. G., Launder B. E.(Eds.), *Proc. Of the Intern. Conf. On Near-Wall Turbulent Flows*, Elsevier, pp. 689-698.
- O'Sullivan, P. L. and Biringen, S., 1998 Direct numerical simulation of low Reynolds number turbulent channel flow with EMHD control, *Phys. Fluids* 10(5), pp.1169-1181.

- Park, D. S., Ladd, D. M., and Hendricks, E. W. 1994 Feedback back control of Von Karman vortex shedding behind a circular cylinder at low Reynolds numbers. *Phys. Fluids* 6, 2390-2405.
- Posdziech, O. and Grundmann, R. 2001 Electromagnetic control of seawater flow around circular cylinders, *Eur. J. Mech. B- Fluids* 20, pp.255-274.
- Roussopoulos, K. 1993 Feedback control of vortex shedding at low Reynolds numbers. *J. Fluid Mech.* 133,265-285.
- Stansby, P. K. 1974 The effects of end plates on the base pressure coefficient of a circular cylinder. *Aerosp. J.*78, 36.
- Strykowski, P.J. and Hannemann, H. 1991 Temporal simulation of the wake behind a circular cylinder in the neighborhood of the critical Reynolds number. *Acta Mechanica*, 90, 1-20
- Tang, S. and Aubury, N. 1997 On the symmetry breaking instability leading to vortex shedding. *Phys. Fluids* 9, (9), 2550-2560.
- Tokumaru, P. T. and Dimotakis, P. E. 1991 Rotary Oscillating Control of a Cylinder Wake. *J. Fluid Mech.* 224, 77-90.
- Tsinober, A. 1989 MHD flow drag reduction, in: Bushnell D. M., Hefner J. N. (Eds.), *Viscous Drag Reduction in Boundary Layers, Progress in Astronautics and Aeronautics*, Vol. 123, American Institute of Aeronautics and Astronautics, pp 327-349.
- Unal, M. F. and Rockwell, D. 1988 On vortex formation from a cylinder. Part 2. Control by splitter-plate interference. *J. Fluid Mech.* 190, 513.
- Van Dyke, M. 1982 *An Album of Fluid Motion*. Parabolic Press, Stanford, CA.
- Wehrmann, O. H. 1965 Reduction of velocity fluctuations in a Karman vortex street by a vibrating cylinder. *Phys. Soc.* 41, 1732.
- Weier, T. Gerbeth, G. Mutschke, G. Platacis, E. and Lielausis, O. 1998 Experiments on cylinder wake stabilization in an electrolyte solution by means of electromagnetic forces localized on the cylinder surface. *Experimental Thermal and Fluid Science* 16, 84-91.
- Zhou, C. Y., So, R. M. C. and Lam, K. 1998 Vortex-induced vibrations on bluff bodies in a cross flow. *Proc. on Bluff Body Wakes and Vortex-induced Vibration*. ASME Fluids Engineering Division Summer Meeting, 12 (1), Washington, D.C. June 21-25.